Modelling ionisation chamber response to nonstandard beam configurations

by

Laurent C. Tantot

Medical Physics Unit
McGill University, Montréal
August 2007

A thesis submitted to McGill University in partial fulfilment of the requirements of the degree of Master of Science in Medical Physics

Abstract

For patient-specific quality assurance of IMRT, a point dose measurement with an ionisation chamber and a relative dose distribution with film are performed. The use of ionisation chambers follows dosimetry protocols that only deal with reference beams, for which Spencer-Attix cavity theory is valid. However, IMRT and other recent radiation delivery techniques do not comply with these protocols. Therefore, the conversion of the dose to the chamber cavity to the dose to water becomes uncertain ; and the geometrical details of the chamber, as well as the details of the delivery, are expected to be significant. In this thesis, a realistic model of the Exradin® A12 Farmer chamber is simulated. A framework is applied for the calculation of ionisation chamber response to arbitrarily modulated fields as a summation of responses to pencil beams. This approach is used with the chamber model and tested against measurements in static open fields and dynamic MLC IMRT fields. As a benchmark test of the model, quality conversion factors values calculated by Monte-Carlo simulation with the chamber model are in agreement within 0.1 % and 0.4 % with those in the AAPM TG-51, for 6 MV and 18 MV photon beams, respectively. Pencil-beam kernels show a strong dependence on the geometrical details of the chamber. Kernel summations with open fields show a relative agreement within 4.0 % with experimental data ; the agreement is within 2.0 % for dynamic MLC IMRT beams. Simulations show a strong sensitivity of chamber response on positioning uncertainties, sometimes leading to dose uncertainties of 15 %.

Résumé

Pour le contrôle de qualité spécifique au patient en IMRT, on pratique une mesure ponctuelle de dose avec une chambre à ionisation et une mesure relative de distribution de dose avec un film. L'utilisation de chambres à ionisation suit les protocoles de dosimétrie qui ne traitent que de faisceaux de référence pour lesquels la théorie de Spencer-Attix est valide. Cependant, la radiothérapie à modulation d'intensité, ainsi que d'autres techniques récentes de radiothérapie, ne se conforme pas à ces protocoles. Par conséquent, la conversion de la dose dans la chambre à la dose dans l'eau devient incertaine ; et on s'attend à ce que les détails géométriques de la chambre, ainsi que les détails de l'émission des faisceaux, soient significatifs. Dans cette thèse, la chambre Exradin® A12 de type Farmer a été modélisée de façon réaliste. Un formalisme a été utilisé pour la simulation de la réponse de la chambre à des champs modulés de façon arbitraire, où la réponse était calculée en sommant les réponses à des faisceaux-pinceaux. Cette approche est utilisée avec le modèle de la chambre et contrôlée par comparaison avec des mesures de champs statiques ouverts et de champs d'IMRT délivrés avec un collimateur multilame (CML) en mode dynamique. Comme test de référence du modèle de la chambre, les facteurs de conversion de qualité ont été calculés avec la chambre par Monte-Carlo et les résultats montrent un accord à mieux que 0.1 % et 0.4 % avec les valeurs du TG-51 de l'AAPM pour des faisceaux de photons de 6 MV et 18 MV, respectivement. Les noyaux de faisceaux-pinceaux montrent une forte dépendance aux détails géométriques de la chambre. Les sommations des noyaux avec les champs ouverts montrent un accord relatif à mieux que 4 % avec les résulats expérimentaux ; cet accord est à mieux que 2 % pour les faisceaux d'IMRT délivrés en mode dynamique avec le CML. Les simulations ont montré une force sensibilité de la réponse de la chambre aux incertitudes dans le positionnement, provoquant quelquefois des incertitudes de dose de 15 %.

Remerciements

Au moment d'achever cette thèse et de compléter ces deux années d'études au sein de l'Unité de Physique Médicale, un profond sentiment d'accomplissement et de fierté s'empare de moi ; et c'est avec fébrilité que j'arrive finalement à la rédaction de ces remerciements. Je repense à ma situation il y a deux ou trois ans et je ne peux m'empêcher de remarquer avec plaisir tout le chemin parcouru depuis lors. Bien sûr, je n'ai pas fait ce chemin tout seul et je profite de l'occasion qui m'est donnée ici pour nommer et remercier les gens qui m'ont aidé.

En premier lieu, je veux présenter mes remerciements au Pr E. Podgoršak qui m'a accepté dans ce programme au sein de l'Unité de Physique Médicale à l'Université McGill. Je lui dois même, en quelque sorte, une seconde admission dans le programme quand certains problèmes extérieurs sont venus mettre en danger mes études. Il a su m'écouter avec indulgence mais sans manquer d'exigence, et il m'a aidé avec justesse à me remettre dans le droit chemin.

Au Dr Jan Seuntjens je veux montrer toute ma reconnaissance. Il m'a permis de travailler avec lui pour ce projet de maîtrise et il s'est montré un soutien sans faille en toutes circonstances. Dans les moments de doute au cours de ce projet, il savait être présent et prodiguer des conseils utiles, même extra-scolaires, jamais dénués de philosophie et de pragmatisme. Sa grande popularité parmi les étudiants se justifie à l'aune de ses larges compétences scientifiques et de son dévouement sans faille pour ses ouailles.

Bien sûr, je pense à mes camarades qui ont contribué à cette ambiance studieuse mais sympathique pendant deux années. Je tiens à nommer plus particulièrement Derek avec qui les conversations tournaient souvent vers des questions métaphysiques; Ismail, qui nous a très souvent reçus chez lui pour des soirées vidéo; Magdalena, qui « est magnifique »; Arman, qui est toujours au faîte de ce qui se passe dans le départment et qui, à mon avis, devrait être reçu comme citoyen d'honneur de la ville de Marseille tant ses histoires prennent immanquablement un tour extraordinaire; enfin tous mes autres camarades que je nommerais volontiers si la place ne m'était pas limitée. Un grand merci aussi aux physiciens de l'unité, notamment François et Wamied, qui ne sont jamais avares de leur savoir et de leurs compétences. Enfin, ma gratitude et quelque admiration pour Margery, qui est toujours souriante et prête à rendre service et qui connaît son métier sur le bout des doigts.

Je n'aurais pas pu entreprendre et poursuivre ces études sur ce lointain continent sans le soutien de mes parents et ma famille. La vie d'étudiant frôle quelquefois l'indigence et je ne peux qu'être aussi reconnaissant pour leur soutien financier.

Ma reconnaissance va aussi à Tamara qui, dans l'année précédant mon arrivée dans ce département, a fait montre de soutien dans mes décisions, m'a apporté son aide dans la rédaction de ma lettre de motivation et m'a prodigué quelques judicieux conseils au moment de faire des choix de vie et de carrière.

Enfin, je veux adresser mes derniers remerciements et mes pensées à la femme avec qui je partage ma vie aujourd'hui, Jill. Toujours présente et attentionnée, Jill a aussi été très patiente avec moi et mon travail. Elle m'a souvent concocté de bons plats que je dégustais quelquefois à l'hôpital. Elle m'a été d'une aide précieuse dans la correction de cette thèse grâce à ses talents de rédactrice. Et pendant deux ans, elle a été de toutes les joies et toutes les angoisses, avec un cœur grand ouvert.

Contents

List of Figures

List of Tables

Chapter 1

Introduction

1.1 External beam radiation therapy

It is estimated that 44 % of Canadian men and 39 % of women will develop cancer during their lifetime (Canadian Cancer Society, 2007).

Surgery, chemotherapy, radiation therapy and hormonal therapy are the four main techniques currently used in the treatment of cancer. Radiation therapy, in particular, is the use of radiation from X-ray or γ-ray sources, electrons, protons, *etc.*, to destroy cancer tumours. It is used not only for the treatment of tumours, but also sometimes to relieve pain and ease other problems caused when cancer spreads to other parts of the body from the primary site[1]. The rationale of radiation therapy is to damage the DNA of cancer cells in order to prevent them from growing and dividing.

Healthy tissues are also affected by radiation. Although they can repair themselves, it is best to irradiate them at as low doses as possible lest secondary cancers should occur. It is also usual practice to fraction the treatment in order to leave time to healthy tissues to recover.

There are three main ways to treat patients with radiation. Internal radiotherapy, or *brachytherapy*, is a technique where the radiation source is placed very close to, or inside, the tumour. The source, a radioactive isotope, is sealed in an implant that is put directly in the body. In *systemic radiation therapy*, the source is orally taken or injected

---

[1] `http://www.cancer.gov/cancertopics/factsheet/Therapy/radiation` (last visited: 2007/08/27).

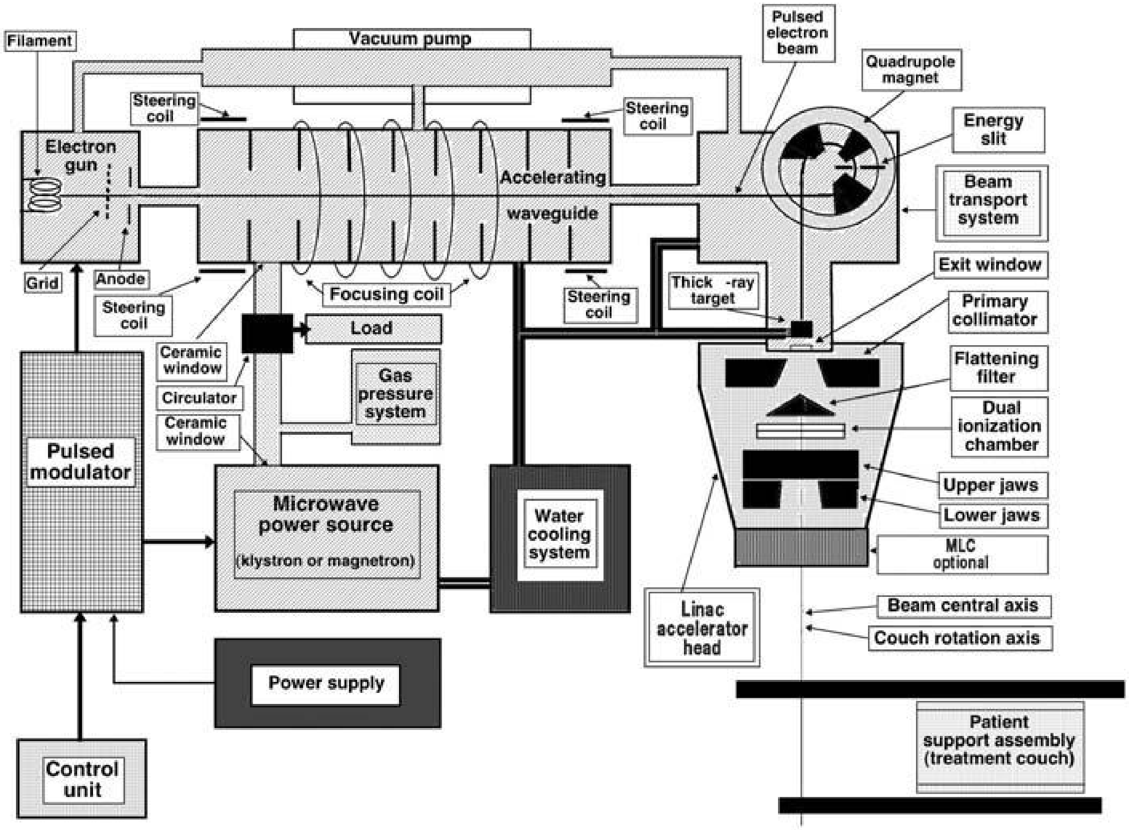

Figure 1.1: Schematic diagram of a linac. From Podgoršak (2005a)

into the body (sources for systemic radiation therapy are typically ^{131}I and ^{89}Sr for the treatment of thyroid cancer and non-Hodgkin's lymphoma). Finally, *external radiotherapy*, or teletherapy, is the most common technique, for which radiation is delivered with a source from outside of the patient. It is usually given on a outpatient basis. It is the technique we are dealing with in this thesis.

Currently, in OECD countries, the most commonly used machine in external radiotherapy is the *linear accelerator*, or *linac*. Another classical machine is the cobalt therapy unit using the γ-rays from ^{60}Co. Cobalt therapy units are less expensive, are simple to use, and are still widespread among developing countries. However, they are less versatile than linear accelerators, and their low energy, 1.25 MeV, is too low for tumours deeply embedded in the body.

The first patient to be treated with a linear accelerator was in London in 1953 (Thwaites and Tuohy, 2006). Although linear accelerators have been ameliorated over the years, their principle design is always the same (Miller, 1953; Podgoršak, 2005a). Figure 1.1 shows a schematic diagram of a linac. Electrons are created by an electron gun and fed into a waveguide that accelerates them to the required energy. The waveguide is an alignment of cavities where radio-frequency waves are guided in phase with the passage of electrons to accelerate them. The electrons exit the waveguide in little packets with a kinetic energy for clinical beams typically between 4 MeV and 25 MeV, depending on the waveguide length. They are transported and focused even more by a quadrupole magnet before they impinge upon a thick target, in which photons are created through Bremsstrahlung. Linacs may have the option of using electrons, in which case the thick target is moved out of the way. The electrons just pass through a scattering foil to broaden the beam and make it usable for treatment. After a primary collimator, which restricts the shape and the width of the beam, the photons pass through a flattening filter to assure that the radial dose distribution will be flat at a reference depth. They traverse the dual ionisation chamber, which controls the linac output. Then, the photons are collimated with two pair of jaws that shape the beam into rectangles.

Since they are created through Bremsstrahlung, all photons in a beam do not have the same energy. The photon beam has an energy spectrum whose maximum is the initial kinetic energy of the electrons. When a photon beam is created with 6 MeV electrons, for example, it is usually referred to as a “6 MV photon beam”.

Linear accelerators are complex machines used for health purposes. Therefore, they must be commissioned after their installation, and a thorough programme of quality assurance (QA) has to be followed, with checks to be performed daily, monthly and annually (Nath *et al.*, 1993; Kutcher *et al.*, 1994). For example, the linac X-ray output constancy has to be checked daily, with a tolerance of 3 %, whereas the output calibration constancy is checked annually.

1.2 IMRT with a multileaf collimator

1.2.1 Principle

A simple way to avoid the radiation of healthy tissues surrounding the tumour is to shape the beam so as to follow the projection of the tumour. This is the principle of *three-dimensional conformal radiation therapy*, or 3D-CRT. It is usually accomplished with a set of fixed beams, and the fluence is uniform across the beam. The fluence may be altered with simple modifiers, such as compensating filters or wedges (Boyer *et al.*, 2001a). However, tumours do not have the same thickness throughout, and the healthy tissues in front of the tumours may have varying densities and thicknesses. Therefore, the fluence across the beam needs to be modulated.

Intensity modulated radiation therapy (IMRT) is the delivery of radiation with fields that have non-uniform radiation fluence. To this respect, the term "intensity modulation" is improper, but it is the consecrated terminology (Webb, 2003). Brahme *et al.* (1982) wrote an article that is now recognised as the first article on intensity modulated radiation therapy, and more specifically on the inverse planning problem. Their results were the premises for what was later developed under the name of *tomotherapy* (Mackie, 2006). IMRT was developed and started to be used clinically in the late 1990s. Within the next 10 years, a large number of articles were published describing how to implement IMRT (Burman *et al.*, 1997; Boyer *et al.*, 2001a; Ezzell *et al.*, 2003; Williams, 2003; Galvin *et al.*, 2004; Guerrero Urbano and Nutting, 2004a,b). Only 32 % of the US facilities had implemented IMRT in 2002; 73 % by 2004 (Bortfeld, 2006).

The *inverse treatment planning* concept is the core of IMRT. In conventional radiation therapy techniques, even in 3D-CRT, the planning is done in a forward manner. The beam parameters are decided and set up by a dosimetrist, and a treatment planning system calculates the dose distribution. If the distribution is not good enough, the dosimetrist will change or only tweak the parameters to achieve an acceptable dose distribution. It is conceptually simple, but it requires experienced physicians, physicists and dosimetrists to decide the technique to use, *e.g.*, the beam energy, the gantry angles. Inverse planning is a technique where the dose distribution and clinical objectives are defined as the goals to reach and where the parameters of the beam delivery are to be derived to achieve these goals. Ideally, the user would define the clinical objectives, and an algorithm would calculate the beam parameters. It would be possible to do it analytically if scatter were not taken into account, and if particle fluences could be negative. In reality, computer optimisation is used. The clinical objectives are defined into mathematical objective functions that the algorithm either maximises (score function) or minimises (cost function). The result of the optimisation is a set of fluence intensity maps representing the optimal choice of beam configuration (Figure 1.2).

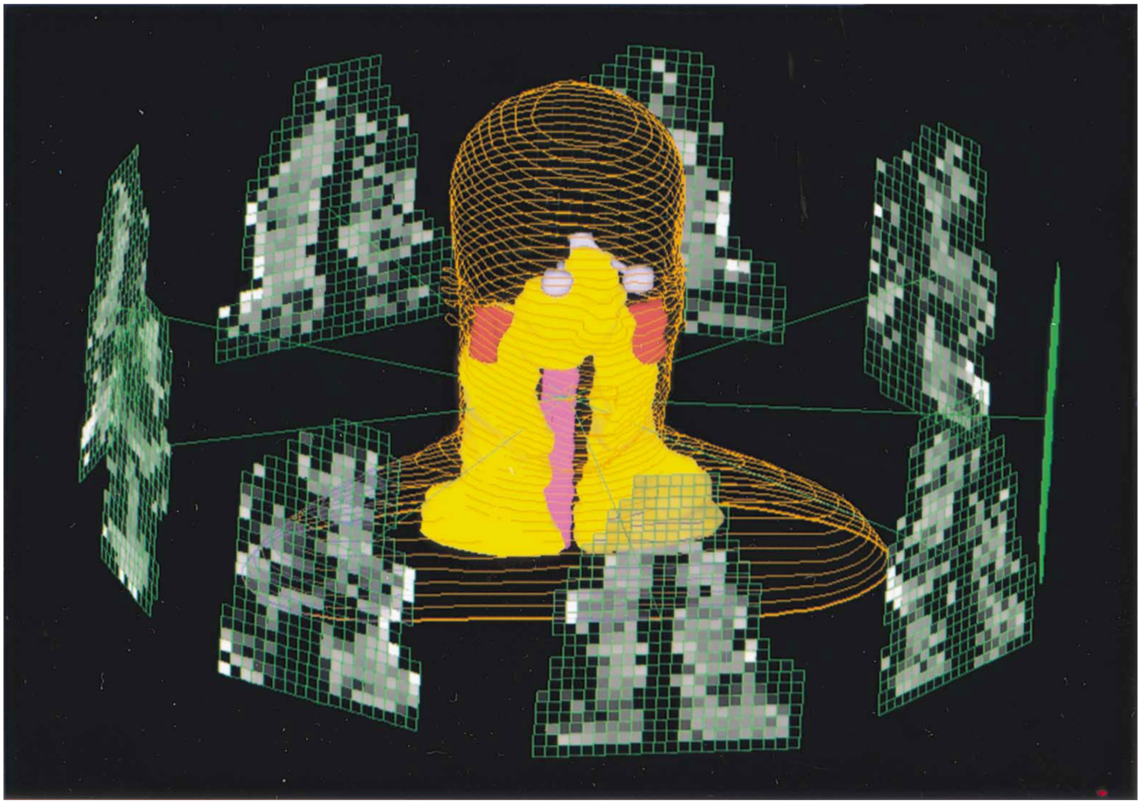

Figure 1.2: Principle of IMRT. The volumes of the PTV, spinal cord and parotid glands are reproduced with nine intensity-modulated beams used to generate the IMRT dose distribution. The grey-level maps represent the intensity values for each beam. From Boyer *et al.* (2001a).

1.2.2 Delivery with an MLC

The energy of the photon beam used in IMRT depends on the localisation of the tumour. However, it is argued that the energy should be lower than 10 MV in order to limit secondary dose to the patient and to avoid neutron contamination (Followill and Nüsslin, 2007).

Figure 1.3: Picture of the 120 Millenium multileaf collimator from Varian®. The rounded leaf ends can be seen. From Bortfeld (2006).

The most common way to deliver IMRT plans is with the use of a *multileaf collimator*, or MLC. The idea of the MLC is actually quite old. It was patented in 1906 by Robinsohn in Germany and was used with a diagnostic X-ray set (Webb, 1993). The MLC was not designed initially for IMRT, but rather as an alternative to traditional field-shaping techniques (Boyer *et al.*, 2001b). Its first use was to replace conventional blocking for conformal therapy. Its second application was to continuously adjust the field shape during procedures such as arc therapy. The shape outlined by the MLC was a function of the gantry angle. Finally, Källman *et al.* (1988) decribed how to use the MLC dynamically to shape dose distribution, and Convery and Rosenbloom (1992) described how the MLC could be used for IMRT in a dynamic mode.

A multileaf collimator is an optional feature on linacs, added to the treatment head, below the jaws (Figure 1.1). In basic terms, it is a set of pairs of tungsten alloy leaves that can individually move across the beam (Figure 1.3). The end of the MLC leaves is designed to follow the beam divergence as the field opens and closes. An alternative is to keep the flat leaf end parallel to the beam fluence. However, the leaves need to move on a circle centred at the source. It is easily done so with the primary jaws, but it is more complicated with 80 or even 120 MLC leaves. The alternative adopted by Philips® and Varian® is to design MLCs with rounded leaf ends (Figure 1.3). This design creates a penumbra, but the penumbra is always the same because the beam traverses a chord at the end of the leaf that is approximately always of the same length (Boyer *et al.*, 2001b).

The fluence intensity maps computed by the inverse treatment planning system are fed to a leaf sequence algorithm. It will either define the shapes (for static MLC IMRT) or the leaf trajectories (for dynamic MLC IMRT) that will produce the required fluence intensity map for each gantry angle used. In *static MLC* IMRT, or *step-and-shoot* IMRT, the leaves are set and fixed for each beam, then moved for the next beam, and so forth. It is a way to deliver intensity modulation in both discrete levels of intensity and discrete spatial increments of those levels across the treatment field (Bortfeld *et al.*, 1994a,b; Xia and Verhey, 1998). *Dynamic MLC IMRT*, on the other hand, is a method used to deliver IMRT with the MLC leaves in motion during radiation delivery. The leaves travel across the beam, and their trajectory will recreate the desired fluence intensity maps (Källman *et al.*, 1988; Spirou and Chui, 1994; Svensson *et al.*, 1994; Burman *et al.*, 1997; Webb, 2000). For both segmental and dynamic MLC IMRT, there is more than one leaf sequence that can produce the required fluence intensity maps (Bortfeld *et al.*, 1994a; Spirou and Chui, 1994; van Santvoort and Heijimen, 1996; Convery and Webb, 1998; Xia and Verhey, 1998).

Dynamic MLC mode is, in general, more accurate, and the delivered intensity profile better matches the optimised intensity profile. Furthermore, segmental MLC mode is known to prolong the delivery time, thus increasing the dose to healthy tissues because of the leaf transmission. However, segmental MLC is simple, less demanding on hardware, and its verification and quality assurance are straightforward. Finally it is argued that treatment time can be dramatically reduced by the recent development of direct aperture-based optimisation (Xia and Ting, 2007).

1.2.3 Effects of MLC on dose distribution

The use of multileaf collimators give rise to several issues that need to be studied and/or taken into account:

- *Intraleaf transmission* is the transmission of the primary radiation through the leaves when they are across the beam. The leaves are made of a tungsten alloy, which has one of the highest densities, in order to limit the transmission. The leaves are typically 6 cm thick. Another associated effect is *scatter*, the radiation exiting the MLC after interacting with it. Studies of intraleaf transmission and scatter showed that they account for 1 % to 2 % of the absorbed dose (Huq *et al.*, 1995; Arnfield *et al.*, 2000; Pasquino *et al.*, 2006). This transmission through the leaves also has the effect of hardening the beam (Kim *et al.*, 2001).

- *Interleaf transmission*, or *leakage*, is the transmission of radiation between adjacent or abutting leaves. For mechanical reasons, there always is a gap between adjacent leaves, and radiation will go through and increase the absorbed dose. Similarly, because of the rounded leaf ends, abutting leaves close the field with a varying thickness, and transmission is higher at the tip than in the rest of the leaves (Huq *et al.*, 1995; Arnfield *et al.*, 2000; LoSasso *et al.*, 1998; Bayouth and Morrill, 2003; Pasquino *et al.*, 2006). Figure 1.4a shows the effect of leakage on the dose distribution.

- Common commercial MLCs have stair-step leaf sides to minimise interleaf transmission. The stair steps of an adjacent leaf pair interlock in a *tongue-and-groove* arrangement. When adjacent leaves are following the same trajectory and therefore are not creating the same 1D intensity profile, there are times when the narrow strip in the beam's-eye view of the interlocking stair steps is shielded by just one stair step from one or the other adjacent leaves rather than either completely exposed or completely shielded by the interlocking stair steps (Figure 1.4b). This leads to an underdosage in this strip, but it can be removed by synchronising the movement of adjacent leaves (van Santvoort and Heijimen, 1996; Wang *et al.*, 1996; Webb *et al.*, 1997; Deng *et al.*, 2001).

- The *leaf positioning accuracy* and, in dynamic mode, the *leaf speed accuracy* are critical to assure an accurate delivery of the IMRT plan (LoSasso *et al.*, 1998; Ezzell *et al.*, 2003; Pasquino *et al.*, 2006).

- The *penumbra* is caused by the rounded leaf end, as well as the tongue or groove of the leaf. The leaves are positioned to be parallel to the primary beam fluence, but the stair-step design of the leaves creates a penumbra. The shape of this penumbra depends on whether it is on the tongue side or on the groove side of the leaf (Huq *et al.*, 1995; LoSasso *et al.*, 1998; Bayouth and Morrill, 2003; Chow *et al.*, 2006; Pasquino *et al.*, 2006). The penumbra at the end of the leaf is due to its rounded shape. However, as said earlier, the shape of the penumbra barely varies with the leaf position.

All these effects need to be studied when commissioning the MLC. However, they are not always taken into account by the inverse treatment planning system, especially because some of those effects depend on the leaf sequencing. Consequently, some of these effects, *e.g.*, tongue-and-groove effect and leaf positioning uncertainties, will create dose gradients that will not be smoothed out even after the delivery of all the fields of the IMRT plan.

1.3 Patient-specific quality assurance of IMRT

The patient-specific quality assurance of Intensity Modulated Radiation Therapy (IMRT) plans (Ting and Davis, 2001) generally involves measurements of a point dose with an

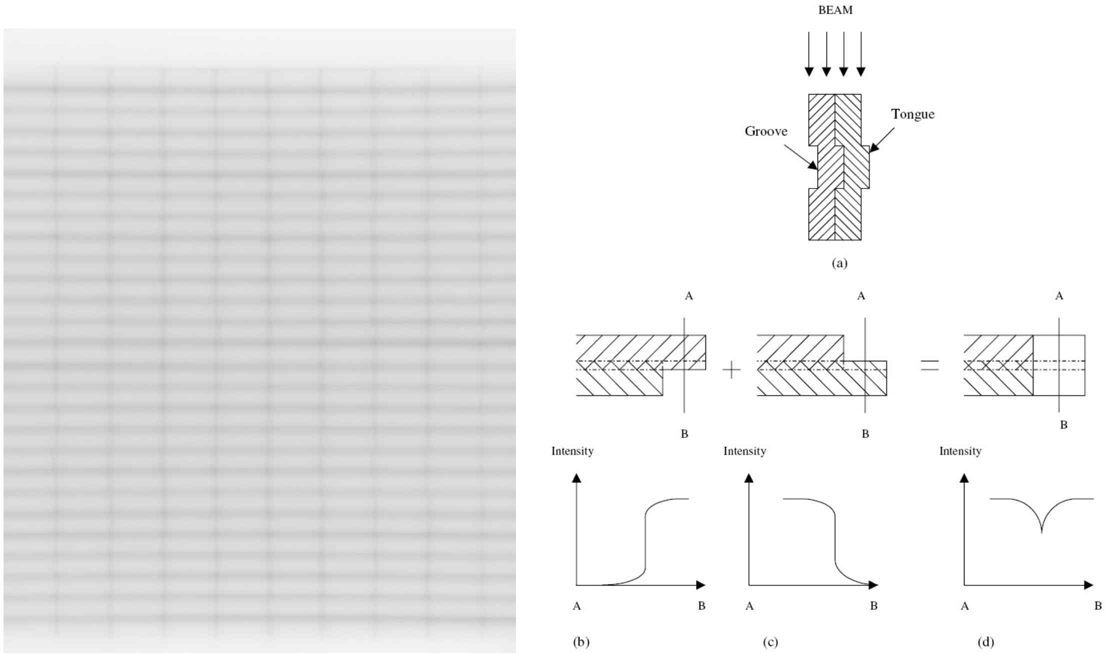

(a) Effect of interleaf transmission

(b) Tongue-and-groove effect

Figure 1.4: (a) Effect of interleaf transmission on dose distribution. The horizontal pattern shows the leakage between adjacent leaves. The vertical pattern shows the effect of rounded-leaf-end transmission when opposing leaves are abutted at different positions. From Bayouth and Morrill (2003). (b) Illustration of the tongue-and-groove effect. From Deng *et al.* (2001).

ionisation chamber and a dose distribution using a radiographic or radiochromic film (Devic *et al.*, 2005) in a standard phantom (Low *et al.*, 1998; Paliwal *et al.*, 2000; Agazaryan *et al.*, 2003; Ma *et al.*, 2003; Richardson *et al.*, 2003; Boehmer *et al.*, 2004; McNiven *et al.*, 2004; Ahnesjö *et al.*, 2006). The term "patient-specific" refers to the fact that the quality assurance is done for each patient, and it does not include the quality assurance that is specific to the linac, the multileaf collimator (MLC) or the treatment planning system. The goal of the patient-specific quality assurance is to make dosimetric verifications of the IMRT plan calculated by the treatment planning system (Low, 2002). The patient-specific quality assurance sometimes does not involve any chamber measurement (Létourneau *et al.*, 2004; Both *et al.*, 2007), but ionisation chambers and films are still the gold standards.

Others have investigated different methods of quality assurance with varied results. Spezi *et al.* (2005) and Poppe *et al.* (2007) studied another way to perform the quality assurance with the use of a 2D array of ionisation chambers for IMRT dose verification. However, their results still depend on the size of the chambers, as explained below, to detect small misalignments between the measurements of dose distributions and the calculated distributions. With a similar idea, recent enquiries have been made into the possibility of doing IMRT quality assurance with the built-in electronic portal imaging device (EPID) on linacs (Warkentin *et al.*, 2003; Steciw *et al.*, 2005; Winkler *et al.*, 2005).

Even though it is the preferred method, the use of ionisation chambers for the patient-specific quality assurance of IMRT has inherent problems that have yet to be solved. The irregular conditions under which the IMRT beams are delivered differ dramatically from the reference conditions defined in the dosimetry protocols (Escudé *et al.*, 2006). The calibration coefficient $N_{D,\mathrm{w}}$ specified for each chamber under reference conditions can no longer be trusted to convert the signal of the ionisation inside the chamber cavity to the dose to water. This difficulty is allegedly circumvented by placing the ionisation chamber in a low dose gradient and high dose region of the phantom (Xia and Chuang, 2003). However, several issues generally arise from this solution. First, the size of the chamber may make it hard to find a low-dose-gradient region that envelopes its entire sensitive part. Furthermore, each beam of the treatment plan may not individually create a low-dose-gradient region where the chamber is placed, and there can even be very high dose gradients. The treatment planning system calculates that the addition of the successive beams will even out the dose gradients, but in practice inaccuracies in the movement of the MLC leaves and physical properties of the MLC unaccounted for by the treatment planning system, as seen earlier, can yield to high dose gradients in the chamber volume. Woo and Nico (2005) studied the impact of leaf positioning uncertainty on the measurements of IMRT fields with ion chambers. They found that it led to a poor reproducibility of the measurements, sometimes with relative reading variations of 13 %.

As a result of dose gradients, the point dose measurements often disagree with the treatment planning system, sometimes by up to 10 %. Discrepancies are usually attributed to tongue-and-groove effect and to positioning uncertainties of the chamber in high dose gradient regions (LoSasso *et al.*, 2001). These discrepancies are a sign that transient charged particle equilibrium can be locally violated in the chamber volume, and that the value of $N_{D,\mathrm{w}}$ under the IMRT conditions is not the same as that under reference conditions.

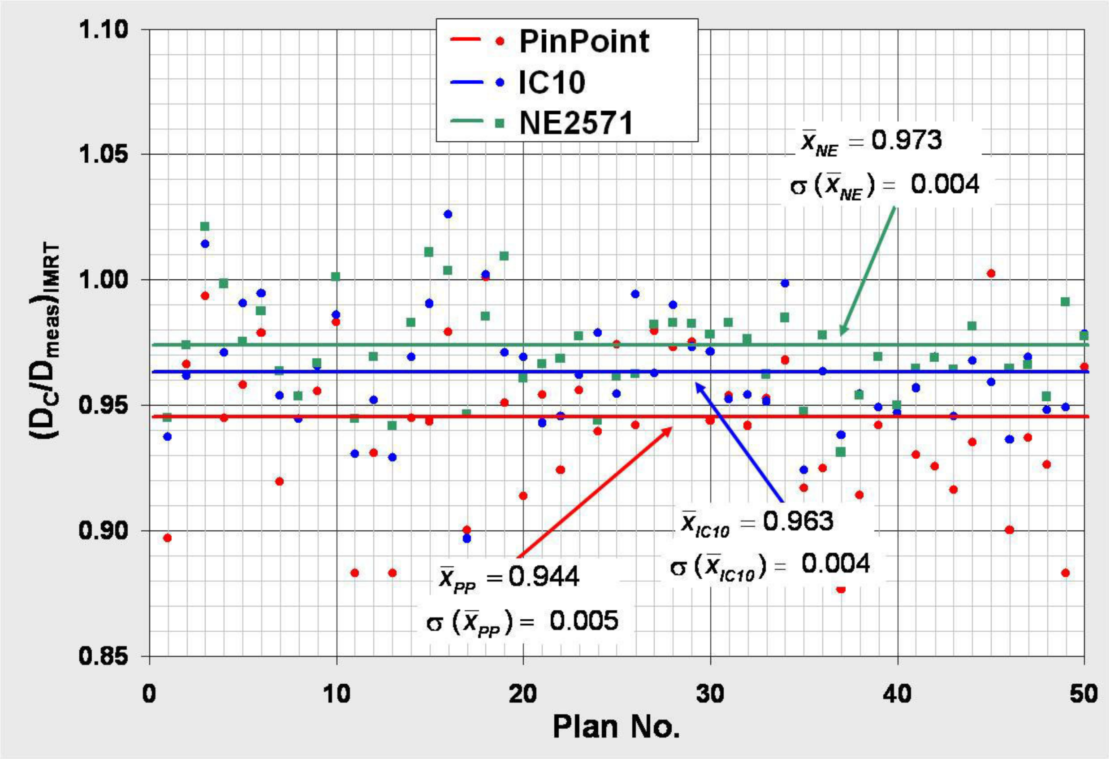

Figure 1.5: Comparison of measurements with three different ionisation chambers to CORVUS® treatment planning system for 50 IMRT plans. The chamber measurements all differ from CORVUS, but they also significantly differ from each other (Fraser *et al.*, 2005).

Fraser *et al.* (2005) further investigated the chamber inaccuracy issue by performing point dose measurements with three different ionisation chamber types for 50 IMRT plans calculated with the treatment planning system CORVUS®. Each measurement with each chamber type is highly reproducible, therefore error bars are not shown on the figure because they are negligible compared to the standard deviations of the point distributions over the 50 plans. Figure 1.5 shows that not only the measurements with the chambers differ from the treatment planning system calculation, but they also significantly differ from each other.

This is a strong sign that chamber responses depend on the chamber geometry. In other words, it is believed that the value of $N_{D,\mathrm{w}}$ for a given IMRT plan depends on the chamber geometry (Bogner *et al.*, 2004). In relation to this problem, it was claimed that restricted stopping power ratios in reference protocols, which are included in the expression of the calibration factor $N_{D,\mathrm{w}}$, could be used even in IMRT conditions for 6 MV photon beams. However, the same ratio relatively changed by 1.1 % for 25 MV photon beams (Sánchez-Doblado *et al.*, 2003).

The main limitation of ion chambers seems to be their relatively large size. Since dose gradients are always present in modulated fields because of the MLC, there is generally insufficient dose uniformity for accurate ion chamber measurements. Arnfield *et al.* (2001) claim that the use of miniature ion chambers has the potential to significantly reduce errors due to volume averaging. The chamber volume effect was studied by Escudé *et al.* (2006) who found that discrepancies are lower when using a small chamber because of the volume-averaging effects. Leybovich *et al.* (2003) also compared ion chambers with different volumes and concluded that only small volume chambers were suitable for the quality assurance of IMRT with dynamic MLC. Martens *et al.* (2000) studied the advantages of using a small volume ion chamber for IMRT measurement in spite of the effects of dose volume averaging and the broadening of the penumbra. Stasi *et al.* (2004) also argue for the use of ion chambers with small volumes, *i.e.*, less than 0.1 cm^3. Buckley *et al.* (2003) investigated the Spencer-Attix cavity theory for ion chambers with EGSnrc. They found a relative difference of 0.6 % between the simulation and the Spencer-Attix prediction, for chambers with walls made of one element, with the usual energy cut-off of 10 keV. All these studies above reduce the problem of dose gradients in ion chambers by reducing the chamber volume. However, they do not eliminate the problem, and they disregard any other characteristics of the chamber, *e.g.*, its shape, its material make-up, that could perturb the measurements. Furthermore, small chambers usually have significant polarity effects, and the relative magnitude of leakage signal is larger than for standard thimble-type chambers

To circumvent this difficulty with ion chambers, Monte Carlo application to IMRT QA has been studied, but the simulation is perturbed by the artefacts from the CT, the need of the Monte Carlo to convert dose to water to dose to material, and the difficulty to reach a good statistical accuracy in a reasonable amount of time (Pawlicki and Ma, 2001). The last point, however, evolves very rapidly thanks to the technological progress of computers. Very recently, Tyagi *et al.* (2007) studied the possibility to replace IMRT dose verifications done with chamber and film with a Monte-Carlo calculation taking into account the complex geometry of the MLC. They found an overall agreement within 2 %/2 mm of the film data for all IMRT beams except a head and neck split field, which showed differences up to 5 % in the high dose regions.

Still with Monte Carlo simulation, Bouchard and Seuntjens (2004) and Capote *et al.* (2004) independently introduced a correction factor to correct the ionisation chamber calibration factor $N_{D,\mathrm{w}}$ for IMRT conditions. They calculated IMRT correction factors with a rectangular parallelepipedic air cavity or a simple model of ion chamber. They already obtained good results and measured correction factors varying from 0.88 to 1.15 for an extreme variety of dynamic IMRT fields. Therefore, they both invalidated the application of reference dosimetry protocol data for the derivation of absorbed dose to water from ionisation chamber measurements. This correction factor was later used to study dose errors in PTV and OAR in prostate carcinoma, using a micro-ionisation chamber, in step-and-shoot mode (Sánchez-Doblado *et al.*, 2005a,b). Within these conditions, they found corrections of up to 6 % with an uncertainty of about 3 %. A recent study by the same team compared corrections factors of three different ion chambers for IMRT fields in both step-and-shoot and dynamic delivery modes. For small chambers, they claim a correction factor for non-reference conditions of 1 % to 1.5 % (Sánchez-Doblado *et al.*, 2007).

1.4 Thesis objective

The goal of this thesis is to show that all the characteristics of an ion chamber can be modelled in a Monte-Carlo simulation using the pencil-beam kernel formalism. This work also shows how the results from the simulation compared to experimental measurements.

This thesis presents a realistic model of the Exradin® A12 Farmer chamber, which is used for point dose verifications of IMRT plans at the Montreal General Hospital. The Monte-Carlo EGSnrc user code CAVITY that can use this complex geometry is tested against the well-known user code CAVRZnrc. Then, the chamber model is tested in reference conditions, and the results are compared to those in the report TG-51 (Almond *et al.*, 1999).

Using the same pencil-beam kernel formalism as Bouchard and Seuntjens (2004), kernels are simulated with CAVITY for ^{60}Co and 6 MV beams. The sampled dose responses are interpolated to obtain detailed dose kernels. The kernel summation method is tested against direct simulations in reference conditions. We show the importance of accuracy in the computation of the variance of the kernel summation. Finally, the kernel summation method is used with open fields and IMRT fields to quantify the chamber response. The results are compared to experimental data performed on a Varian® Clinac 6EX.

Chapter 2 presents the physics of photon and electron transport through matter. In particular, electron stopping powers are introduced. Concepts and methods of dosimetry are presented in Chapter 3. Ionisation chamber dosimetry protocols and calibration factors are introduced in that chapter. The materials and methods used in our analysis are then reviewed in Chapter 4. The results follow in Chapter 5. Finally, after the conclusion in Chapter 6, the details of the calculation of kernel summation variance are presented in Appendix A.

Chapter 2

Physics of Ionising Radiation

Radiation is of the ionising type if it can ionise matter. Ionisation is the process in which a neutral atom acquires or loses one or several electrons, so that its electric charge becomes either negative or positive. There are two types of ionising radiation:

- *Directly ionising.* Charged particles, *e.g.*, electrons, positrons, α particles, protons, are described as directly ionising radiation. They deposit their energy in the medium through Coulomb interactions with the orbital electrons.

- *Indirectly ionising.* Uncharged particles, *e.g.*, photons and neutrons, interact with the medium where charged particles are released (electrons or positrons are released by photons; protons and heavy ions are released by neutrons). The released charged particles, usually called *secondary charged particles*, deposit their energy in the medium through Coulomb interactions with the orbital electrons.

Both types of radiation are used in radiotherapy, and the most common particles used are photons and electrons. It is then necessary to understand how these particles interact with matter in order to be able to make dosimetric predictions and deliver the right amount of radiation when treating patients. Other particles, *e.g.*, protons, neutrons and heavy ions, are also used in radiotherapy (Smith, 2006; Podgoršak, 2005b). However their usage is not widespread, and it is outside the scope of this work since IMRT is usually delivered with photons.

2.1 Photon Interaction with Matter

2.1.1 Rayleigh Scattering

Lord Rayleigh developed in 1899 a classical theory of the scattering of electromagnetic radiation by atoms to explain the colour of the sky (Rayleigh, 1899). In his theory and later developments, photons are scattered by the orbital bound electrons of the atoms. The photon is scattered at an angle θ with essentially no energy loss in the process, *i.e.*, with the same wavelength. The negligible energy transferred to the atom as a whole is only recoil energy, and the atom is not excited. The fact that the scattered photon keeps the same wavelength is the reason why the interaction is also called *coherent scattering*.

Rayleigh (coherent) scattering happens mostly with low energy photons and for high Z atoms in the medium. Because all the orbital electrons contribute to absorb the recoil energy, the Rayleigh atomic cross section is greater at low energies than the Compton atomic cross section. Compton scattering will be developed in section 2.1.3 on page 21.

The differential atomic cross section $\frac{d_{\mathrm{a}}\sigma_{\mathrm{R}}}{d\Omega}$ for Rayleigh scattering is given by:

$$\frac{d_{\mathrm{a}}\sigma_{\mathrm{R}}}{d\Omega} = \frac{r_{\mathrm{e}}^2}{2}\left(1+\cos^2\theta\right)F^2(x,Z)\ , \tag{2.1}$$

where

r_{e} is the classical radius of the electron,
θ is the scattering angle,
$x = \frac{\sin\frac{\theta}{2}}{\lambda}$ is the momentum transfer variable,
λ is the photon wavelength,
$F(x,Z)$ is the atomic form factor.

The atomic form factor $F(x,Z)$ is difficult to calculate, but it is equal to Z for low scattering angles θ and tends to 0 at large angles.

Although there is no energy transfer involved in Rayleigh scattering, it is important to take this interaction into account, especially at low energies, because it contributes to the attenuation of the photon beam.

2.1.2 Photoelectric Effect

In the photoelectric interaction, a photon is totally absorbed by a tightly bound orbital electron that is ejected from the atom (see Figure 2.1a). The ejected electron is then called a *photoelectron*. The photoelectric effect is an ionising process because it creates a vacancy in the atom. The vacancy will be filled either by a free electron from the medium or by a bound electron of the cloud. In both cases, the electron will lose some of its energy most of the time by emitting a characteristic photon. This is called *fluorescence* (see Figure 2.1b). The electron may also transfer its transition energy to another electron of the cloud that in turn will be ejected from the atom. This effect is called *Auger effect* after Pierre Auger who studied it in his doctoral thesis (Auger, 1926), but the phenomenon was discovered in 1923 by the Austrian physicist Lise Meitner. The *Coster-Kronig* and *super Coster-Kronig* effects are special cases of the Auger effect. In the Coster-Kronig effect, the vacancy is filled by an electron of a higher subshell of the same shell, and the transition energy is transferred to an electron in a higher shell, whereas in the super Coster-Kronig effect the transition energy is transferred to an electron in the same shell. As the Auger effect only changes the position of the vacancy in the atom, it may lead to fluorescence.

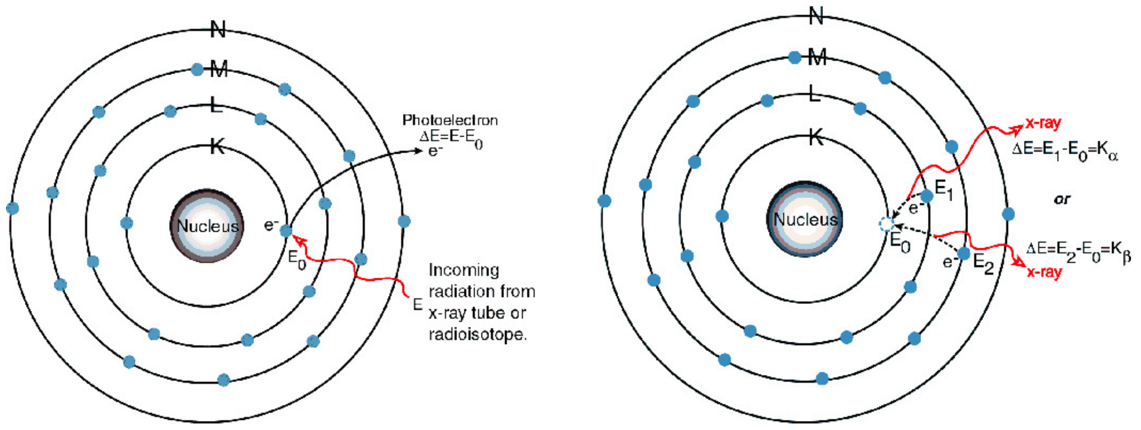

(a) Photoelectric effect on K shell of an atom.

(b) Atomic relaxation leading to fluorescence.

Figure 2.1: (a) Diagram representing a photoelectric effect on the K shell of an atom. (b) Diagram representing the relaxation of the ionised atom leading to fluorescence. From `http://mxp.physics.umn.edu/s04/Projects/s04xrf/theory.htm` (last visited: 2007/06/22).

Fluorescence and Auger effect are competing processes in *atomic relaxation*. The fluorescent yield ω for a given shell is defined as the number of characteristic photons emitted divided by the number of vacancies on the given shell. Figure 2.2 shows the fluorescent yield for the shells K and L as a function of the atomic number. We can observe that ω_{K} significantly increases with Z and approaches 1 for high Z materials.

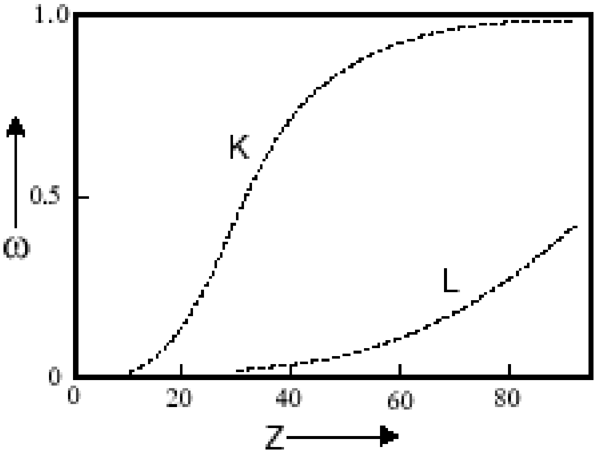

Figure 2.2: Fluorescent yield for the K and L shells as a function of the atomic number Z. From `http://www4.nau.edu/microanalysis/Microprobe/Interact-Auger.html` (last visited: 2007/06/22).

The photoelectric atomic cross section is noted ${}_{\mathrm{a}}\tau$, and it depends on both the photon energy and the atomic number Z of the atom. Its representation as a function of the incident photon energy (Figure 2.3) shows sharp discontinuities when the photon energy is equal to the electron binding energy of a particular shell. The graph also shows the fine structure of all shells but the K shell.

The expression of ${}_{\mathrm{a}}\tau$ depends on whether we are near an absorption edge, at some distance of it, or at high energy far above the K edge energy. There are no theoretical predictions for the first energy region, and physicists rely on experimental values. For the second and third energy regions, the energy dependence is assumed to go as $(\frac{1}{h\nu})^3$ for low energy, gradually changing to $\frac{1}{h\nu}$ at high energy. The Z dependence also varies, and ${}_{\mathrm{a}}\tau$

goes as Z^4 at low energy and as Z^5 at high energy. However, in energy regions where the photoelectric effect is predominant, the Z and energy dependence of ${}_{\mathrm{a}}\tau$ is usually written as follows:

$$ {}_{\mathrm{a}}\tau \propto \frac{Z^4}{(h\nu)^3} \,. \tag{2.2}$$

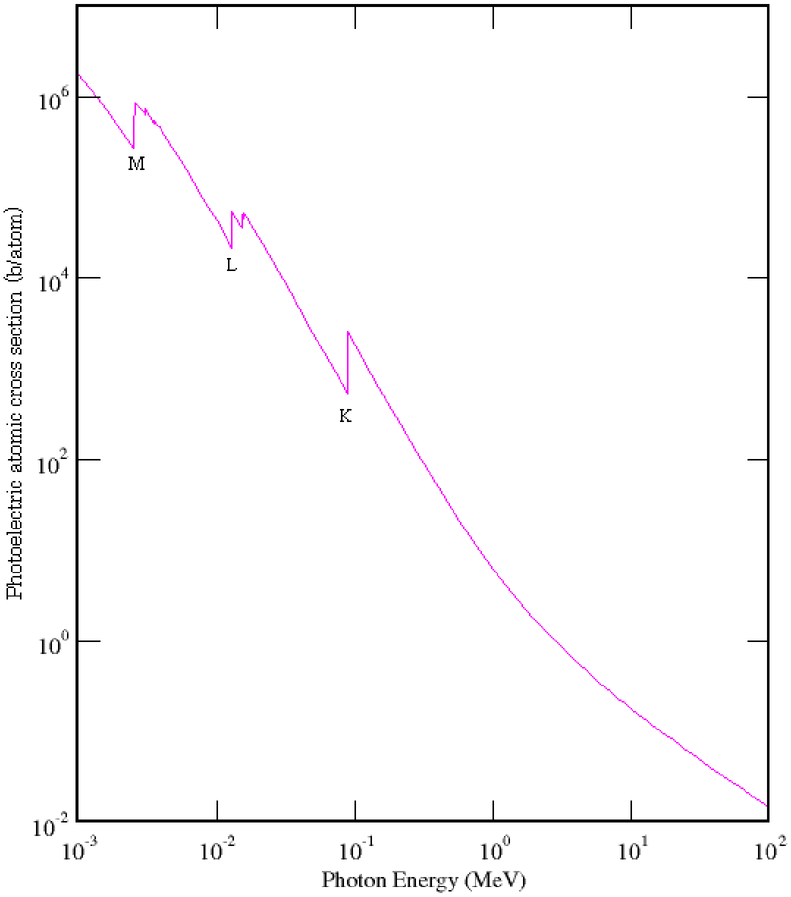

Figure 2.3: The photoelectric atomic cross section ${}_{\mathrm{a}}\tau$ of lead. The absorption edges of shells K, L and M can be observed. The K absorption edge is at 88 keV. Data from NIST.

The photoelectron leaves the atom with a kinetic energy $E_{\mathrm{K}} = h\nu - E_{\mathrm{B}}$ where E_{B} is the binding energy for the shell where the photoelectron is coming from. For this simple equation (Einstein, 1905), A. Einstein received the Nobel prize in 1921 because he had postulated that light interacts with matter as discrete quanta of energy, a revolutionary idea at a time when physicists only considered light to be a wave.

Most of the time, if the photon energy is higher than the binding energy of the K shell, the vacancy is created on the K shell and the photoelectron kinetic energy is $E_{\mathrm{K}} = h\nu - E_{\mathrm{B}}(\mathrm{K})$. However, when we want to calculate the mean energy transfer $\overline{E}^{\tau}_{\mathrm{tr}}$ for the photoelectric effect, we have to take into account the Auger electrons that may be produced, depending on the fluorescent yield w_{K}. In the general case, $\overline{E}^{\tau}_{\mathrm{tr}}$ is between $h\nu - E_{\mathrm{B}}(\mathrm{K})$ and $h\nu$.

The general expression of the mean energy transfer is:

$$\overline{E}^{\tau}_{\mathrm{tr}} = h\nu - P_{\mathrm{K}}\omega_{\mathrm{K}}\overline{h\nu}_{\mathrm{K}}\,, \tag{2.3}$$

where

P_{K} is the probability that the photon with an energy greater than $E_{\mathrm{B}}(\mathrm{K})$ creates a vacancy on the K shell. P_{K} is typically between 0.8 and 1;

ω_{K} is the fluorescent yield of the K shell;

$\overline{h\nu}_{\mathrm{K}}$ is the weighted mean value of all possible fluorescent transition energies down to the K shell. Typically, we usually have $\overline{h\nu}_{\mathrm{K}} \approx 0.86 E_{\mathrm{B}}(\mathrm{K})$.

2.1.3 Compton Scattering

Before Arthur H. Compton, physicists were puzzled by the fact that the wavelength of scattered X-rays depends on the scattering angle. The American physicist worked for three years on this problem until, in late 1922, he came up with a simple solution that involved both special relativity and quantum physics at a level that was scarcely understood at the time (Compton, 1923).

Compton scattering describes the interaction of a photon with a free electron (Figure 2.4). In an atom, the electron is considered as free, or loosely bound, when its binding energy is much smaller than the energy of the incoming photon. The photon loses part of its energy and is scattered at an angle θ. The energy is transferred to the recoil electron.

From the equations representing the conservation of the total energy-momentum quadrivector, we can derive the expression of the photon wavelength shift:

$$\Delta\lambda = \lambda' - \lambda = \lambda_{\mathrm{C}}(1 - \cos\theta)\,, \tag{2.4}$$

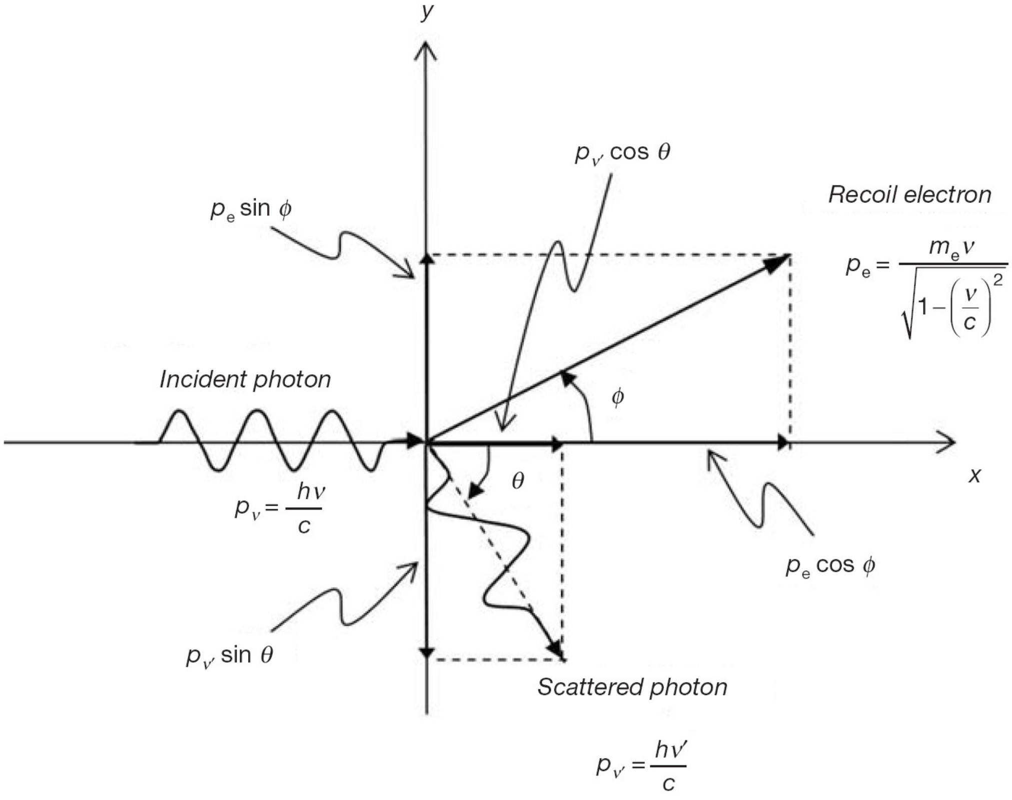

Figure 2.4: Diagram of Compton scattering. A photon with energy $h\nu$ is scattered by a loosely bound atomic electron. The Compton recoil electron is ejected from the atom with the kinetic energy E_K, and the outcoming photon leaves at the angle θ with the energy $h\nu' = h\nu - E_K$. From Podgoršak (2005a).

where λ_C is the Compton wavelength of the electron:

$$\lambda_C = \frac{h}{m_e c} . \tag{2.5}$$

The differential electronic cross section for the Compton effect was first derived by Oskar Klein and Yoshio Nishina (Klein and Nishina, 1929), and its expression for the scattering on a free electron is given by:

$$\frac{d_e\sigma_C^{KN}}{d\Omega} = \frac{r_e^2}{2}(1+\cos^2\theta)F_{KN} , \tag{2.6}$$

where

$\frac{d_{\mathrm{e}}\sigma_{\mathrm{C}}^{\mathrm{KN}}}{d\Omega}$ is the Klein-Nishina differential electronic cross section for the Compton effect,

r_{e} is the classical electron radius,

θ is the scattering angle of the photon,

F_{KN} is the Klein-Nishina form factor.

The Klein-Nishina form factor F_{KN} for a free electron is given as follows:

$$F_{\mathrm{KN}} = \left(\frac{1}{1+\epsilon(1-\cos\theta)}\right)^2 \left(1 + \frac{\epsilon^2(1-\cos\theta)^2}{[1+\epsilon(1-\cos\theta)]\,(1+\cos^2\theta)}\right) , \qquad (2.7)$$

where $\epsilon = \frac{h\nu}{m_{\mathrm{e}}c^2}$ is the incoming photon energy normalised to the electron rest energy.

Equation 2.6 can be integrated, and the Klein-Nishina total electronic cross section for Compton scattering can be expressed as follows:

$$\begin{aligned} {}_{\mathrm{e}}\sigma_{\mathrm{C}}^{\mathrm{KN}} &= \int \frac{d_{\mathrm{e}}\sigma_{\mathrm{C}}^{\mathrm{KN}}}{d\Omega} d\Omega & (2.8) \\ &= 2\pi r_{\mathrm{e}}^2 \left[\frac{1+\epsilon}{\epsilon^2}\left(\frac{2(1+\epsilon)}{1+2\epsilon} - \frac{\ln(1+2\epsilon)}{\epsilon}\right) + \frac{\ln(1+2\epsilon)}{2\epsilon} - \frac{1+3\epsilon}{(1+2\epsilon)^2}\right] . & (2.9) \end{aligned}$$

For low energies, *i.e.*, when ϵ tends to 0, the cross section in the equation above tends to the classical Thomson result ${}_{\mathrm{e}}\sigma_{\mathrm{Th}} = \frac{8\pi}{3} r_{\mathrm{e}}^2 = 0.665$ b. For all energies, the total Compton cross section is always lower than the classical Thomson cross section.

The Klein-Nishina cross section is only valid when the electron is free or loosely bound, *i.e.*, when the electron binding energy is negligible compared to the energy transfer. At low energy, the effect of the electron binding energy is high, and the Compton cross section drops. John Hubbell, from the National Institute of Standards and Technology, developed a method to correct the Klein-Nishina cross section for the binding energy effect. A correction function, $S(x, Z)$, called *incoherent scattering function*, is applied to the Klein-Nishina electronic differential cross section to get the atomic differential cross section:

$$\frac{d_{\mathrm{a}}\sigma_{\mathrm{C}}}{d\Omega} = \frac{d_{\mathrm{e}}\sigma_{\mathrm{C}}^{\mathrm{KN}}}{d\Omega} S(x, Z) , \qquad (2.10)$$

where $x = \frac{1}{\lambda}\sin\frac{\theta}{2}$ is the momentum transfer variable.

For high momentum transfers, $S(x, Z)$ tends to Z, simply translating the fact that when the electrons are loosely bound to the atom, the atomic differential cross section is equal to Z times the electronic differential cross section. On the other hand, when the momentum transfer x decreases, $S(x, Z)$ decreases, and for $x = 0.01$ Å^{-1} it is already less than 1 % of Z.

The correction is important for photon energies of the order of the electron binding energy. However, at these energies, the photoelectric effect and Rayleigh scattering are much more dominant than Compton scattering. Therefore, it does not matter if one ignores the electron binding effect at low energies when determining the total cross section for photon interactions. The photoelectric effect and Rayleigh scattering contribute almost totally to the total cross section.

When the electron is loosely bound, the energy E_{K} transferred to the recoil electron and the outcoming photon energy $h\nu'$ are easy to derive from Equation 2.4, and they are expressed as follows:

$$\begin{aligned} E_{\mathrm{K}} &= h\nu \frac{\epsilon(1-\cos\theta)}{1+\epsilon(1-\cos\theta)} \,, && (2.11) \\ h\nu' &= h\nu \frac{1}{1+\epsilon(1-\cos\theta)} \,. && (2.12) \end{aligned}$$

The maximum energy transferred to the electron happens when $\theta = \pi$, and it is given by the following:

$$E_{\mathrm{K}}^{\max} = h\nu \frac{2\epsilon}{1+2\epsilon} \,. \qquad (2.13)$$

The mean energy transferred to the electron is defined as:

$$\begin{aligned} \overline{E_{\mathrm{K}}} &= h\nu \frac{({}_{\mathrm{e}}\sigma_{\mathrm{C}}^{\mathrm{KN}})_{\mathrm{tr}}}{{}_{\mathrm{e}}\sigma_{\mathrm{C}}^{\mathrm{KN}}} && (2.14) \\ &= \frac{\int \frac{d_{\mathrm{e}}\sigma_{\mathrm{C}}^{\mathrm{KN}}}{d\Omega} E_{\mathrm{K}} d\Omega}{\int \frac{d_{\mathrm{e}}\sigma_{\mathrm{C}}^{\mathrm{KN}}}{d\Omega} d\Omega} && (2.15) \\ &= h\nu \frac{\int (1+\cos^2\theta) \frac{\epsilon(1-\cos\theta)}{1+\epsilon(1-\cos\theta)} F_{\mathrm{KN}} d\Omega}{\int (1+\cos^2\theta) F_{\mathrm{KN}} d\Omega} \,. && (2.16) \end{aligned}$$

After integration of both integrals in the previous equation, the mean fraction of energy of the incoming photon transferred to the Compton electron can be expressed by:

$$\frac{\overline{E_{\mathrm{K}}}}{h\nu} = \frac{\frac{2(1+\epsilon)^2}{\epsilon^2(1+2\epsilon)} - \frac{1+3\epsilon}{(1+2\epsilon)^2} - \frac{(1+3\epsilon)(2\epsilon^2-2\epsilon-1)}{\epsilon^2(1+2\epsilon)^2} - \frac{4\epsilon^2}{3(1+2\epsilon)^3} - \left(\frac{1+\epsilon}{\epsilon^3} - \frac{1}{2\epsilon} + \frac{1}{2\epsilon^3}\right)\ln(1+2\epsilon)}{\frac{1+\epsilon}{\epsilon^2}\left(\frac{2(1+\epsilon)}{1+2\epsilon} - \frac{\ln(1+2\epsilon)}{\epsilon}\right) + \frac{\ln(1+2\epsilon)}{2\epsilon} - \frac{1+3\epsilon}{(1+2\epsilon)^2}} \qquad (2.17)$$

Both $\frac{E_{\mathrm{K}}^{\max}}{h\nu}$ and $\frac{\overline{E_{\mathrm{K}}}}{h\nu}$ are plotted in Figure 2.5.

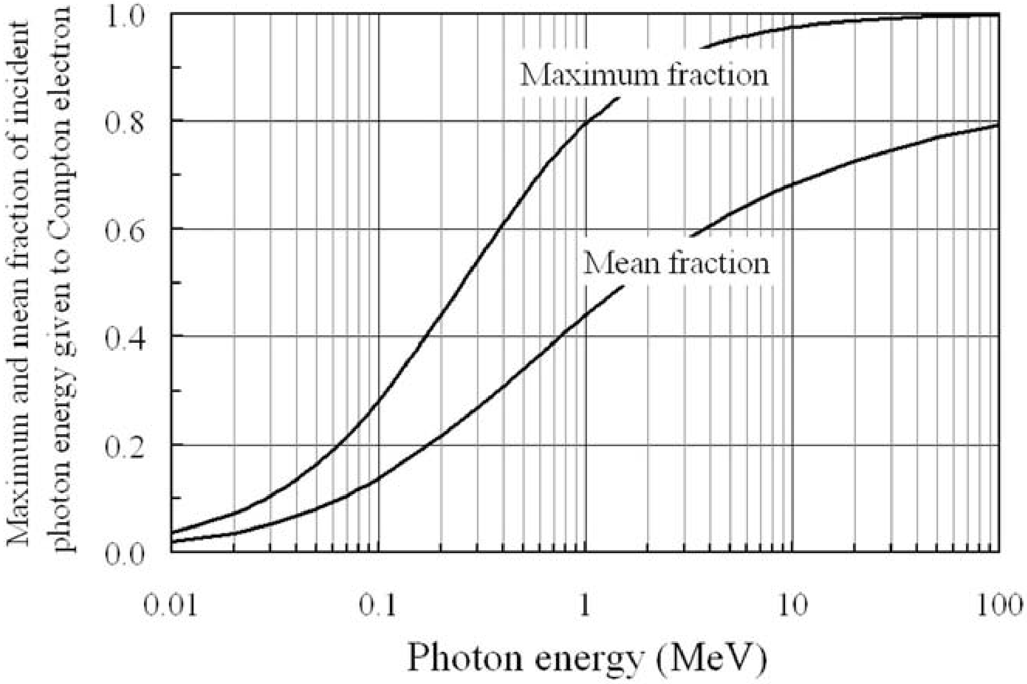

Figure 2.5: Maximum and mean fractions of energy transferred to the recoil Compton electron as a function of the incoming photon energy, in the case of a loosely bound electron. From Podgoršak (2005a).

2.1.4 Pair Production

It is possible to create a pair electron-positron if we provide at least twice the rest mass-energy of the electron, *i.e.*, 1.02 MeV. Only a photon can provide this energy while conserving charge numbers, especially the electric charge. However, to conserve energy and momentum, the photon alone cannot annihilate in free space to produce a pair electron-positron. It can easily be understood if we consider the fact that the photon has no mass, and therefore, there does not exist any frame where the photon is at rest. To annihilate, the photon must interact with the electric field of either a nucleus or an atomic electron. The former case is called *pair production*, whereas the latter is referred to as *triplet production* because some energy is transferred to the recoil electron, which is then ejected from the atom, along with the newly created electron and positron.

The atomic cross section for general pair production is noted ${}_{\mathrm{a}}\kappa$. It can be written as the sum of two contributions from the pair production cross section ${}_{\mathrm{a}}\kappa_{\mathrm{pp}}$ and the triplet production cross section ${}_{\mathrm{a}}\kappa_{\mathrm{tp}}$. The triplet production cross section ${}_{\mathrm{a}}\kappa_{\mathrm{tp}}$ can be further expressed as a function of ${}_{\mathrm{a}}\kappa_{\mathrm{pp}}$, and we can write:

$$ {}_{\mathrm{a}}\kappa = {}_{\mathrm{a}}\kappa_{\mathrm{pp}} + {}_{\mathrm{a}}\kappa_{\mathrm{tp}} = {}_{\mathrm{a}}\kappa_{\mathrm{pp}} \left(1 + \frac{1}{\eta Z}\right) \tag{2.18} $$

where η is a parameter depending on $h\nu$.

The general expression for the photon threshold energy for pair or triplet production is:

$$ h\nu_{\mathrm{thr}} = 2m_{\mathrm{e}}c^2 \left(1 + \frac{m_{\mathrm{e}}}{m_{\mathrm{A}}}\right) , \tag{2.19} $$

where m_{e} and m_{A} are the mass of the electron and the mass of the object interacting with the photon, respectively. The formula is simply derived from the conservation of the total energy and momentum of the system. For pair production, where the electron mass is considered negligible to the nucleus mass, the threshold energy is therefore $h\nu_{\mathrm{thr}} = 2m_{\mathrm{e}}c^2 = 1.022$ MeV. For triplet production, the threshold energy is $h\nu_{\mathrm{thr}} = 4m_{\mathrm{e}}c^2 = 2.044$ MeV[1].

If we ignore the negligible recoil energy of the nucleus, the total kinetic energy transferred to charged particles in the pair production process is given by:

$$ \overline{E_{\mathrm{tr}}^{\mathrm{pp}}} = h\nu - 2m_{\mathrm{e}}c^2 . \tag{2.20} $$

This transferred energy is shared by the electron and the positron. In average, the electron and positron equally share the transferred energy.

The positron, in turn, slows down and loses energy in successive collisions and radiative losses (Section 2.2). Eventually, when nearly at rest, it interacts with an electron, and both annihilate, creating two photons leaving in opposite directions with $h\nu = m_{\mathrm{e}}c^2 = 511$ keV. In about 2 % of the cases, though, the positron may annihilate before losing all its energy. It is referred to as *annihilation in flight*. Depending on whether it interacts with a tighly bound or a free[2] electron, one or two photons are created. In the former case, the nucleus

---

[1] Hubbell (2006) remarks that triplet production can actually happen down to $2m_{\mathrm{e}}c^2$ because momentum can be transferred to the atom in excitation or ionisation. However, the cross section in this energy region is negligible.

[2] "Free" is used here for "loosely bound", *i.e.*, when the electron binding energy is negligible compared to the positron kinetic energy.

picks up the recoil momentum, and one photon is created with essentially the positron total energy. In the latter case, two photons are created with different energies $h\nu_1$ and $h\nu_2$.[3] When the kinetic energy of the positron E_K is much greater than $m_\mathrm{e}c^2$, the decay photons leave with the energies $h\nu_1 = E_\mathrm{K} + \frac{3}{2}m_\mathrm{e}c^2$ and $h\nu_2 = \frac{1}{2}m_\mathrm{e}c^2$.

2.1.5 Photodisintegration

To complete this section on photon interaction with matter, we must mention photodisintegration, although it is the least important process involving photons. Photodisintegration involves an energetic photon directly interacting with a nucleus of the medium. The reaction generally produces a neutron, called *photoneutron*, that is ejected from the nucleus.

For the reaction to occur, the photon energy must overcome the nuclear binding energy of 8 MeV or more. The two exceptions are the reactions $^{2}\mathrm{H}(\gamma,\mathrm{n})^{1}\mathrm{H}$ and $^{9}\mathrm{Be}(\gamma,\mathrm{n})2\alpha$, for which the neutron binding energies are only 2.22 MeV and 1.67 MeV, respectively. There is a giant resonance at about 12 MeV for high Z materials, and 24 MeV for low Z materials. The resonance has a width ranging from 3 MeV to 9 MeV.

The shape and magnitude of the resonance irregularly depends on both A and Z, and the cross section is therefore difficult to calculate. This is the reason why the cross section is generally omitted in medical physics calculations, although at the resonance peak, the cross section ${}_\mathrm{a}\sigma_\mathrm{ph.n.}$ may contribute from 2 % to 6 % to the total cross section, for high Z and low Z materials, respectively (Hubbell, 2006).

Even if the photodisintegration is not usually taken into account into cross section calculations, the phenomenon is however considered seriously in the design of treatment facilities. Indeed, the neutrons produced in this reaction are energetic and induce radioactivity in the treatment room air and in the machine components. Neutrons and radioactivity present a health hazard to the personnel, and it is necessary to deal with both. Borated hydrogenous materials are incorporated in treatment room doors to thermalise and absorb the neutrons. To deal with the radioactivity, the air of the treatment room is renewed every 7 to 10 min, and the machine components are made of materials with low photodisintegration cross

---

[3] This is actually the same case as when the positron annihilates at rest, except that the lab frame does not coincide with the centre-of-mass frame of the electron-positron system.

sections and short product half-life.

2.1.6 Attenuation coefficients

The sum of all the atomic cross sections for photon interactions is the *total atomic cross section* ${}_\mathrm{a}\mu$ usually expressed in barns (1 b = 10^{-28} m^2):

$$ {}_\mathrm{a}\mu = {}_\mathrm{a}\sigma_\mathrm{R} + {}_\mathrm{a}\tau + {}_\mathrm{a}\sigma_\mathrm{C} + {}_\mathrm{a}\kappa \left(+{}_\mathrm{a}\sigma_\mathrm{ph.n.}\right). \tag{2.21} $$

More commonly, the *linear attenuation coefficient* μ, expressed in cm^{-1}, is used. Let a monoenergetic photon beam from a narrowly collimated source be attenuated by a thickness x of material, and its intensity $I(x)$ be measured by a narrowly collimated detector. The intensity is expressed as follows:

$$ I(x) = I(0)e^{-\int_0^x \mu dx'} \tag{2.22} $$

where $I(0)$ is the intensity measured without any material.

The linear attenuation coefficient μ is related to the total atomic cross section ${}_\mathrm{a}\mu$:

$$ \mu = \rho \frac{\mathcal{N}_\mathrm{A}}{A} {}_\mathrm{a}\mu \tag{2.23} $$

where

ρ is the density of the material,
$\mathcal{N}_\mathrm{A}$ is Avogadro's number,
A is the atomic mass,.

The importance of each contribution to the linear attenuation coefficient depends on both the photon energy $h\nu$ and the atomic number Z. For $h\nu < 1$ MeV, there is a competition between the photoelectric effect and the Compton effect. The higher Z, the more predominant the photoelectric effect. For energies between 1 MeV and 4 MeV, the Compton effect is predominant, whatever Z. For energies higher than 4 MeV, pair production becomes the most important interaction for increasing Z. The predominance regions for each type of interaction are shown in Figure 2.6.

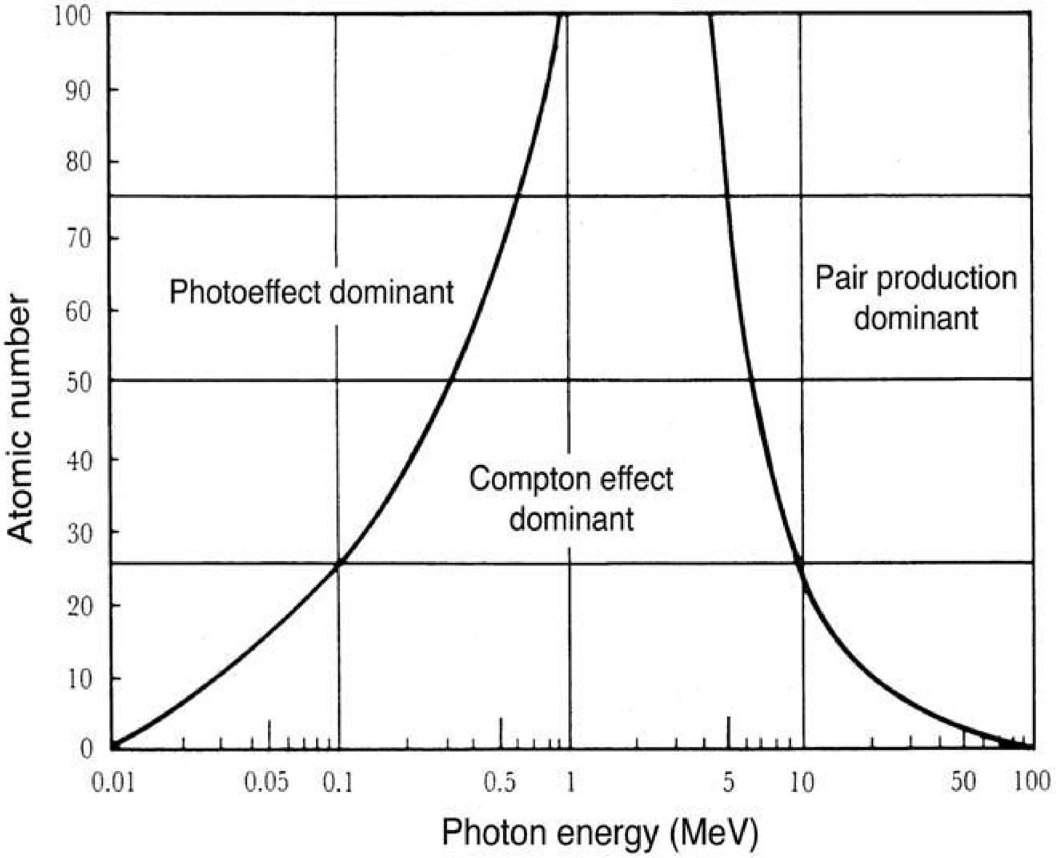

Figure 2.6: Regions of predominance of the three main photon interactions. The curves represent the regions where the interactions on each side have equal atomic cross sections. From Podgoršak (2005a)

Two other useful quantities are the *energy transfer coefficient* μ_{tr}, and the *energy absorption coefficient* μ_{en}. The energy transfer coefficient is defined as:

$$\mu_{\mathrm{tr}} = \rho \frac{\mathcal{N}_{\mathrm{A}}}{A} \left({}_{\mathrm{a}}\tau \frac{\overline{E_{\mathrm{tr}}^{\tau}}}{h\nu} + {}_{\mathrm{a}}\sigma_{\mathrm{C}} \frac{\overline{E_{\mathrm{K}}}}{h\nu} + {}_{\mathrm{a}}\kappa \frac{\overline{E_{\mathrm{tr}}^{\mathrm{pp}}}}{h\nu} \right) \tag{2.24}$$

where

$h\nu$ is the photon energy,

$\overline{E_{\mathrm{tr}}^{\tau}}$ is the mean energy transferred in the photoelectric effect and is approximated by $h\nu - P_{\mathrm{K}}\omega_{\mathrm{K}}E_{\mathrm{B}}(\mathrm{K})$,

$\overline{E_{\mathrm{K}}}$ is the mean energy transferred to the Compton electron, given in Figure 2.5 as a fraction of $h\nu$,

$\overline{E_{\mathrm{tr}}^{\mathrm{pp}}}$ is the mean energy transferred in pair production, equal to $h\nu - 2m_{\mathrm{e}}c^2$.

Rayleigh scattering does not appear in the expression of μ_{tr} because this interaction does not involve any energy transfer, as is explained in subsection 2.1.1.

The mean energy absorbed by the medium slightly differs from the mean energy transferred because the secondary charge particles may lose a fraction of their energy by radiative interactions when travelling through the medium. Electrons and positrons lose radiative energy through Bremsstrahlung, and the positrons may also yield radiative energy by annihilating in flight. The fraction of the mean energy transferred that is radiated is called *radiative fraction* and is noted $\overline{g}$. Using the radiative fraction definition, it is easy to define the energy absorption coefficient μ_{en} in terms of the energy transfer coefficient:

$$\mu_{\mathrm{en}} = \mu_{\mathrm{tr}}(1 - \overline{g})\,. \tag{2.25}$$

Finally, to be able to compare one medium to another, it is convenient to define and use the *mass attenuation coefficient* $\frac{\mu}{\rho}$, along with the *mass energy transfer coefficient* $\frac{\mu_{\mathrm{tr}}}{\rho}$ and the *mass energy absorption coefficient* $\frac{\mu_{\mathrm{en}}}{\rho}$. These coefficients are expressed in $\mathrm{cm}^2\cdot\mathrm{g}^{-1}$. They are particularly convenient in the Compton region where they are essentially independent[4] of Z.

2.2 Electron Interaction with Matter

Charged particles, and in particular electrons and positrons, experience Coulomb interactions with the nuclei and the atomic electrons as they travel through matter. It is natural to think that electrons and positrons interact individually with the nuclei and with the electrons of the cloud. However, the quantum nature of electrons and hadrons makes their behaviour more complex. In fact, the electron can undergo inelastic scattering on the atom, even though the atom is neutral as a whole. To that respect, we can distinguish three types on electron interaction:

---

[4] In the Compton region, $\frac{\mu}{\rho} \approx \mathcal{N}_{\mathrm{A}} \frac{Z}{A} {}_{\mathrm{e}}\sigma_{\mathrm{C}}$, and $\frac{Z}{A}$ can be considered as equal to 0.5.

- Inelastic Coulomb interaction with a nucleus leading to *Bremsstrahlung* production. The energy lost by the electron is emitted as radiation.

- *Hard collision*, a Coulomb interaction with an electron of the atom, when the impact parameter is of the order of the atom radius. The electron loses a non-negligible amount of energy, which will either excite an electron of the cloud or even eject it and ionise the atom. The ejected electron may have enough energy to follow its own track, in which case it is called a δ-ray. Hard collisions are known as *Møller scattering* in the case of an incident electron, and *Bhabha scattering* in the case of an incident positron.

- *Soft collision*, a Coulomb interaction with the whole atom, when the impact parameter is much larger than the atom radius. The electron loses a very small amount of energy that is transferred to the atom and the orbital electrons.

Electrons and positrons are small charged particles compared to the nuclei in the medium, and they experience a large number of interactions and changes of direction before they lose all their kinetic energy (or before they annihilate in the case of positrons).

2.2.1 Bremsstrahlung

Bremsstrahlung is a German term for “braking radiation”. This phenomenon describes the emission of light by any accelerated charged particle. Classically, the power emitted by the accelerated particle is given by the Larmor relationship:

$$P = \int |\mathbf{S}| \cdot d\mathbf{A} = -\frac{\mathrm{d}E}{\mathrm{d}t} = \frac{1}{6\pi\epsilon_0}\frac{q^2a^2}{c^3}\,, \tag{2.26}$$

where $\mathbf{S}$ is the Poynting vector, E is the energy of the charged particle, ϵ_0 is the permittivity of vacuum, q is the charged particle, a is the acceleration of the particle, and c is the speed of light. The radiation emitted is maximum at right angles to the direction of motion of the particle.

In the relativistic case, however, the norm of the Poynting vector, *i.e.*, the emitted radiation intensity $\mathcal{I}(r,\theta)$ becomes larger for forward emission angles:

$$|\mathbf{S}(r,\theta)| = \mathcal{I}(r,\theta) = \frac{1}{16\pi\epsilon_0}\frac{q^2a^2}{c^3r^2}\frac{\sin^2\theta}{(1-\beta\cos\theta)^5}\,, \tag{2.27}$$

where β is the velocity of the particle, r is the distance from the accelerated charged particle, and θ the radiation emission angle. As β increases, the intensity distribution of the emitted radiation becomes more and more forward-peaked. The maximum of intensity occurs at an angle θ_{max} whose typical values for electrons are 10.0° for a kinetic energy of 1 MeV, 1.4° at 10 MeV, and 0.4° at 100 MeV.

Bremsstrahlung is usually considered as a continuous process because a large number of events take place on a very short distance. However, in quantum electrodynamics (QED), Bremsstrahlung and electron-positron pair production appear to be two cross-symmetrical processes, as the Feynman diagram for the former is obtained by switching the incoming photon with the outcoming positron in the diagram for the latter. As a consequence, there is a cross section for Bremsstrahlung, and its expression is similar to the cross section for pair production. The differential cross section with respect to the photon energy(Kawrakow and Rogers, 2006) is given by:

$$\begin{aligned}\frac{\mathrm{d}\sigma_{\mathrm{Brem}}(E,Z)}{\mathrm{d}h\nu} &= \frac{A'(E,Z)r_{\mathrm{e}}^2\alpha Z(Z+\xi(Z))}{h\nu}\left[\left(1+\left(\frac{E-h\nu}{E}\right)^2\right)\left(\phi_1(\delta)-\frac{4}{3}\ln Z\right.\right.\\ &\left.\left.-4\tilde{f}_c(E,Z)\right)-\frac{2}{3}\frac{E-h\nu}{E}\left(\phi_2(\delta)-\frac{4}{3}\ln Z-4\tilde{f}_c(E,Z)\right)\right], \qquad (2.28)\end{aligned}$$

where

E is the energy of the electron,
Z is the atomic number of the nucleus,
$A'(E,Z)$ is an empirical correction factor,
r_{e} is the classical electron radius,
α is the fine structure constant,
$\tilde{f}_c(E,Z)$ is a Coulomb correction for $h\nu > 50$ MeV,
$\phi_i(\delta)$ are functions accounting for screening effects
$\xi(Z)$ is a correction factor accounting for the triple production process.

2.2.2 Møller scattering

Møller scattering(Møller, 1931) describes the hard collision of an electron on a free electron. When the kinetic energy transferred by an incoming electron to an atomic electron is much greater than the binding energy of that electron, the atomic electron is considered as free. The energy of the incoming electron needs to be greater than a threshold kinetic energy T_{c}. The differential cross section for Møller scattering with respect to the kinetic energy E'_{K} of the outcoming electron is given as follows:

$$\frac{\mathrm{d}\sigma^{-}_{\mathrm{inel}}}{\mathrm{d}E'_{\mathrm{K}}} = \frac{2\pi r_{\mathrm{e}}^2 m}{\beta^2 {E'_{\mathrm{K}}}^2}\left[1 + \frac{{E'_{\mathrm{K}}}^2}{(E_{\mathrm{K}} - E'_{\mathrm{K}})^2} + \frac{\tau^2}{(1+\tau)^2}\left(\frac{E'_{\mathrm{K}}}{E_{\mathrm{K}}}\right)^2 - \frac{1+2\tau}{(1+\tau)^2}\frac{E'_{\mathrm{K}}}{E_{\mathrm{K}} - E'_{\mathrm{K}}}\right], \qquad (2.29)$$

where E_{K} is the kinetic energy of the incident electron, β is its velocity, and $\tau = \frac{E_{\mathrm{K}}}{m}$.

The electrons being indistinguishable, the electron leaving with the higher energy is considered as the primary electron. Therefore, the maximum kinetic energy that can be transferred is $\frac{E_{\mathrm{K}}}{2}$. The total cross section is then given by:

$$\sigma^{-}_{\mathrm{inel}} = \int_{T_{\mathrm{c}}}^{\frac{E_{\mathrm{K}}}{2}} \frac{\mathrm{d}\sigma^{-}_{\mathrm{inel}}}{\mathrm{d}E'_{\mathrm{K}}}\mathrm{d}E'_{\mathrm{K}}\,. \qquad (2.30)$$

where T_{c} is the threshold energy for hard collision.

2.2.3 Bhabha scattering

Bhabha scattering(Bhabha, 1936) is the equivalent of Møller scattering when the incoming charged particle is a positron. However, in this case, the particles are distinguishable, and the electron can leave with all the energy. The differential cross section with respect to the kinetic energy of the outcoming electron is as follows:

$$\frac{\mathrm{d}\sigma^{+}_{\mathrm{inel}}}{\mathrm{d}E'_{\mathrm{K}}} = \frac{2\pi r_{\mathrm{e}}^2 m}{\beta^2 {E_{\mathrm{K}}}^2}\left[\frac{1}{\epsilon}\left(\frac{1}{\epsilon\beta^2} - B_1\right) + B_2 + \epsilon(\epsilon B_3 - B_4)\right], \qquad (2.31)$$

where

$$\epsilon = \tfrac{E'_{\mathrm{K}}}{E_{\mathrm{K}}}\,, \quad \tau = \tfrac{E_{\mathrm{K}}}{m}\,, \quad y = \tfrac{1}{2+\tau}\,, \quad \beta^2 = \tfrac{\tau(2+\tau)}{(1+\tau)^2}$$

$$B_1 = 2 - y^2\,, \quad B_2 = (1-2y)(3+y^2)\,, \quad B_3 = (1-2y)^3\,, \quad B_4 = B_3 + (1-2y)^2\,.$$

The electron is coming with a kinetic energy greater than the threshold kinetic energy T_{c}, but it can leave with all its energy. The limits of the integral in the expression of the total cross section are therefore different from those in the case of Møller scattering:

$$\sigma^{+}_{\mathrm{inel}} = \int_{T_{\mathrm{c}}}^{E_{\mathrm{K}}} \frac{\mathrm{d}\sigma^{+}_{\mathrm{inel}}}{\mathrm{d}E'_{\mathrm{K}}}\mathrm{d}E'_{\mathrm{K}}\,. \qquad (2.32)$$

2.2.4 Stopping powers and electron range

The rate of energy loss along the path of the charged particle is called *linear stopping power* S, and it is measured in MeV cm^{-1}. It is defined as:

$$S = -\frac{\mathrm{d}E}{\mathrm{d}x}. \tag{2.33}$$

However, we usually use the *mass stopping power* $\frac{S}{\rho}$, measured in MeV cm^2 g^{-1}.

We distinguish the *collisional stopping power* S_{coll} for the case when the electron undergoes a collision, and the *radiative stopping power* S_{rad} when the electron loses some of its kinetic energy to photons.

The general expression of the mass collisional stopping power in quantum elctrodynamics, with K-shell and polarisation correction is given as follows:

$$\frac{S_{\text{coll}}}{\rho}(E_{\text{K}}) = \frac{2\pi r_{\text{e}}^2 m_{\text{e}} c^2}{\beta^2} \frac{\mathcal{N}_{\text{A}} Z}{A} \left(2\ln\frac{E_{\text{K}}}{I} + \ln\left(1 + \frac{\tau}{2}\right) + F^{\pm}(\tau) - \delta \right) , \tag{2.34}$$

where

$\mathcal{N}_{\text{A}}$ is Avogadro's number,

I is the mean ionisation-excitation potential of the medium,

$F^{+}(\tau)$ is the function taking into account the contribution of Bhabha scattering in the case of positrons,

$F^{-}(\tau)$ is the function taking into account the contribution of Møller scattering in the case of electrons,

δ is the *polarisation density effect correction*, taking into account the fact that the charged particle polarises the medium and weakens the Coulomb field.

The *mass radiative stopping power* $\frac{S_{\text{rad}}}{\rho}$ is the rate of energy lost by electrons or positrons that results in the production of Bremsstrahlung or in annihilation. For electrons, the expression of the mass radiative stopping power is given by:

$$\frac{S_{\text{rad}}}{\rho} = \alpha r_{\text{e}}^2 Z^2 \frac{\mathcal{N}_{\text{A}}}{A} E B_{\text{rad}} , \tag{2.35}$$

where E is the total electron energy and B_{rad} is a function of E and Z, slowly varying from $\frac{16}{3}$ for nonrelativistic electrons to 15 for $E_{\text{K}} = 100$ MeV. The expression for positrons is different because it takes into account the possibility that the positron annihilates in flight. We can see in the expression of the radiative stopping power that it is approximately proportional to Z.

The sum of the collisional and the radiative stopping powers gives the total stopping power S_{tot}:

$$S_{\mathrm{tot}} = S_{\mathrm{coll}} + S_{\mathrm{rad}}\,. \tag{2.36}$$

Since light charged particles like electrons and positrons can be scattered at large angles at every interaction with the medium, their trajectories in the medium can be very tortuous. Therefore, their *range*, *i.e.*, the distance they reach before they stop, is shorter than the range they would have if they were continuously slowing down on a straight line. This latter range is obtained with the *continuous slowing down approximation* (CSDA) and its expression can be calculated as follows:

$$R_{\mathrm{CSDA}} = \int_0^{E_{\mathrm{K}}} \frac{1}{S_{\mathrm{tot}}(E)}\mathrm{d}E\,. \tag{2.37}$$

R_{CSDA} can be up to twice as long as the actual range of the electron, but it still gives a good approximation on its order of magnitude. For heavy charged particles, the physical range is very close to R_{CSDA}.

A last important concept that used especially in dosimetry is the concept of *mass restricted stopping power*. It is the linear rate of energy loss due to hard-collision events (excitation or ionisation) in which the energy transferred to secondary electrons is less than some cut-off energy Δ. It is usually noted L_Δ. For the validity of this definition, the cut-off energy need to be greater than the binding energy of the atomic electrons of the medium.

The expression of L_Δ is similar to that of S_{coll} (Equation 2.34), but the functions $F^+(\tau)$ and $F^-(\tau)$ are replaced by two other functions $G^+(\tau, \Delta)$ and $G^-(\tau, \Delta)$ that take the cut-off energy into account. In the Spencer-Attix theory (Subsection 3.2.2), Δ is chosen such that the range of electrons of energy $E = \Delta$ is no larger than the cavity size, *i.e.*, these are the electrons that deposit all their energy within the cavity.

Chapter 3

Dosimetry

3.1 Definitions

3.1.1 Kerma

Kerma is an acronym for "Kinetic Energy Released per unit MAss"[1] and was first introduced by (Roesch, 1958). It is the energy dE_{tr} transferred by indirectly ionising radiation to secondary charged particles, divided by the mass dm of medium where the energy is released.

$$K = \frac{dE_{\mathrm{tr}}}{dm} \tag{3.1}$$

The unit of kerma is the gray (1 Gy = 1 J kg^{-1}). The secondary charged particles release energy in the medium through atomic ionisations and excitations, but the kerma does not quantify this process. It only deals with the energy that is initially transferred to secondary charged particles. For this reason, it can be easily expressed in terms of the mass energy transfer coefficient $\frac{\mu_{\mathrm{tr}}}{\rho}$ for a monoenergetic photon beam:

$$K = \phi \cdot h\nu \cdot \frac{\mu_{\mathrm{tr}}}{\rho}\,, \tag{3.2}$$

where ϕ is the photon fluence.

---

[1] The term "energy per unit mass" is frowned upon in the use of the International System of Units (SI). The term "energy divided by mass" should be preferred.
`http://physics.nist.gov/cuu/Units/checklist.html` (last visited: 2007/08/17).

For a polyenergetic photon beam, the kerma is the sum of contributions for all energies in the spectrum:

$$\begin{aligned} K &= \int_0^{h\nu_{\max}} \phi(h\nu) \cdot h\nu \cdot \frac{\mu_{\mathrm{tr}}(h\nu)}{\rho} d(h\nu) && (3.3) \\ &= \int_0^{h\nu_{\max}} \phi(h\nu) \cdot h\nu \cdot d(h\nu) \times \frac{\int_0^{h\nu_{\max}} \phi(h\nu) \cdot h\nu \cdot \frac{\mu_{\mathrm{tr}}(h\nu)}{\rho} d(h\nu)}{\int_0^{h\nu_{\max}} \phi(h\nu) \cdot h\nu \cdot d(h\nu)} \\ &= \Psi \cdot \frac{\overline{\mu}_{\mathrm{tr}}}{\rho}, && (3.4) \end{aligned}$$

where Ψ is identified as the total energy fluence of the photon beam, the function $\phi(h\nu)$ is the energy spectrum of the photon beam, and $\frac{\overline{\mu}_{\mathrm{tr}}}{\rho}$ is the mass energy transfer coefficient averaged over the photon energy spectrum.

Using Equation 2.25, we can decompose the kerma into collisional and radiative components:

$$\begin{aligned} K &= \Psi \cdot \frac{\overline{\mu}_{\mathrm{en}}}{\rho} + \Psi \cdot \overline{g} \frac{\overline{\mu}_{\mathrm{tr}}}{\rho} \\ &= K_{\mathrm{coll}} + K_{\mathrm{rad}} \,. && (3.5) \end{aligned}$$

3.1.2 Absorbed dose

Absorbed dose is a concept that quantifies the biologically significant effects produced by any type of ionising radiation in any medium. It replaced exposure, which applied only to X and γ rays, to measure ionisation in air, and which could only be used for photon energies above 3 MeV (Khan, 1994).

The absorbed dose is defined by the International Commission on Radiation Units as the ratio $\frac{d\overline{\epsilon}}{dm}$, where $d\overline{\epsilon}$ is the mean energy imparted by ionising radiation to the small volume of medium of mass dm. Its unit is the gray (symbol: G). The energy imparted ϵ is the sum of all the energy entering a volume of medium minus all the energy that leaves the volume, including any mass-energy conversion within the volume. For example, a creation of mass will decrease the energy imparted.

3.1.3 Charged Particle Equilibrium (CPE)

When every charged particle of a given energy leaving a volume V of a medium is replaced by an identical particle with the same energy, there is *charged particle equilibrium* (CPE). Where there is CPE, the number of charged particles entering the volume and imparting their energy to the medium is equal to the number of charged particles with the same energy created by photons leaving the volume with the energy absorbed. In other words, where there is CPE, the collisional kerma and the absorbed dose are equal.

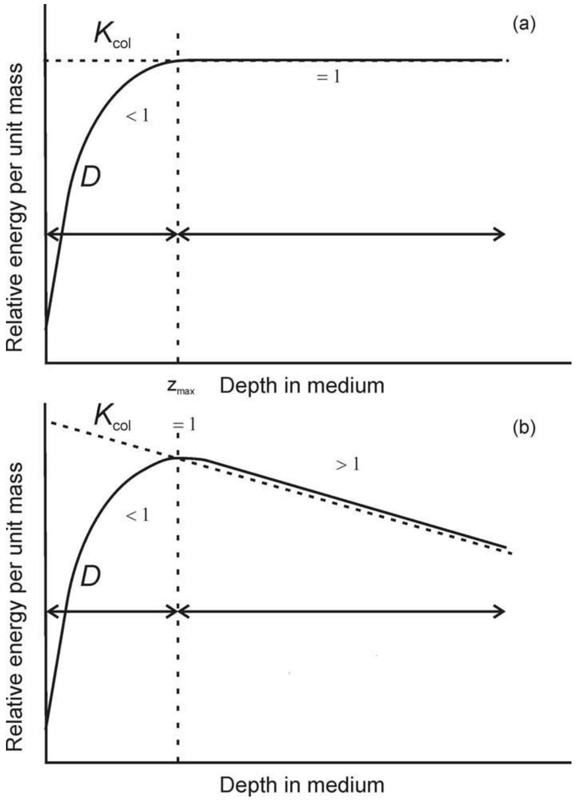

Figure 3.1: Illustration of collisional kerma and absorbed dose as a function of depth for a megavoltage photon beam. (a) shows the hypothetical case of no photon attenuation; (b) is the realistic case. From Podgoršak (2005a)

When a photon beam enters a medium, the collisional kerma is maximum at the surface and decreases with increasing depth because the photon beam is attenuated. If the mean energy of the photon beam is low enough, the range of the secondary charged particles—

mainly electrons—created in the medium is negligible, and they deposit their energy on the spot. In this case, the energy absorbed and the energy imparted in any small volume of mass dm are equal, *i.e.*, $K_{\text{coll}} = D$. This is a special case of CPE because in any volume V, no charged particle ever enters or leaves.

For high-energy photon beams, the range of secondary charged particles is not negligible anymore, and it increases with the photon energy. Therefore, the electrons created at the surface of the radiated medium deposit their energy downstream, very little energy is imparted at the surface, and the dose is minimum. The absorbed dose builds up with depth, as more and more electrons coming from upstream deposit their energy, and it reaches a maximum before it decreases because the photon fluence decreases (Figure 3.1).

The ratio $\beta = \frac{D}{K_{\text{coll}}}$ is smaller than one in the build-up region. There is a point where both curves of absorbed dose and collisional kerma intersect and where $\beta = 1$. At that point, CPE is reached. As we continue downstream, D is greater than K_{coll} ($\beta > 1$), but both curves decrease at the same rate. There is no CPE simply because the photons are attenuated and scattered. If we could correct for the attenuation and scattering (Figure 3.1a), there would be CPE at any depth beyond the dose maximum. In reality (Figure 3.1b), $\beta > 1$ but it is constant, and we say that there is *transient charged particle equilibrium* (TCPE).

3.2 Cavity Theory

3.2.1 Bragg-Gray Cavity Theory

Unaware of the work published by Bragg (1912), Gray (1929) developed a theoretical relation between the absorbed dose in a medium and the absorbed dose in a small air-filled cavity inside that medium, and he called it *principle of equivalence.* There are two conditions for the validity of the Bragg-Gray cavity theory (Podgoršak, 2005a):

- The size of the cavity must be small compared to the range of the charged particles crossing, so that the cavity does not perturb their fluence in the medium.
- Photon interactions inside the cavity are ignored, therefore the absorbed dose is en-

tirely deposited by the charged particles crossing the cavity.

Under these two conditions, the relation between the dose in the medium and the dose in the cavity is then:

$$D_{\text{med}} = D_{\text{cav}} \left(\frac{\overline{S}}{\rho}\right)_{\text{cav}}^{\text{med}} , \tag{3.6}$$

where $\left(\frac{\overline{S}}{\rho}\right)_{\text{cav}}^{\text{med}}$ is the ratio of the average unrestricted mass collision stopping power of the medium to that of the cavity.

The qualification as a Bragg-Gray cavity depends on the size of the cavity compared to the range of the electrons in the medium. It depends consequently on the energy of the photon beam. A Bragg-Gray cavity for a megavoltage photon beam may be too large and not behave as a Bragg-Gray cavity for a kilovoltage photon beam.

3.2.2 Spencer-Attix

The Bragg-Gray cavity theory does not take into account the fast δ electrons that are created by hard collisions and that are travelling through the cavity. Spencer and Attix (1955) developed a more general theory that accounts for these electrons. Their theory uses the same conditions as Bragg and Gray's, but it incorporates the electrons created inside the cavity. Some of these electrons may be energetic enough to leave the cavity and reduce the absorbed dose.

The secondary electrons[2] created in the cavity are divided into two groups based on a threshold energy Δ defined by Spencer. The secondary electrons with kinetic energies E_{K} less than Δ are categorised as slow electrons depositing all their energy locally and do not contribute to the absorbed dose. The electrons with kinetic energies greater than Δ are considered as fast electrons, *i.e.*, leaving the cavity, and they are included in the electron energy spectrum. The threshold energy Δ is related to the size of the cavity and is the energy of the electron whose range is equal to the mean chord length of the cavity.

The Spencer-Attix relation between the dose to the medium and the dose in the cavity is similar to Bragg and Gray's, but restricted mass stopping powers with threshold Δ must

---

[2] The electrons generated by electron impacts are secondary electrons. The primary electrons are those generated by the photon beam.

be used:

$$
\begin{aligned}
D_{\mathrm{med}} &= D_{\mathrm{cav}} \left(\frac{\overline{L}_{\Delta}^{\mathrm{SA}}}{\rho} \right)^{\mathrm{med}}_{\mathrm{cav}} && (3.7) \\
&= \frac{\int_{\Delta}^{E_{\mathrm{K0}}} \phi^{\mathrm{med},\delta}(E_{\mathrm{K}}) \left(\frac{L_{\Delta}(E_{\mathrm{K}})}{\rho} \right)^{\mathrm{med}} dE_{\mathrm{K}} + \phi^{\mathrm{med},\delta}(\Delta) \left(\frac{S(\Delta)}{\rho} \right)^{\mathrm{med}} \Delta}{\int_{\Delta}^{E_{\mathrm{K0}}} \phi^{\mathrm{med},\delta}(E_{\mathrm{K}}) \left(\frac{L_{\Delta}(E_{\mathrm{K}})}{\rho} \right)^{\mathrm{cav}} dE_{\mathrm{K}} + \phi^{\mathrm{med},\delta}(\Delta) \left(\frac{S(\Delta)}{\rho} \right)^{\mathrm{cav}} \Delta} , && (3.8)
\end{aligned}
$$

where $\phi^{\mathrm{med},\delta}(E_{\mathrm{K}})$ is the electron fluence from the medium including the fast secondary electrons created in the cavity. The second terms in the second equation account for a part of the energy deposited by the electrons in the spectrum with energies between Δ and 2Δ. These electrons may lose enough energy to be left with a kinetic energy below Δ, in which case they will be removed from the spectrum.

Since both Bragg-Gray and Spencer-Attix theories make the hypothesis that CPE is reached, the ratio $\phi^{\mathrm{med}}_{\mathrm{cav}}$ is assumed to be equal to one. In reality, even in reference conditions, there are effects that can perturb the fluence; therefore, the ratio $\phi^{\mathrm{med}}_{\mathrm{cav}}$ can no longer be taken as equal to one.

3.3 Ionisation chamber dosimetry

Ionisation chamber dosimetry is one of many ways to measure dose, either absolutely or relatively. Other techniques are typically film dosimetry, chemical dosimetry, calorimetry, semiconductor dosimetry, *etc.*

Figure 3.2 shows a basic design of a cylindrical Farmer-type ion chamber, similar to that used in this thesis. It is composed of a cylindrical outer electrode and a central electrode separated by an insulator. A high polarising voltage is applied to both electrodes. The ions created by radiation in the air cavity between both electrodes are collected and the total charge is read by an electrometer and linearly converted into dose to the air cavity. It can be written generally as:

$$D_{\mathrm{det}} = N_{\mathrm{det}} \cdot M_{\mathrm{det}} \, , \tag{3.9}$$

where M_{det} is the signal collected by the detector (the electric charge in a ionisation chamber), and N_{det} is the detector calibration coefficient previously measured by absolute

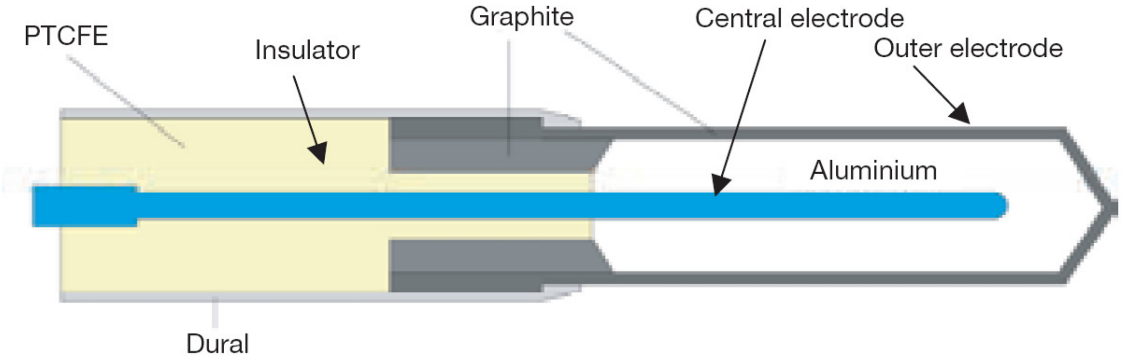

Figure 3.2: Basic design of a cylindrical Farmer-type ionisation chamber. From Podgoršak (2005a)

dosimetry.

For ionisation chambers with an air cavity, the dose is given by:

$$D_{\text{air}} = \frac{Q_{\text{ion}} \cdot \frac{\overline{W}_{\text{air}}}{e}}{m_{\text{air}}}\,, \tag{3.10}$$

where Q_{ion} is the absolute value of the total charge of the ions of one sign created in the air cavity, $\frac{\overline{W}_{\text{air}}}{e}$ is the mean energy expended in air to create a charge of 1 C (its value is 33.97 J C^{-1} in dry air), and m_{air} is the mass of air in the cavity.

Combining Equations 3.9 and 3.10, it is straightforward to obtain the expression of the air cavity calibration coefficient of the chamber:

$$N_{D,\text{air}} = \frac{1}{m_{\text{air}}} \cdot \frac{\overline{W}_{\text{air}}}{e}\,. \tag{3.11}$$

We can see that $N_{D,\text{air}}$ only depends on the detector characteristics; therefore, it is the same for any beam quality, if, as it is assumed, $\frac{\overline{W}_{\text{air}}}{e}$ does not vary with energy. Since $\frac{\overline{W}_{\text{air}}}{e}$ is known, we only need to know the mass of air in the cavity to calculate the air cavity calibration coefficient. However, the geometry of the chamber is never exactly known. Moreover, the volume of air where the ions are created is generally smaller than the total volume of air in the cavity, and there may be edge effects near the cavity region where the air is not polarised. It is, therefore, impossible to know exactly the mass of air that enters in the expression of $N_{D,\text{air}}$. For this reason, the calibration coefficient is measured under reference beams in a primary standard laboratory.

Finally, from the dose to the air cavity, we can get the dose to the medium by using Spencer-Attix theory:

$$D_{\text{med}} = Q_{\text{ion}} \cdot \frac{1}{m_{\text{air}}} \cdot \frac{\overline{W}_{\text{air}}}{e} \cdot \left(\frac{\overline{L}}{\rho}\right)^{\text{med}}_{\text{air}} . \tag{3.12}$$

This last equation represents the formalism of dose measurements with an ionisation chamber. It is an ideal equation. In practice, a series of correction factors need to be applied in order to correct the signal for atmospheric and electrical perturbations, and to correct for fluence perturbations.

3.4 Calibration protocols

Calibration protocols are guidance documents on clinical reference dosimetry in external beam radiotherapy for high-energy photon beams, between ^{60}Co and 50 MV, and high-energy electron beams, between 4 MeV and 50 MeV. The protocols describe how to use ionisation chambers for reference dose measurements, using the calibration coefficient associated to the chamber and measured in a primary standard laboratory.

3.4.1 Air-kerma-based - TG-21/TRS-277

The air-kerma-based protocols AAPM TG-21 (Schultz *et al.*, 1983) and IAEA TRS-277 (Andreo *et al.*, 1987) describe how to perform reference dosimetry when the calibration coefficient from the primary standard laboratory is a ^{60}Co exposure calibration coefficient N_{X}^{Co}, or an air-kerma calibration coefficient N_{K}^{Co}. Both are related as follows:

$$N_{\text{K}}^{\text{Co}} = N_{\text{X}}^{\text{Co}} \cdot \frac{\overline{W}_{\text{air}}}{e} \cdot \frac{1}{1-\overline{g}} , \tag{3.13}$$

where $\overline{g}$ is the radiative fraction (Equation 2.25).

The dose to water in a photon beam of quality Q is then given by:

$$\begin{aligned} D_{\text{w}} &= M_Q \cdot N_{D,\text{air}} \cdot \left(\frac{\overline{L}}{\rho}\right)^{\text{w}}_{\text{air}} \cdot p_Q \\ &= M_Q \cdot N_{\text{K}}^{\text{Co}} \cdot (1-\overline{g}) \cdot k_{\text{m}} \cdot k_{\text{att}} \cdot k_{\text{cel}} \cdot s_{\text{w,air}} \cdot p_Q , \end{aligned} \tag{3.14}$$

where

$s_{\text{w,air}}$ is the TRS-277 notation for $\left(\frac{\overline{L}}{\rho}\right)^{\text{w}}_{\text{air}}$, the unrestricted mass stopping power ratio.

M_Q is the chamber signal corrected for atmospheric effects,

k_m is a correction factor for the non–air equivalence of the chamber wall and build-up cap needed for an air-kerma in air measurement,

k_att is a correction factor for photon attenuation and scatter in the chamber wall,

k_cel is a correction factor for the non–air equivalence of the central electrode of the cylindrical ionisation chamber,

p_Q is the product of $p_\mathrm{wall}p_\mathrm{dis}p_\mathrm{cav}p_\mathrm{cel}$, the perturbation correction factors accounting for perturbations caused by the chamber inserted in water.

These air-kerma-based protocols were much more accurate than previous methods, but they were more complex. They required the user to calculate theoretical dosimetry factors, and large tables of stopping power ratios and mass energy absorption coefficients. They are now abandoned, and absorbed-dose-to-water based protocols are used.

3.4.2 Absorbed-dose-to-water-based - TG-51/TRS-398

Absorbed-dose-to-water-based protocols AAPM TG-51 (Almond *et al.*, 1999) and IAEA TRS-398 (Andreo *et al.*, 2004) describe how to perform reference dosimetry when the calibration coefficient is the chamber-specific ^{60}Co absorbed-dose-to-water calibration coefficient $N_{D,\mathrm{w}}^{\mathrm{Co}}$, measured in cGy nC^{-1}, and traceable to a primary standard laboratory.

In reference conditions, *i.e.*, at 10 cm depth, at 100 cm SSD or SAD, and in a 10×10 cm^2 field, the dose to water in a photon beam of quality Q is given as:

$$\begin{aligned} D_\mathrm{w} &= (M \cdot P_\mathrm{ion}P_\mathrm{TP}p_\mathrm{elec}P_\mathrm{pol}) \cdot \frac{1}{m_\mathrm{air}} \cdot \frac{\overline{W}_\mathrm{air}}{e} \cdot s_{\mathrm{w,air}} \cdot p_\mathrm{wall}p_\mathrm{dis}p_\mathrm{cav}p_\mathrm{cel} \\ &= M^\mathrm{c} \cdot N_{D,\mathrm{w}}^{Q}\,, \end{aligned} \tag{3.15}$$

where P_ion, P_TP, P_elec and P_pol are charge measurement correction factors, and p_wall, p_dis, p_cav and p_cel are perturbation correction factors.

The calibration coefficient is specific to the beam quality. To obtain the calibration coefficient $N_{D,\mathrm{w}}^{Q}$ for the beam quality Q from that for ^{60}Co, we use a *conversion factor* k_Q:

$$N_{D,\mathrm{w}}^{Q} = k_Q \cdot N_{D,\mathrm{w}}^{\mathrm{Co}}\,. \tag{3.16}$$

The value of the conversion factor depends on the type of cylindrical chamber and on the value of the photon component of the photon beam percentage depth-dose at 10 cm depth in water, in a 10×10 cm^2 field, at 100 cm SSD. However, its expresion is easy to identify from the previous equations:

$$k_Q = \frac{\left[\frac{\overline{W}_{\text{air}}}{e} s_{\text{w,air}} \cdot p_{\text{wall}} p_{\text{dis}} p_{\text{cav}} p_{\text{cel}}\right]_Q}{\left[\frac{\overline{W}_{\text{air}}}{e} s_{\text{w,air}} \cdot p_{\text{wall}} p_{\text{dis}} p_{\text{cav}} p_{\text{cel}}\right]_{^{60}\text{Co}}} . \tag{3.17}$$

Finally, once the dose to water at 10 cm in reference conditions has been measured for the beam quality Q, it can be converted to the dose to water at any other depth, at any SSD, for any field size, with a use of the appropriate parameters.

Huq and Andreo (2004) provide a comparison between air-kerma-based and dose-to-water-based protocols. They emphasise that both protocols lead to the same uncertainties when used with the same criteria. However, they advocate the use of dose-to-water standards because (i) the calibration at primary standard laboratories is easier to perform, (ii) dose-to-water procedures are based on specific calibrations for each chamber, (iii) air-kerma-based protocols rely on the value of W_{air}, which may vary with energy.

3.4.3 Correction factors

We just saw that there are two types of correction factors. Some of them correct the charge measurement for atmospheric effects and chamber imperfection. The others correct for the perturbation of the charged particle fluence because we are not in the idealistic situation of the Spencer-Attix theory.

The charge measurement correction factors are:

- P_{ion}, the correction factor for the recombination of ions in the air cavity before they arrive to the collecting electrodes. For a pulsed beam, such as in linear accelerators, its value is $P_{\text{ion}} = \frac{1 - V_{\text{H}}/V_{\text{L}}}{M^{\text{H}}_{\text{raw}}/M^{\text{L}}_{\text{raw}} - V_{\text{H}}/V_{\text{L}}}$.

- P_{TP}, the temperature and pressure correction. When the chamber is not sealed, the mass of air in the cavity varies with both the temperature and pressure, and we have to correct for it. Using the ideal gas law $PV = nRT$, we can get the value $P_{\text{TP}} = \frac{P_0}{P}\frac{T}{T_0}$.

- P_{elec}, the correction factor to be used when the chamber is used with another electrometer than that with which it was calibrated.

- P_{pol}, the correction factor for the polarity effect. It is necessary because the inversion of the polarity can alter the charge measurement. The effect is due to two phenomena (i) the *Compton current* created in the electrode when photons interact with it, thus increasing or decreasing the collected charge and (ii) *extracameral* current, *e.g.*, current collected outside the sensitive volume of the chamber.

The perturbation correction factors are:

- p_{wall}, the correction factor for the fact that the chamber wall is not water despite the fact that we use the stopping power ratio $s_{\text{w,air}}$.
- p_{cel}, a similar correction factor for the fluence-perturbing presence of the central electrode (Palm and Mattsson, 1999).
- p_{dis}, the correction for the gradient effect on the electron fluence due to the presence of the chamber. It can be replaced by a shift upstream by 60 % of the chamber inner radius (radius of the cavity).
- p_{cav}, the correction for the presence of the chamber in water.

Chapter 4

Materials and methods

4.1 Formalism

Bouchard and Seuntjens (2004) and Capote *et al.* (2004) independently proposed to introduce a correction factor C^{IMRT} to correct $N_{D,\mathrm{w}}$ for IMRT conditions. It is defined as follows:

$$N_{D,\mathrm{w}}^{\mathrm{IMRT},Q} = C^{\mathrm{IMRT},Q} \cdot N_{D,\mathrm{w}}^{Q} \tag{4.1}$$

or

$$C^{\mathrm{IMRT},Q} \hat{=} \frac{[D_{\mathrm{a}}^{\mathrm{w}}]^{\mathrm{IMRT},Q}}{[D_{\mathrm{a}}^{\mathrm{w}}]^{Q}} \,, \tag{4.2}$$

where $[D_{\mathrm{a}}^{\mathrm{w}}]^{Q}$ is the ratio of the dose to water to the dose to the air cavity in reference conditions for the beam quality Q, and $[D_{\mathrm{a}}^{\mathrm{w}}]^{\mathrm{IMRT},Q}$ is the ratio of the dose to water to the dose to the air cavity in IMRT conditions for the beam quality Q. Capote *et al.* measured C^{IMRT} directly, from phase space files obtained with Monte-Carlo simulation. Taking a pencil beam approach (Gustafsson *et al.*, 1994), Bouchard and Seuntjens (2004) developed the following expressions:

$$[D_{\mathrm{a}}^{\mathrm{w}}]^{Q} = \frac{\int_{-5}^{5}\int_{-5}^{5} d_{\mathrm{w}}(x,y,z) f(x,y) dxdy}{\int_{-5}^{5}\int_{-5}^{5} d_{\mathrm{a}}(x,y,z) f(x,y) dxdy} = s_{\mathrm{w,air}} p_{\mathrm{wall}} p_{\mathrm{dis}} p_{\mathrm{cav}} p_{\mathrm{cel}} \tag{4.3}$$

and

$$[D_{\mathrm{a}}^{\mathrm{w}}]^{\mathrm{IMRT},Q} = \frac{\int_{-\infty}^{\infty}\int_{-\infty}^{\infty} d_{\mathrm{w}}(x,y,z) T^{\mathrm{IMRT}}(x,y) f(x,y) dxdy}{\int_{-\infty}^{\infty}\int_{-\infty}^{\infty} d_{\mathrm{a}}(x,y,z) T^{\mathrm{IMRT}}(x,y) f(x,y) dxdy} = [s_{\mathrm{w,air}} p_{\mathrm{wall}} p_{\mathrm{dis}} p_{\mathrm{cav}} p_{\mathrm{cel}}]^{\mathrm{IMRT}} \,, \tag{4.4}$$

where

$d_{\mathrm{w}}(x, y, z)$ is the dose-to-water kernel, *i.e.*, the dose response in a water voxel placed on-axis at a depth of z cm when a pencil photon beam hits the point (x, y) at 100 cm,

$d_{\mathrm{a}}(x, y, z)$ is the dose-to-air kernel, *i.e.*, the dose-to-air-cavity response when the ionisation chamber is at a depth of z cm when a pencil photon beam hits the point (x, y) at 100 cm,

$T^{\mathrm{IMRT}}(x, y)$ is the transmission function representing the transmission of the photon beam through the MLC at the point (x, y),

$f(x, y)$ is the relative photon fluence in the isocentre plane.

The transmission function depends on the thickness of the MLC leaf that the incident primary photon beam traverses at (x, y). For a step-and-shoot treatment mode, it can be written as follows:

$$T(x, y) = \sum_{i=1}^{N} \omega_i e^{-\overline{\mu} l_i(x,y)}\,, \tag{4.5}$$

where ω_i is the weight of the field i, $\overline{\mu}$ is the average attenuation coefficient of primary photons through the MLC, and $l_i(x, y)$ is the thickness of MLC leaf traversed by the primary photon beam incident at (x,y) in the isocentre plane, for the field i. In the case of a dynamic delivery, the average transmission function is given by:

$$T(x, y) = \frac{1}{\tau} \int_0^{\tau} e^{-\overline{\mu} l(x,y,t)} dt\,, \tag{4.6}$$

where τ is the total dMLC treatment time, and l(x,y,t) is time-dependent.

4.2 The EGSnrc Monte-Carlo code system

The EGS (*Electron Gamma Shower*) Monte-Carlo code system was first developed at the Stanford Linear Accelerator Center (SLAC), CA, in the mid 1970s for high energy physics (Bielajew *et al.*, 1994). A new version called EGSnrc was released in 2000 by the National Research Council of Canada (NRC-CNRC), ON, where it is now essentially developed and maintained (Kawrakow, 2000a,b).

EGSnrc is a general purpose package for Monte-Carlo simulation of the transport of photons, electrons and positrons with energies ranging from a few keV to hundreds of GeV (Kawrakow and Rogers, 2006). It offers a large number of new features over EGS, the previous version released in 1985. Many physical situations are calculated more accurately, and among all the ameliorations in the physics of the code, we can mention the following:

- A new electron algorithm. Depending on the geometry, much larger steps can be taken with a better accuracy. The boundary crossing is optionally performed in single scattering mode to ensure its accuracy.
- Atomic relaxation is available, which allows the creation and following of fluorescent photons from shells K, L and M, as well as Auger and Coster-Kronig electrons.
- Bound Compton scattering is available as well as Klein-Nishina Compton scattering.

Other features are now built into the package, such as the variance reduction techniques. Finally, the NRC user codes DOSRZnrc, FLURZrnc, CAVRZnrc and SPRZrnc are now distributed with the package (Rogers *et al.*, 2004). The new user code CAVITY, which we used for this work, was added in 2005 with the new EGSnrc C++ class library (Kawrakow, 2005).

4.2.1 The physics of EGSnrc

The strength and accuracy of EGSnrc consist in its highly accurate simulation of the physical processes pertaining to photon end electron transport. The radiation transport can be simulated in any element, compound or mixture. Particles are transported in steps of random length according to the mean free path in the medium, rather than in discrete steps.

Most of the physical processes discussed in Chapter 2 are included in, and simulated by, EGSnrc. For photons, they are: Rayleigh scattering, photoelectric effect with atomic relaxation including Auger and Coster-Kronig electrons, Klein-Nishina and bound Compton scattering including the radiative Compton effect (Brown and Feynman, 1952), pair and triple production. For electrons, they include positron annihilation in flight and at rest, multiple electron scattering including relativistic spin effects, Bremsstrahlung from Bethe-Heitler cross sections or from the NIST Bremsstrahlung cross section database, Møller and Bhabha scattering and collisional stopping powers.

A *history*, or case, or shower, is the complete track of a particle with its energy, position and region index, direction cosines, charge *etc.*, along with all its descendants and so forth, until their energy drops below the user-defined cut-off value or they leave the geometry of interest. The initial particle of a history is created according to the distribution describing the source. The distance it travels is calculated from a random number generator that follows a probability distribution depending on the total interaction cross section. The particle is then scattered into another energy, direction cosines, *etc.*, according to the differential cross section of the interaction, possibly producing new particles that will be transported as well. The quantities of interest are scored during the simulation of the particle history, and they are averaged over a given number of histories.

Electrons present a difficulty because in the slowing-down process, they undergo hundreds of thousands of interactions with the medium; an event-by-event simulation of electron transport would produce a large number of secondary particles to be transported, and it would require an unreasonable simulation time. To circumvent this difficulty, the electron transport in EGSnrc is based on the *condensed history* technique (Berger, 1963). This method condenses a large number of consecutive transport and collision processes to a single step. Appropriate multiple scattering distributions at the end of the step are used to take into account the cumulative effect of the successive elastic and inelastic collisions during the step. This approach is valid when the electron energy is high enough so that a single collision barely changes the state of the electron. The condensed history technique fails when this condition is not satisfied, at very low energies.

The real trajectory of the electron along a step is not a straight line, and an *electron-step algorithm* is used to take the deflections into account. The electrons are assumed to lose energy continuously between two "catastrophic" collisions, and the angular deflections in between are calculated. The mean free path to the next collision is calculated from the total cross section for Møller and Bremssttrahlung interactions.

This electron-step algorithm is only valid in an infinite, homogeneous medium. In practical situations, an electron may come close to an interface with another material, its curved path may be in this different material, and so the trajectory may be different from the simulated trajectory. This leads to artefacts and possible dose over-predictions (Kawrakow, 2000b). The presence of interfaces is treated by an exact *boundary crossing algorithm* (BCA). As it approaches an interface, the electron is not allowed to take steps longer than the distance to the closest boundary. However, when the electron comes closer to the boundary than the user-defined minimum step length for boundary crossing, the simulation goes over to a single elastic scattering mode. This minimum distance, called *skin depth for BCA* has a default value of three elastic mean free paths because it is the distance below which single scattering simulation is more efficient than condensed history simulation (Kawrakow and Rogers, 2006).

4.2.2 EGSnrc algorithm

The EGS code consists of two subroutines, `HATCH` and `SHOWER`, that are called by the MAIN program. `HATCH` handles the once-only initialisation and reads the material data previously created by the program PEGS4. Once the initialisation is completed, MAIN may call `SHOWER`, which initiates the cascade. Each call to `SHOWER` generates one history. The general structure of EGSnrc is shown in Figure 4.1.

Three other subroutines usually called are written by the user; `HOWFAR` and `HOWNEAR` determine the geometry, and `AUSGAB` handles the scoring, the output and the variance reduction. The `SHOWER` subroutine calls to `ELECTR` and `PHOTON` for electron and photon transport, respectively. In turn, they call `HOWFAR` and `HOWNEAR` that respectively evaluate the distance to the next boundary in the direction of the particle and the nearest distance to a boundary. `ELECTR` and `PHOTON` call the physics subroutines. In `AUSGAB`, the user defines which quantity they want to be scored, such as energy absorbed, particle fluence, *etc.* For this purpose, the user can communicate with EGS the values of variables from the `common` blocks.

Some important variables of the `common` blocks are:

- ECUT and PCUT, the cut-off energies for charged particles and photons, respectively, for each region. Below these energy cut-offs, the particle histories are terminated.

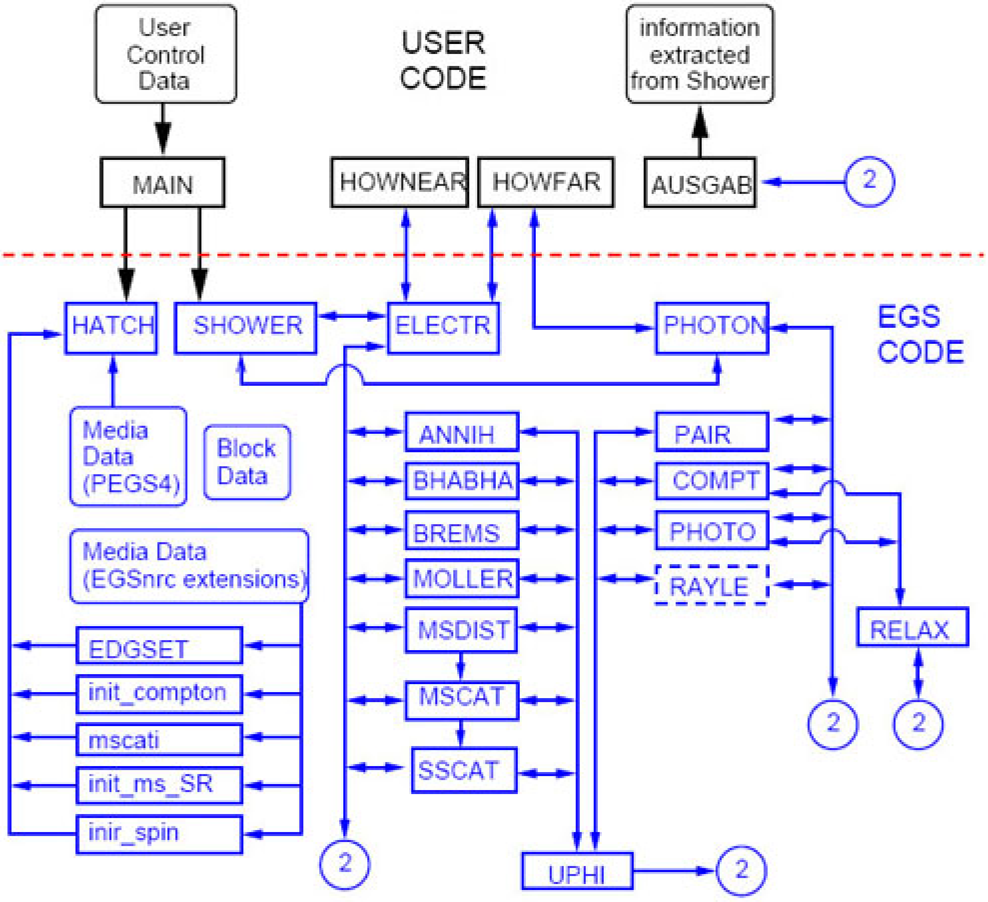

Figure 4.1: Flowchart of the EGSnrc code system when used with a user-code. From Kawrakow and Rogers (2006)

- IRAYLR is set to 1 or 0 for each region to decide whether Rayleigh scattering will be done in the region.
- SPIN_EFFECTS is a logical variable set to `.true.` if relativistic spin effects are to be included in electron transport.
- SKINDEPTH_FOR_BCA is a real variable that specifies the distance in number of elastic mean free paths at which electron transport should switch to the BCA.
- ESTEPE is a real variable, setting the global maximum fractional energy loss in an electron step due to continuous energy loss.

4.2.3 Variance reduction techniques

The efficiency of a Monte-Carlo simulation code can be increased by reducing the variance for a given simulation time, the simulation time for a given variance, or both. Techniques that increase the efficiency are called *variance reduction techniques* although they may reduce the simulation time instead of the variance itself (Kawrakow and Fippel, 2000). There are three variance reduction techniques available in EGSnrc, each of which the user should activate in the subroutine `AUSGAB`.

Electron range rejection is a technique that checks the electron range against the distance to the nearest boundary on every step. If the range is shorter than the distance to the boundary, the electron history is terminated. This technique involves an approximation because the electron could emit a photon that could leave the region. To control it, the user has to set an energy threshold `e_max_rr`, under which range rejection can be applied.

Another technique is *Russian roulette*. The option is turned on by setting the integer flag `i_play_rr` to 1 and the probability `prob_RR` to an appropriate value. When Russian roulette is played on a photon, it will survive with the probability `prob_RR` and its weight will be multiplied by $\texttt{prob\_RR}^{-1}$.

Russian roulette is usually played in conjunction with *Bremsstrahlung splitting*, the last of the four variance reduction techniques offered by EGSnrc. When an electron emits a photon, the simulation emits a number `nbr_split` of photons with their weight equal to $\texttt{nbr\_split}^{-1}$. They all acquire the energy lost by the electron, so that energy conservation seems to be lost for the history. However, energy is conserved on average. When Russian roulette is also used, the appropriate value of `prob_RR` is $\texttt{nbr\_split}^{-1}$.

There are other variance reduction techniques, *e.g.*, *photon interaction forcing*, that the user can implement in `AUSGAB`. Unlike those we just dealt with, some variance reduction techniques actually reduce the variance, such as techniques that increase the importance of particles with a large influence on the dose.

4.3 Kernel sampling with CAVITY

We used the CAVITY/EGSnrc Monte-Carlo code to calculate the dose kernels[1] in water and the air cavity of the chamber. CAVITY[2] is a similar code to DOSXYZnrc or DOSRZnrc, but it can use any geometry that can be modelled within the EGSpp geometry package[3]. It also allows the user to get dose responses for any number of sources and scoring region positions in the same run.

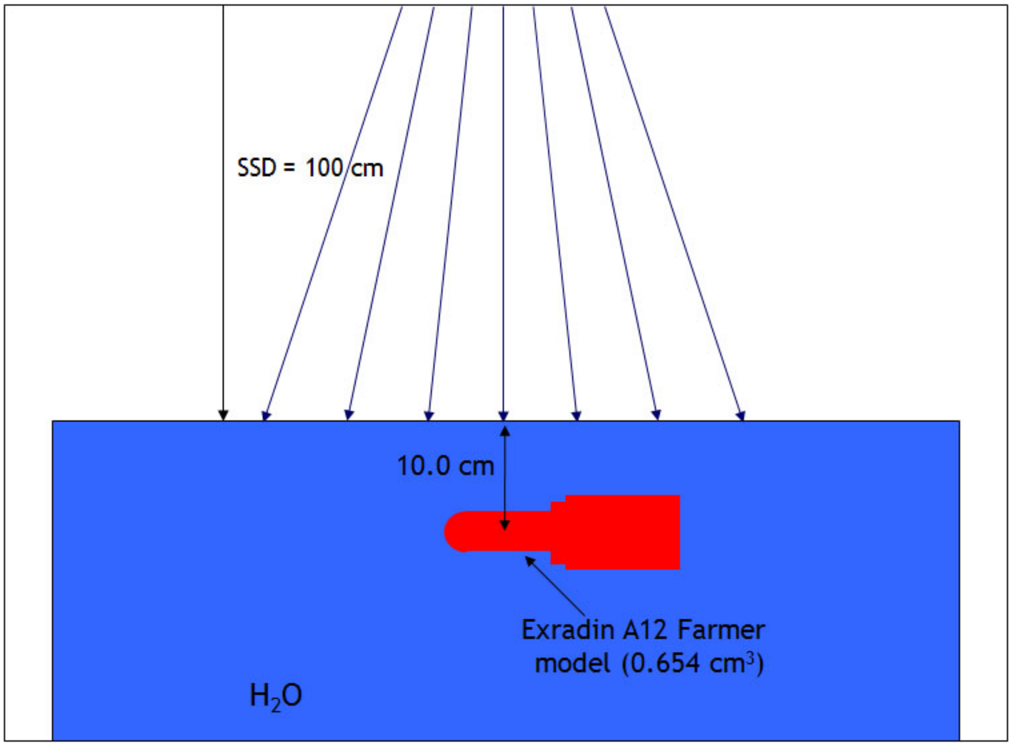

Figure 4.2: This diagram illustrates how the dose-to-air kernel is acquired. The chamber model is placed at 10 cm in a water phantom, and a pencil beam is swept at the surface of the phantom.

The dose kernels in water and air were acquired for different set-ups. The tests of the chamber model were made with dose kernels acquired using a SSD of 100 cm and a

---

[1] These are summation kernels, not inverse kernels used in convolution methods (see Ahnesjö and Aspradakis, 1999).

[2] `http://www.irs.inms.nrc.ca/EGSnrc/pirs898/cavity.html` (last visited: 2007/08/25).

[3] `http://www.irs.inms.nrc.ca/EGSnrc/pirs898/index.html` (last visited: 2007/08/25).

reference depth of 10 cm. However, the kernels used in IMRT conditions were acquired in Solid Water®, with a SAD of 100 cm and a reference depth of 8.5 cm to reproduce the conditions in which IMRT QA is performed at the Montreal General Hospital. A 1 mm^3 water voxel and the chamber model were embedded in a rectangular parallelepipedic water phantom whose dimensions were $30 \times 30 \times 17$ cm^3, and the dose was recorded in the water voxel or the chamber air cavity centred on the beam axis at the reference depth. The chamber axis was positioned perpendicularly to the main beam axis. The kernels were acquired by sweeping a pencil photon beam on the surface of the water phantom (Figure 4.2).

Chapter 5

Results and Discussion

5.1 Test of the CAVITY user code

CAVITY/EGSnrc was released not long ago before we started using it. Although is uses the same algorithms as the other EGSnrc user codes, CAVITY is written in C++ instead of Mortran, and it is used in a slightly different way. In other words, we needed to learn how to use it and be sure we understood the results it was giving us.

We decided to compare CAVITY with the well-tested code CAVRZnrc. We first learnt that CAVITY and CAVRZnrc do not handle the fluence in the same manner. This is what led us to the understanding of why and how dose per history in kernels had to be converted to dose per fluence (Equation 5.1).

	CAVITY	CAVRZnrc	ratio
dose/Gy	$5.2764 \times 10^{-9}(1 \pm 0.127\ \%)$	$5.2817 \times 10^{-9}(1 \pm 0.13\ \%)$	1.001 ± 0.002

Table 5.1: Comparison of CAVITY and CAVRZ in a simple set-up

Table 5.1 shows a comparison of CAVITY and CAVRZnrc in a simple set-up. A ^{60}Co source at an SSD of 100 cm, collimated in a disc with a radius of 1.3 cm, was shot on a pancake air cavity with graphite walls. The air cavity dimensions were 1 cm OD × 0.2 cm, and the wall thickness was 0.3 cm. The results show an agreement within 0.1 % between both user codes; therefore, we concluded we could use CAVITY with confidence.

5.2 The chamber model

Using the EGSpp geometry package of EGSnrc, a detailed model of the Exradin A12 Farmer chamber was constructed (Figure 5.1). The dimensions and components of the chamber follow the prescriptions of the blueprint, which was confidentially given to us by the manufacturer. The wires, the central electrode, the inside joints, and especially the cavity volume were carefully designed as per the blueprint.

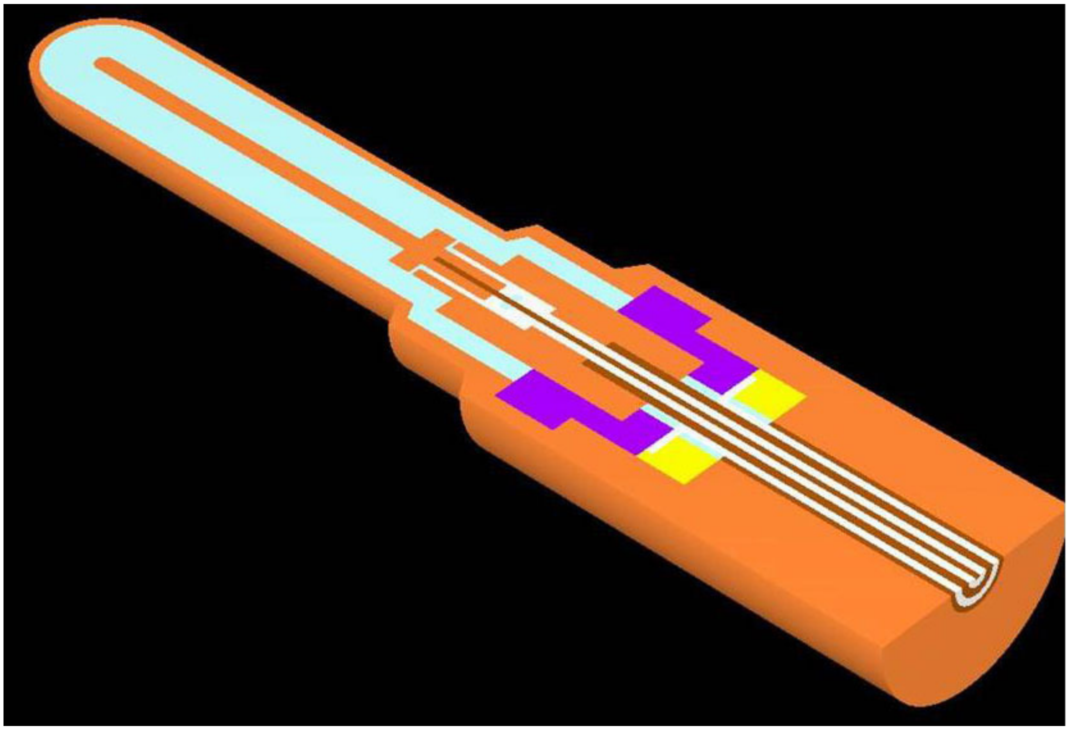

Figure 5.1: Model of the Exradin A12 Farmer chamber designed with the EGS++ geometry package of EGSnrc.

This detailed model is used for testing purposes only. We showed that a simpler model will give the same results for the air cavity dose response, and the simulation will take six times as less time to run. The simpler model used hereafter does not show any detail in the stem. The wires and joints are replaced by the same plastic as in the wall and central electrode, and the conical parts in the geometry are replaced by only cylinders. The simplifications are far enough from the sensitive volume of the chamber to have any significant effect on the simulations.

The sensitive volume does not include the entire volume of the air cavity. In Figure 5.1, the plastic part in the central section of the chamber, just behind the central electrode, is at the same potential as the chamber wall. Therefore, the air between this central plastic piece and the wall is not polarised, and no charge is ever collected from it. The only sensitive region is the air between the central electrode and the wall, and the small volume of air between the central electrode and the central plastic piece. This definition still holds with the simpler model that we used, of course, since the central piece and the wall form only one plastic piece. The boundary effects between the sensitive air volume and the non sensitive one were neglected.

The chamber model is 4.115 cm long and the external radius of the chamber thimble is 0.355 cm. The wall around the air cavity is 0.05 cm thick. The central electrode has a hemispherical tip, and its thinnest part is 2.05 cm long. The centroid of the chamber is defined on the axis of the chamber, at 1.29 cm from its tip. The calculated volume of the sensitive air cavity is 0.654 263 cm^3. It is a necessary piece of information that CAVITY cannot compute itself because of the generality of the geometry package.

The chamber model was tested in reference conditions, with photon beams of energies 1.25 MeV, 6 MV and 18 MV. The set-up was a photon source collimated on a $10 \times 10\ \mathrm{cm}^2$ field, at 100 cm from the surface of a water phantom. For dose-to-air measurements, the chamber model was embedded at 10 cm in the phantom, whereas for dose-to-water measurements, a 125 mm^3 water voxel was embedded in the phantom. The test consisted of simulating the quality conversion factor k_Q for 6 MV and 18 MV, and of comparing the results with those in the report TG-51 (Almond *et al.*, 1999). PDD curves were simulated for both energies, and the values of $N_{D,\mathrm{w}}$ were calculated for the three energies.

The values of k_Q obtained with the chamber model (Table 5.2) agree with the values from the TG-51 within one standard deviation. It shows that the Monte-Carlo simulations with the model of the Exradin A12 ionisation chamber correctly reproduce the measurements made in reference conditions.

	Dose/(10^{-16} Gy cm^2)			k_Q	
	water	air	$N_{D,\mathrm{w}}$	Monte-Carlo	TG-51
^{60}Co	2.954 ± 0.009	2.632 ± 0.004	1.123 ± 0.004		
6 MV	4.872 ± 0.005	4.352 ± 0.013	1.119 ± 0.004	0.996 ± 0.005	0.995
18 MV	0.905 ± 0.010	9.105 ± 0.009	1.088 ± 0.002	0.969 ± 0.004	0.973

Table 5.2: Test results of the chamber model in reference conditions

5.3 Kernel sampling

5.3.1 Sampling

The dose kernels were acquired with the user code CAVITY. ECUT and PCUT were set to 0.521 MeV and 0.01 MeV, respectively. We used the EGSnrc electron-step algorithm and the exact boundary crossing algorithm. Rayleigh scattering, triplet production and the radiative Compton effect were off. For the variance reduction, both photon splitting and Russian roulette were used. The photon splitting was set at 50, the rejection range was set at 1 MeV, and the Russian roulette survival probability was 0.01. For the dose-to-air kernels, 500 000 histories were simulated per point, whereas 4×10^7 histories were simulated per point for the dose-to-water kernels.

The kernels were acquired by sweeping a pencil photon beam on the surface of the water phantom (Figure 4.2). The first kernels we acquired were one-dimensional profiles of the chamber model and the water voxel embedded in water. For these profiles, we used a very small parallel beam ($r = 1$ nm) instead of a pencil beam. The results were given in Gy cm^2.

Figure 5.2 shows the transverse profile of the chamber model acquired across its centroid. The dose to the air cavity in the chamber increases as the beam approaches the chamber. There is a change in slope at $x = -0.355$ and $x = 0.355$ when the beam hits the chamber wall instead of only water. The dose peaks correspond to the maximum distance the beam travels through the wall. Moving towards the centre, the beam crosses a decreasing thickness of wall and the dose to the air cavity decreases. At the centre, the effect of the central electrode on the dose is clearly visible.

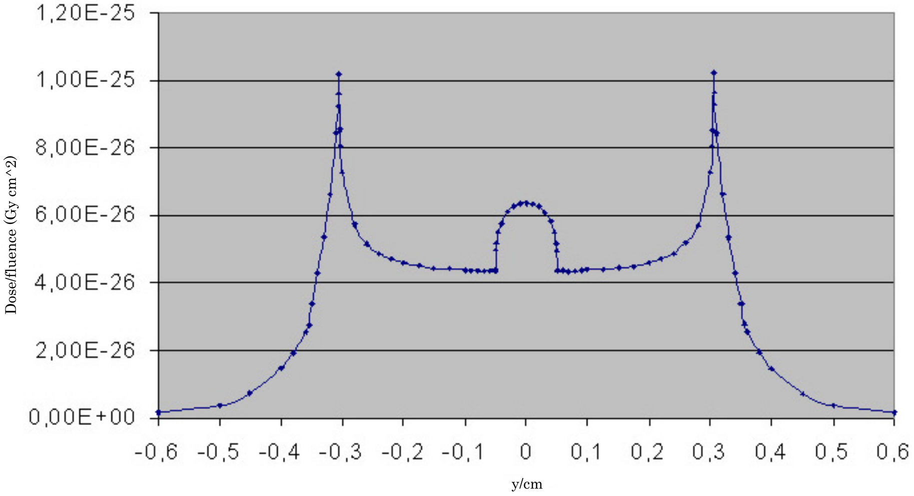

Figure 5.2: Transverse profile of the chamber model obtained at 3 cm in water with a parallel beam ($r = 1$ nm).

Two longitudinal chamber profiles are shown in Figure 5.3. One was acquired on-axis, and the other was off-axis, still in the cavity, so that the beam does not travel through the central electrode. The goal was to show the effect of the central electrode in the difference of both graphs. On the figure, we can see the effects of details in the chamber between $x = -1.5$ cm and $x = -1$ cm. These effects are due to the changing outside diameter of the chamber and to the varying thickness of air the beam travels through in the inactive cavity region. The point at $x = 0$ is the position of the chamber centroid. When the beam is directly impinging on the air cavity, the dose is maximum if the beam hits the centroid. Finally, the dose maxima at the tip of the chamber are not at the same position. This is explained by the fact that the chamber tip is hemispherical. Therefore, the off-axis beam reaches the tip wall for a smaller x than the beam on axis.

Generalising the method used to compute chamber profiles, we generated the two-dimentional kernels. The method was also refined and the kernels were acquired with dimensionless pencil beams. The pencil beam having no cross section, the dose per fluence scored by CAVITY, which is usually reported in Gy cm^2, was reported here in Gy/history. The influence of this seemingly insignificant fact will be discussed in the next subsection. A

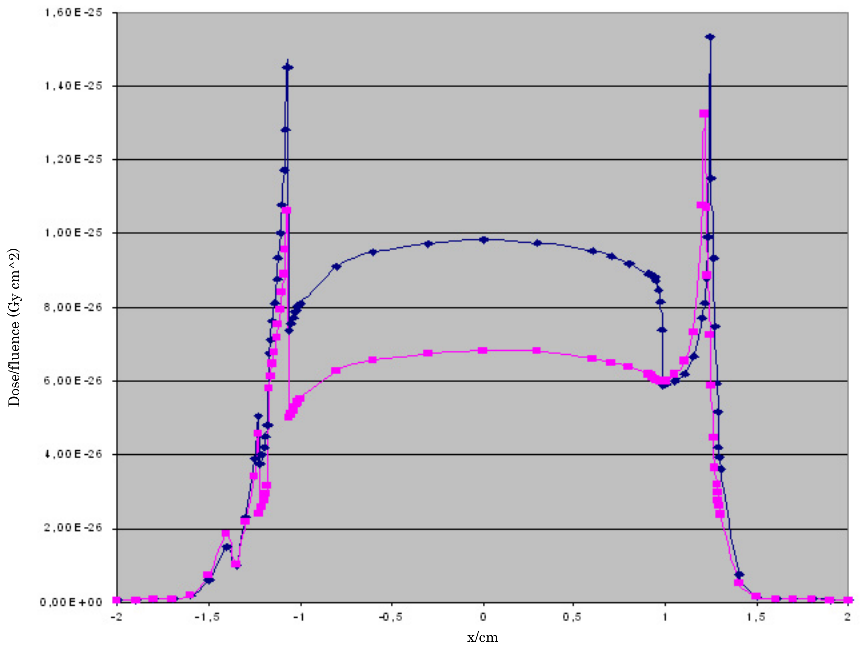

Figure 5.3: Longitudinal profile of the chamber model obtained at 10 cm in water with a parallel beam ($r = 1$ nm). The blue profile was acquired on-axis. The purple profile was acquired off-axis at 0.14 cm to avoid the central electrode.

total of 1702 beam positions were simulated for half of the chamber because of its symmetry. For the water voxel that has three axes of symmetry, 190 beam positions were simulated for one eighth of the voxel. The beam positions were defined at the intersections of an irregular rectangle grid, as illustrated in Figure 5.4. A high density of points was measured in regions with much geometric detail or where the dose gradient was high. For the chamber, it was in the tip, near the wall and at the back of the sensitive volume (Figure 5.4a). For the water voxel, the density of points was decreasing from the centre to the field edge (Figure 5.4b).

5.3.2 Interpolation

The kernels were not exploitable immediately after the Monte-Carlo simulation. The number of points calculated was not sufficient. Moreover, the results given as dose per history were not convertible to results as dose per fluence. To be able to do that, we needed to know the dose per history at a point within a small cell, so that we could consider that

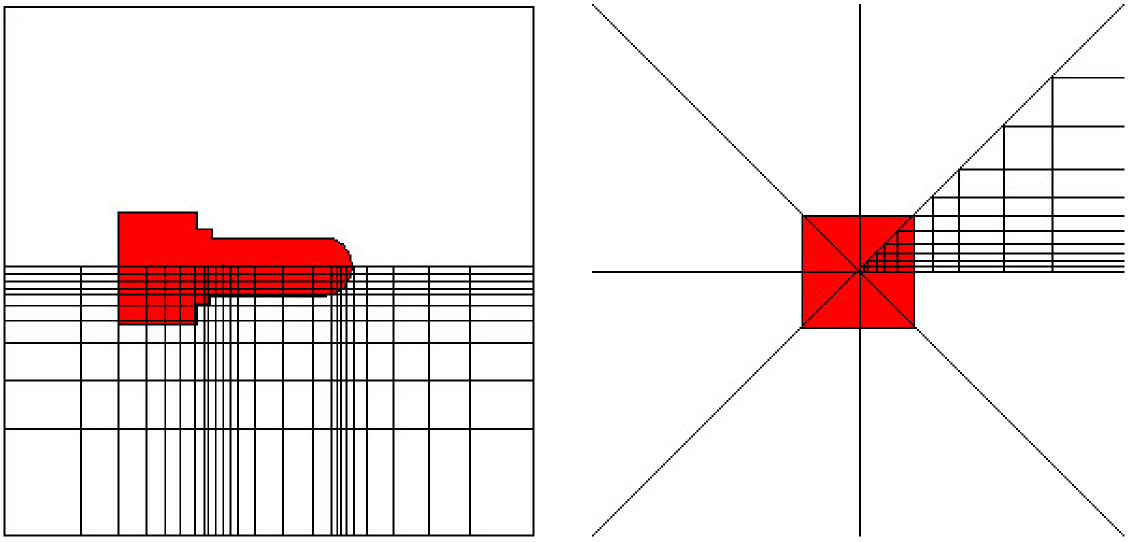
(a) Dose-to-air kernel sampling grid

(b) Dose-to-water kernel sampling grid

Figure 5.4: Irregular grids used for kernel sampling. The symmetries of the chamber model and of the water voxel allow to reduce the number of points where dose responses are scored.

all the points within the cell were at the same position and at the same distance from the source. When one converts a dose per history to a dose per fluence, one needs to correct for the inverse square law and the angle between the beam direction and the normal to the cell, before multiplying by the cell area.

The first step was then to define a fine and regular grid. We developed a code in which the kernel was interpolated to obtain 1001 × 1001 points in a 10×10 cm^2 field. The size of a cell was therefore 0.01 mm^2. Since the kernels were mostly concave, they were not bilinearly interpolated because the interpolation would have overestimated the dose. Instead, a bilinear interpolation was performed on the logarithms of the dose values to lower the interpolated values. However, the dose uncertainties were bilinearly interpolated as a conservative measure.

Once the kernel had been interpolated, the dose per history responses were converted to dose per fluence responses:

$$\begin{aligned} D\ [\mathrm{Gy\ cm^2}] &= (\text{cell area}) \times (\text{angle correction}) \times (\text{inverse square law}) \times D\ [\mathrm{Gy/history}] \\ &= (10^{-4}\ \mathrm{cm}^2) \times \left(\frac{\mathrm{SAD}^2}{\mathrm{SAD}^2 + x^2 + y^2}\right)^{\frac{3}{2}} \times D\ [\mathrm{Gy/history}] \qquad (5.1) \end{aligned}$$

The kernels were stored as tables with the position at (x, y) in the isocentre plan, the dose per fluence, and the standard deviation. They were ready to be exploited by the main code algorithm.

5.4 Code algorithm

The code algorithm was developed by Bouchard (2003) (see also Bouchard and Seuntjens (2004)). Without repeating in length Bouchard's explanations, it is useful to present the main features of the code (Figure 5.5).

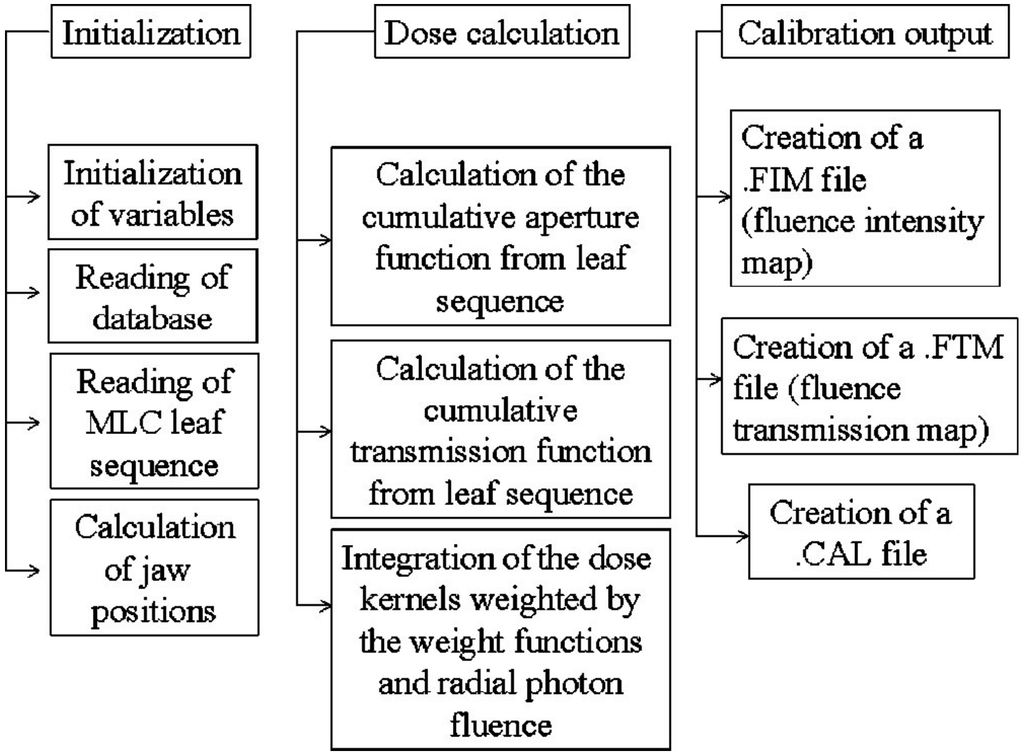

Figure 5.5: Schematic diagram of the components of the software developed to calculate C^{IMRT} for any MLC sequence. Image from Bouchard and Seuntjens (2004).

The code initialises the variables and functions, then it reads the dose kernel tables and the MLC sequence. The program calculates the cumulative aperture function from the leaf sequence, the transmission function, and it computes the integrations of the dose kernels weighted by the radial fluence and the transmission function. The integrations are performed for both reference conditions and the MLC sequence. The transmission function (Equation 4.6) takes into account most of the geometrical properties of the Varian® Millenium 120 MLC including the rounded leaf ends, the divergence and the tongue-and-groove details. The jaw positions are calculated to follow the way they are set during a Varian IMRT delivery. The X jaws are positioned 0.8 cm outside from the edge of the maximum leaf opening in the x direction. The Y jaws are set at 0.2 cm outside from the edge of the maximum leaf opening in the y direction.

The code yields the dose to water and the dose to air for the reference conditions and for the MLC sequence. From these four quantities, we can calculate the relative dose factor (RDF), the relative cavity dose (RCD) and C^{IMRT}. In our analysis, we only needed RCD, but the extra information was often useful for cross checking. Finally, the program creates a fluence intensity map, a fluence transmission map and an output file.

The code has a feature allowing to calculate a dose uncertainty due to the positioning of the chamber. The dose is calculated for the main chamber position and for the eight chamber positions obtained by shifting the chamber by 1 mm in any direction in the (x, y) plane. The uncertainty due to the positioning was claimed by Bouchard and Seuntjens (2004) to be more than three orders of magnitude higher than the statistical uncertainties from the kernel.

All the dose components of the kernels were assumed by the authors to be statistically independent, yielding an extremely small uncertainty when summing the kernel. However, as it is shown in appendix A, the kernel components cannot be assumed as statistically independent after the interpolation process. Covariance terms appear in the kernel summation variance, and the uncertainty is actually much higher. In fact, with the kernels we acquired, the statistical uncertainty is of the same order of magnitude as the uncertainty due to the chamber positioning.

5.5 Kernel summation in reference conditions

The interpolated kernels were first tested in reference conditions. It was a way to validate the kernel summation approach, as well as the interpolation method. Dose-to-water and dose-to-air kernels were summed for ^{60}Co and 6 MV photon beams, and the calculations of $N_{D,\mathrm{w}}$ and k_Q were compared to those acquired in the direct calculation shown in Table 5.2.

	$N_{D,\mathrm{w}}$		
	^{60}Co	6 MV	k_Q
Direct MC calculation	1.123 ± 0.006	1.118 ± 0.005	0.996 ± 0.005
Kernel summation	1.125 ± 0.008	1.120 ± 0.004	0.995 ± 0.008

Table 5.3: Test results of kernel summation in reference conditions.

The results of the comparison are shown in Table 5.3. Both calculation methods are in good agreement, within 1 %. It showed the validity of the summation method, and it allowed us to use the kernels in comparison with chamber measurements.

5.6 Kernel summation and measurements with static open fields

The comparison between Monte-Carlo calculations and measurements for ten static open fields and one dynamic wedge is shown in Table 5.4. The measurements were performed on a Varian® 6EX, with an Exradin® A12 Farmer chamber at 10 cm in a water phantom. For each measurement, 100 MU were delivered at a rate of 400 MU/min.

Figure 5.6 shows beam's eye views of the open fields that we used in our measurements. The chamber is shown for every field to understand better where the fields edges were with respect to the active region of the air cavity. For example, we may expect that the positioning will be very critical for the fields in Figures 5.6d and 5.6e. On the contrary, the positioning should have no importance in Figure 5.6h.

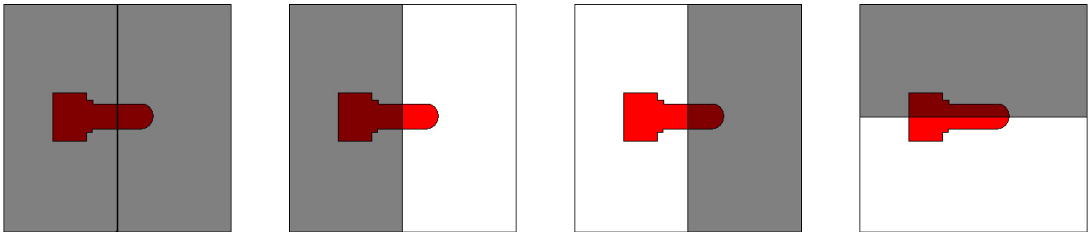

(a) Closed field (b) 5 × 10 right field (c) 5 × 10 left field (d) 10 × 5 down field

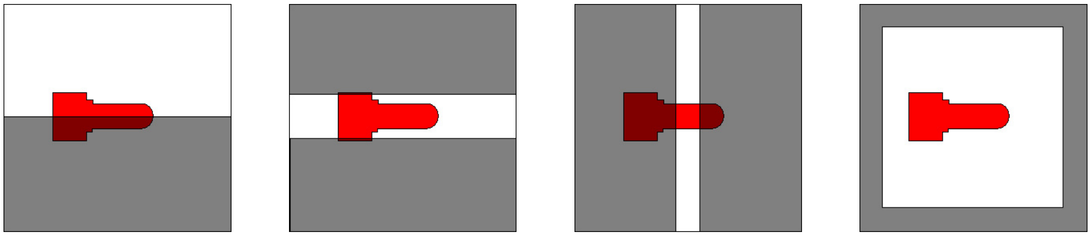

(e) 10 × 5 up field (f) 10 × 1 field (g) 1 × 10 field (h) 8 × 8 field

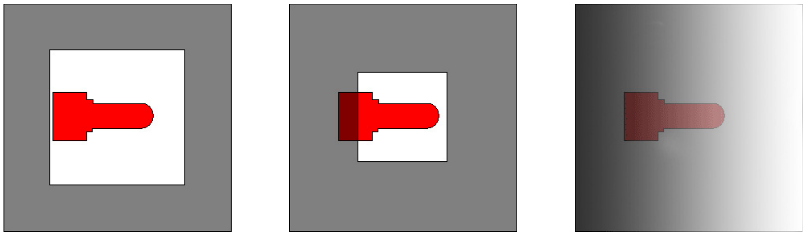

(i) 6 × 6 field (j) 4 × 4 field (k) Dynamic wedge

Figure 5.6: Beam's eye views of the fields used in open fields measurements

Figures 5.7 to 5.17 show the fluence intensity maps and the fluence transmission maps for the open fields measured. Whereas the intensity maps show very sharp field edges, the transmission maps show the effects of leakage, of interleaf transmission and of the rounded leaf ends.

The Table 5.4 shows values of Relative Chamber Dose (RCD), the ratio of the dose to the chamber cavity for the field considered to the dose to the chamber cavity in reference conditions. The uncertainties reported for the experimental data are type A uncertainties. They are very small compared to the uncertainties reported for the Monte-Carlo data. The latter combine the statistical uncertainties from EGSnrc that are calculated after interpolation following the results in Appendix A and the uncertainties due to the positioning of the chamber.

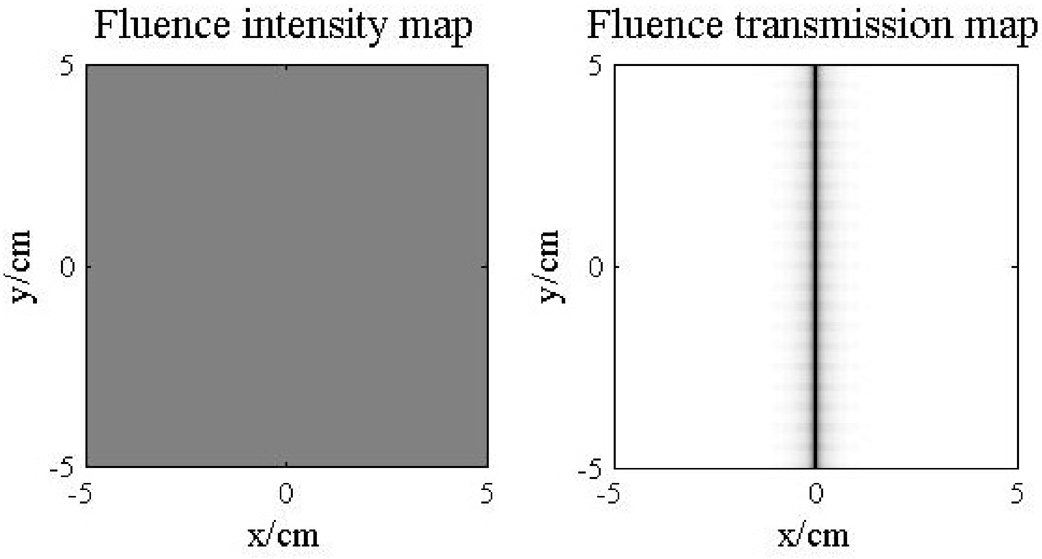

Figure 5.7: Fluence intensity map and fluence transmission map of the closed field used in open field measurements

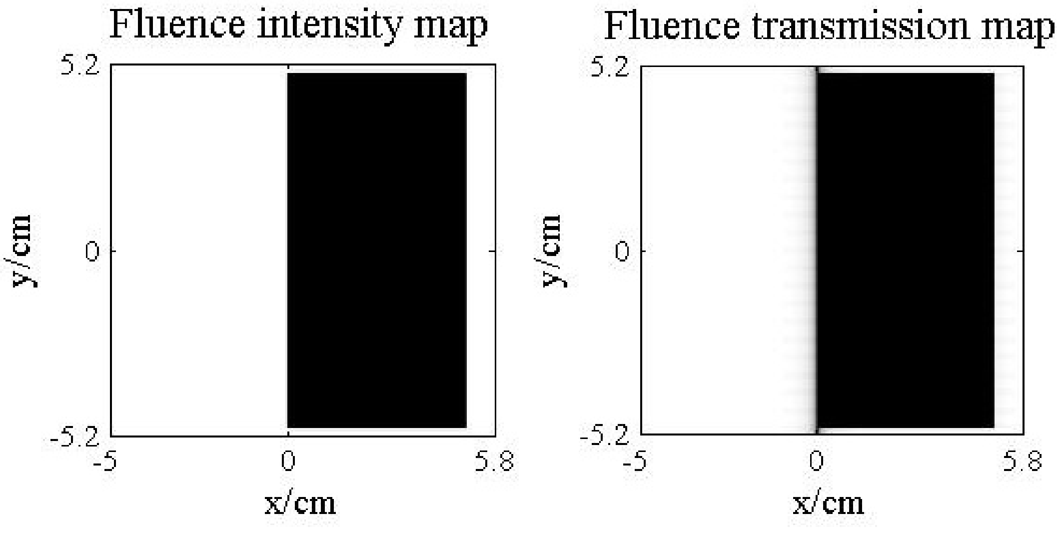

Figure 5.8: Fluence intensity map and fluence transmission map of the 5 × 10 right field used in open field measurements

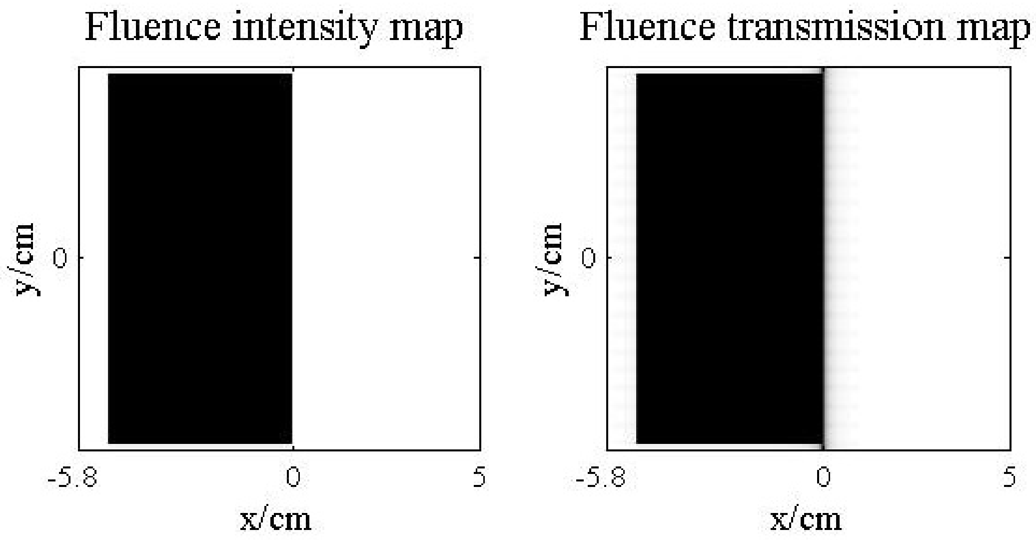

Figure 5.9: Fluence intensity map and fluence transmission map of the 5 × 10 right field used in open field measurements

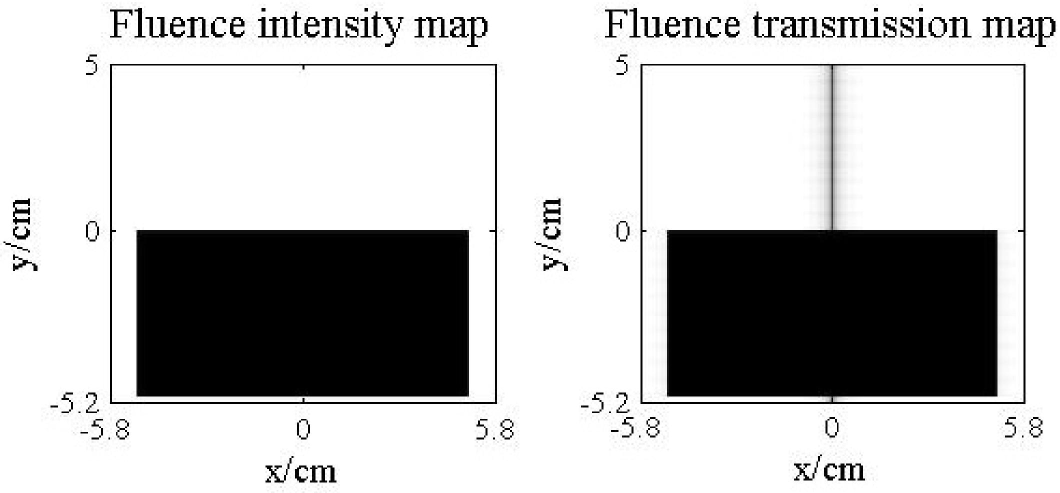

Figure 5.10: Fluence intensity map and fluence transmission map of the 10 × 5 down field used in open field measurements

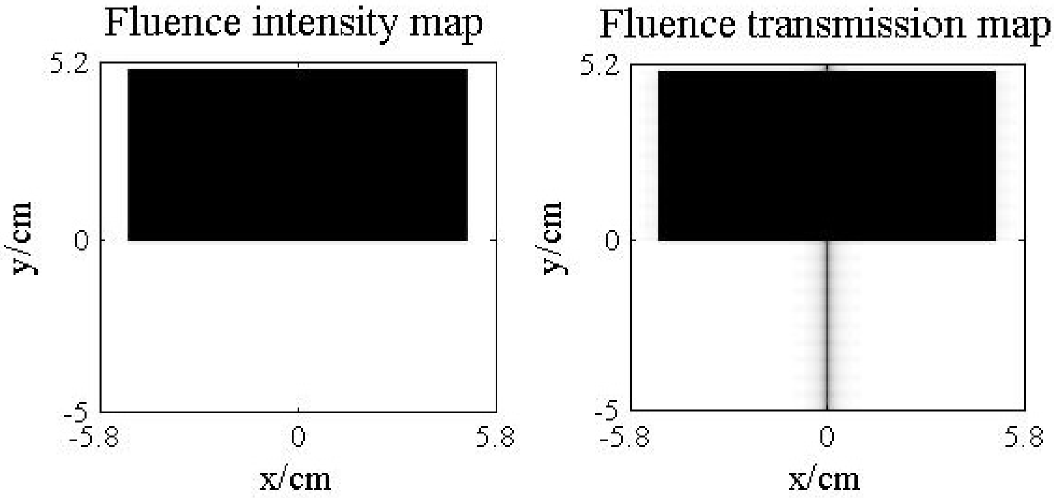

Figure 5.11: Fluence intensity map and fluence transmission map of the 10×5 up field used in open field measurements

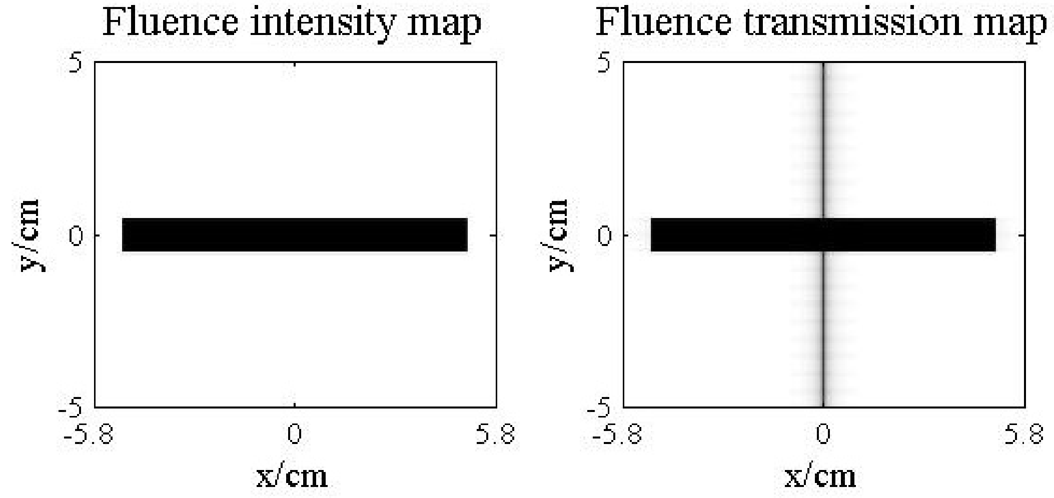

Figure 5.12: Fluence intensity map and fluence transmission map of the 10×1 field used in open field measurements

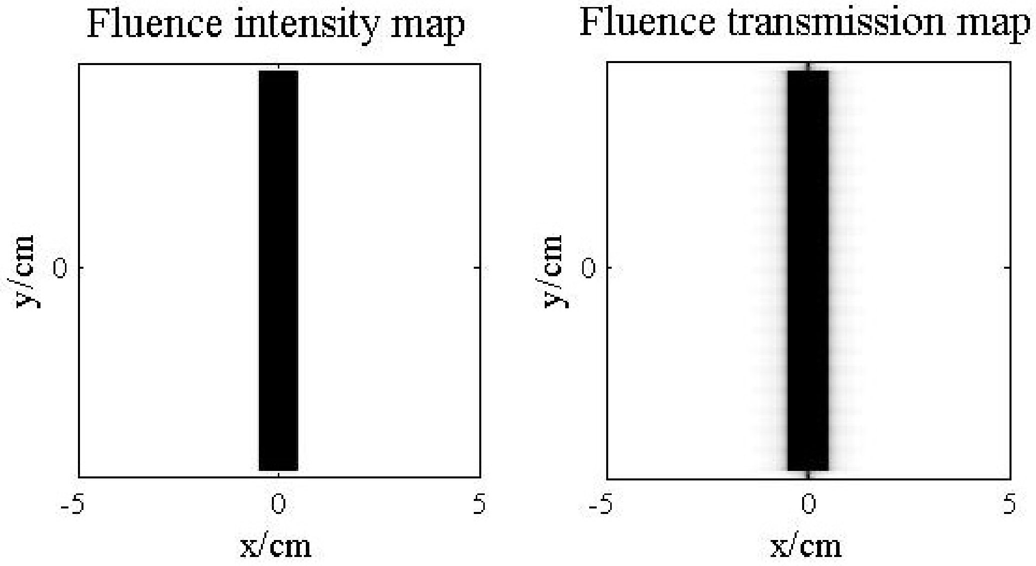

Figure 5.13: Fluence intensity map and fluence transmission map of the 1 × 10 field used in open field measurements

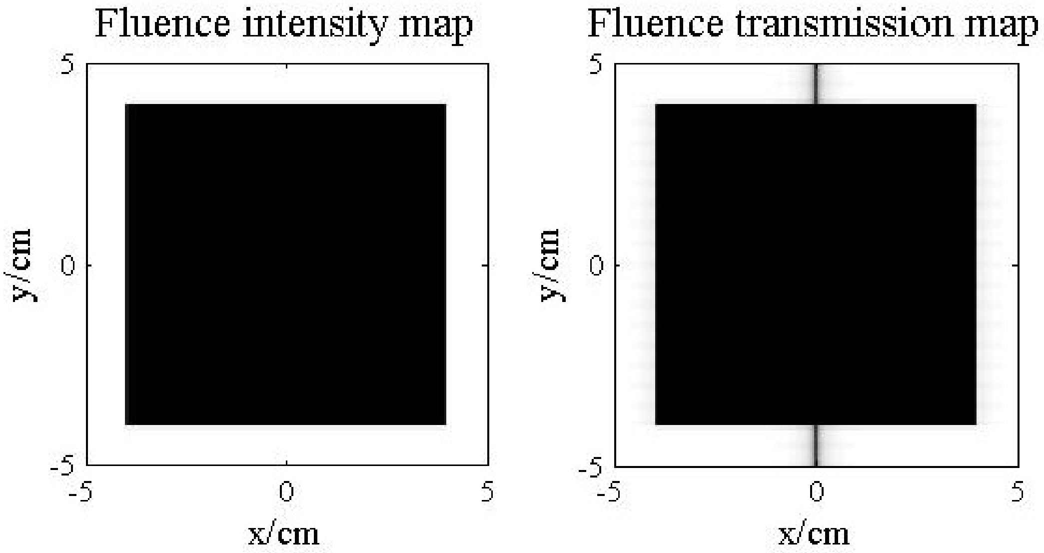

Figure 5.14: Fluence intensity map and fluence transmission map of the 8 × 8 field used in open field measurements

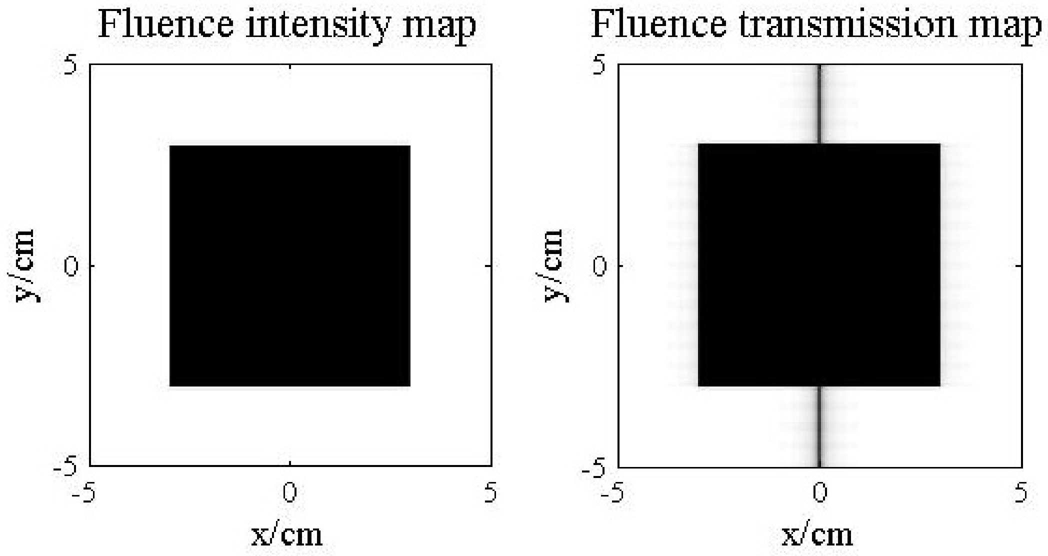

Figure 5.15: Fluence intensity map and fluence transmission map of the 6 × 6 field used in open field measurements

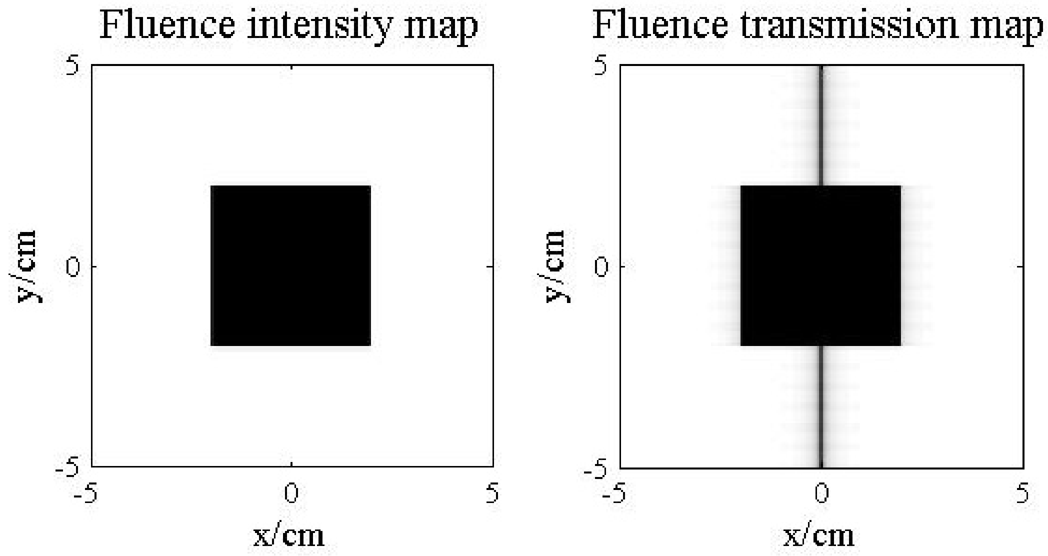

Figure 5.16: Fluence intensity map and fluence transmission map of the 4 × 4 field used in open field measurements

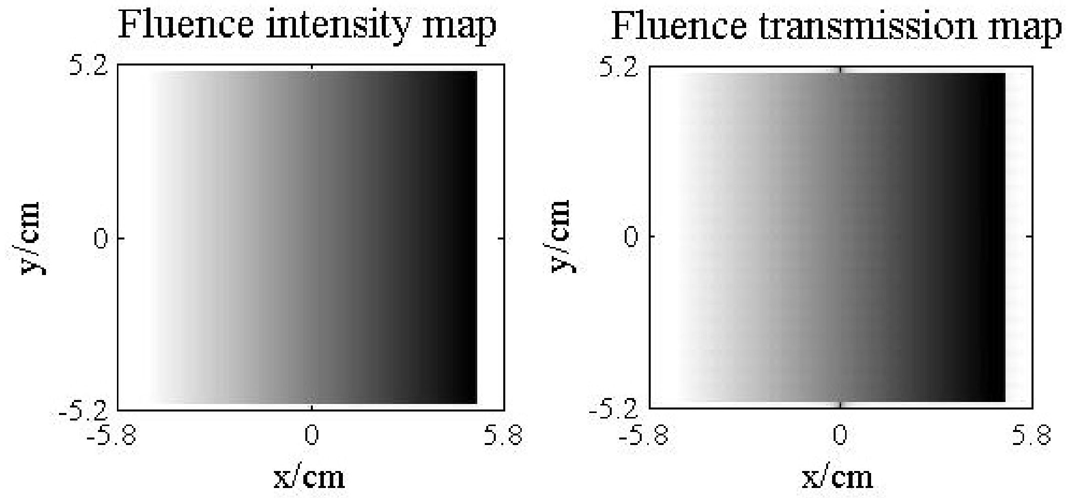

Figure 5.17: Fluence intensity map and fluence transmission map of the dynamic wedge field used in open field measurements

The results confirm what we expected for the fields in Figures 5.6d and 5.6e. The relative difference between the Monte-Carlo and the measurement is respectively 0.3 % and 7.3 %; but more importantly, we see that the uncertainty of the relative difference is about 15 %, and it is mostly due to the uncertainty due to the positioning of the chamber. On the other hand, for the field in Figure 5.6h, for which the positioning plays no important role, the uncertainty on the relative difference between Monte-Carlo and measurement is 3.7 %, which is the statistical uncertainty of the kernel summation itself. Except for both fields we have just mentioned, the relative difference is always good and below 4 %.

However, we must say that even when we are not limited by the positioning uncertainty, we still have a fairly large statistical uncertainty of 3.7 % due to a lack of statistics in the kernel simulations and to the very large number of interpolated points. We can estimate that we should divide this uncertainty by four if we interpolated four times as less points from the calculated points, *i.e.*, if the kernel resolution were 0.02 cm instead of 0.01 cm. However, by doing so, we should introduce systematic effects.

6 MV, $z = 10$ cm	Relative Cavity Dose (RCD)		
100 cm SSD	Experiment	MC kernel summation	Relative difference (%)
Closed	0.0933 ± 0.0001	0.091 ± 0.007	2.9 ± 7.0
5×10 right	0.5418 ± 0.0004	0.550 ± 0.041	1.5 ± 7.3
5×10 left	0.5506 ± 0.0003	0.541 ± 0.041	1.8 ± 7.6
10×5 down	0.5488 ± 0.0003	0.550 ± 0.087	0.3 ± 15.6
10×5 up	0.5009 ± 0.0003	0.541 ± 0.087	7.3 ± 14.8
10×1	0.7596 ± 0.0005	0.791 ± 0.032	4.0 ± 3.8
1×10	0.4715 ± 0.0004	0.459 ± 0.021	2.9 ± 4.7
8×8	0.9760 ± 0.0008	0.978 ± 0.037	0.2 ± 3.7
6×6	0.9434 ± 0.0007	0.949 ± 0.036	0.6 ± 3.7
4×4	0.8927 ± 0.0007	0.907 ± 0.035	1.6 ± 3.7
dyn. wedge	0.5079 ± 0.0004	0.515 ± 0.022	1.4 ± 4.1

Table 5.4: Comparison of dose-to-air kernel summation to measurements in static open fields.

5.7 Kernel summation and measurements with IMRT fields

Twelve IMRT fields from actual IMRT treatment plans were selected. They were submitted to the code algorithm and RCD values were obtained for each one of them with the kernel summation method. They were also delivered with a Varian® Clinac 6EX equipped with a 120 Millenium multileaf collimator. The plans were delivered in the conditions of patient-specific quality assurance, *i.e.*, on a Solid Water® phantom whose dimensions were $30 \times 30 \times 17$ cm^3. A Exradin A12 Farmer chamber was placed with its centroid at the centre of the phantom. In order to compare Monte-Carlo and experimental measurements, the kernels used in the summation had been specifically simulated in a Solid Water® phantom with the chamber model embedded at the same depth as in the experiment.

Similarly to the case of open fields, Figures 5.18 to 5.29 represent the fluence intensity maps and the fluence transmission maps of the 12 IMRT fields that we measured. The chamber is positioned along the x axis, with its centroid at $(0, 0)$. The transmission maps show the effects of leakage, of interleaf transmission and of the rounded leaf ends. In particular, we can always see a non negligible transmission on the right of the fields; it is explained by the fact that it was a sliding window delivery mode starting with the abutting leaf ends on the right of the fields.

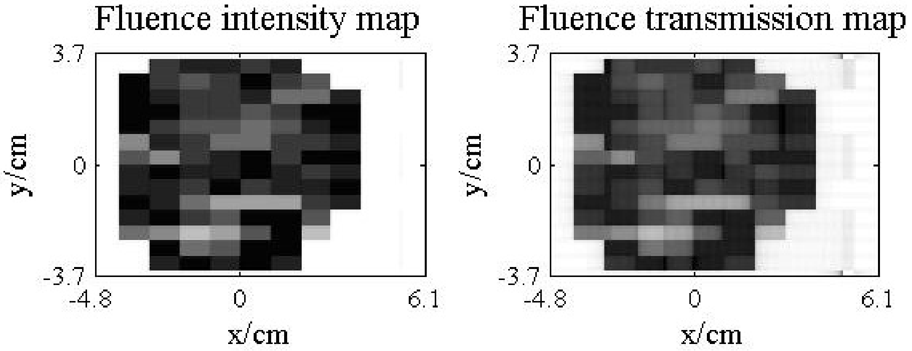

Figure 5.18: Fluence intensity map and fluence transmission map of the dynamic field #1 used in IMRT field measurements

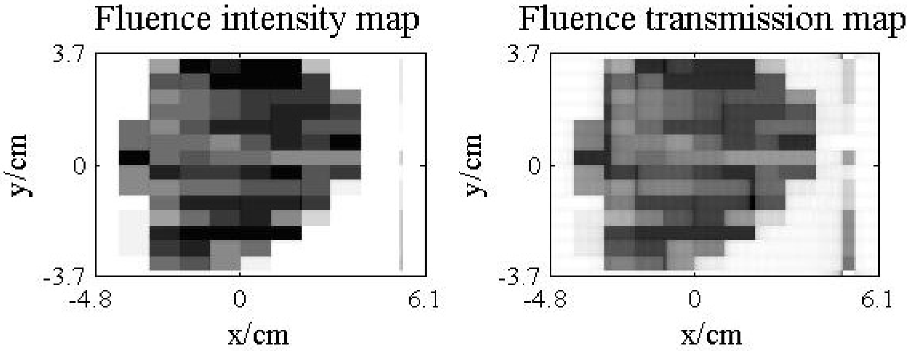

Figure 5.19: Fluence intensity map and fluence transmission map of the dynamic field #2 used in IMRT field measurements

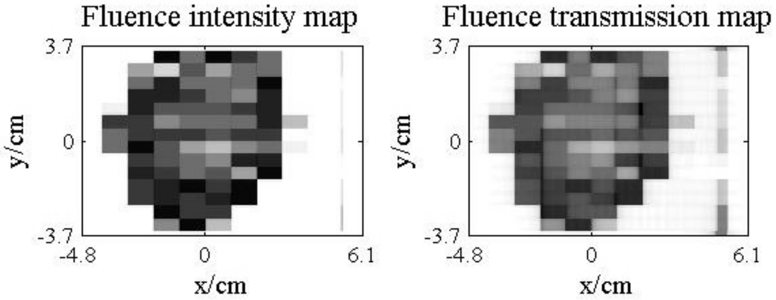

Figure 5.20: Fluence intensity map and fluence transmission map of the dynamic field #3 used in IMRT field measurements

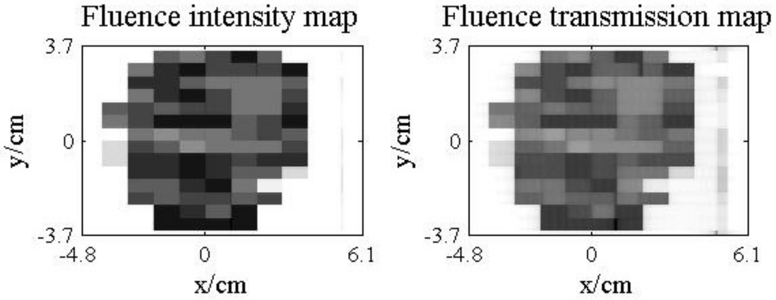

Figure 5.21: Fluence intensity map and fluence transmission map of the dynamic field #4 used in IMRT field measurements

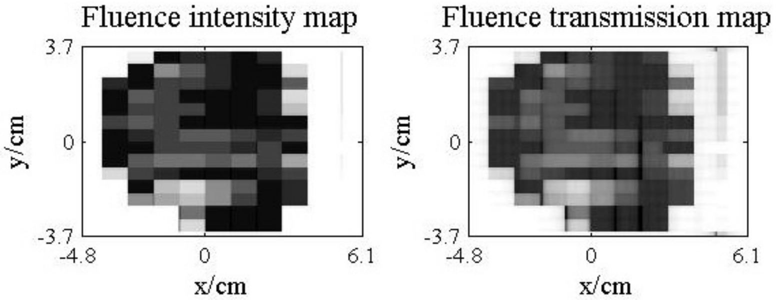

Figure 5.22: Fluence intensity map and fluence transmission map of the dynamic field #5 used in IMRT field measurements

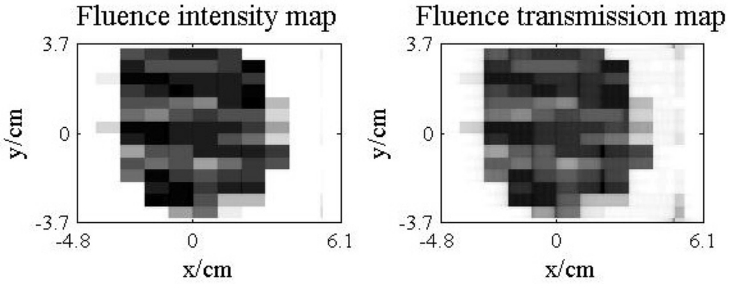

Figure 5.23: Fluence intensity map and fluence transmission map of the dynamic field #6 used in IMRT field measurements

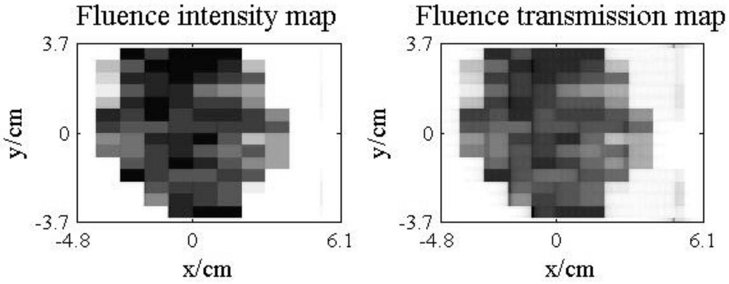

Figure 5.24: Fluence intensity map and fluence transmission map of the dynamic field #7 used in IMRT field measurements

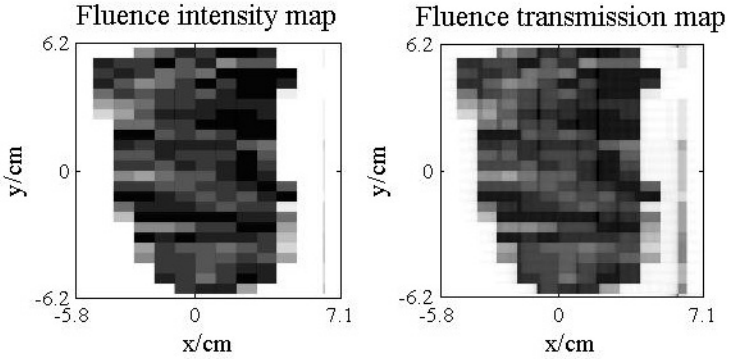

Figure 5.25: Fluence intensity map and fluence transmission map of the dynamic field #8 used in IMRT field measurements

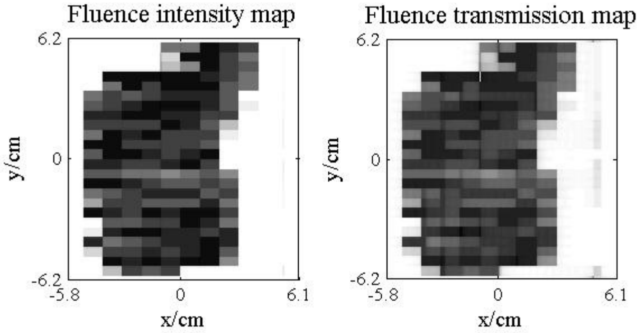

Figure 5.26: Fluence intensity map and fluence transmission map of the dynamic field #9 used in IMRT field measurements

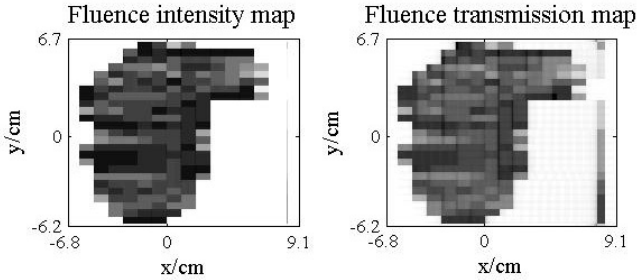

Figure 5.27: Fluence intensity map and fluence transmission map of the dynamic field #10 used in IMRT field measurements

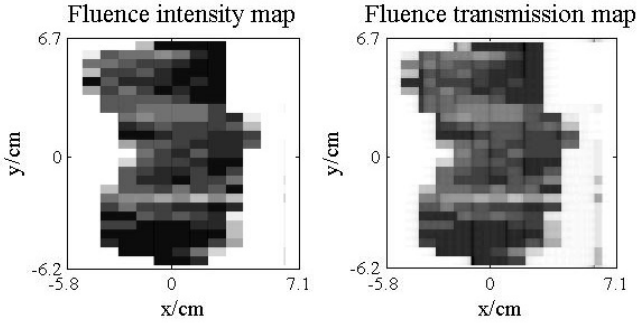

Figure 5.28: Fluence intensity map and fluence transmission map of the dynamic field #11 used in IMRT field measurements

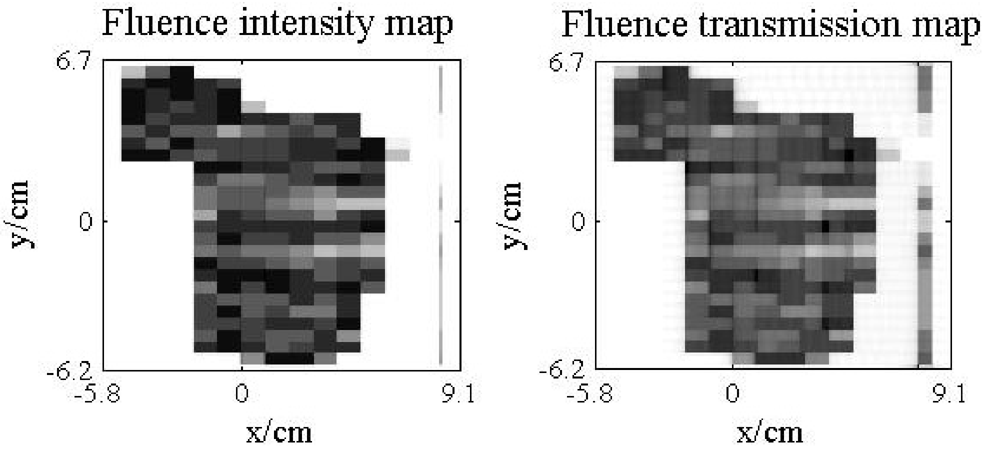

Figure 5.29: Fluence intensity map and fluence transmission map of the dynamic field #12 used in IMRT field measurements

6 MV, $z = 10$ cm	Relative Cavity Dose (RCD)		
100 cm SAD	Experiment	MC kernel summation	Relative difference (%)
Dynamic #1	0.451	0.459 ± 0.017	1.7 ± 3.7
Dynamic #2	0.342	0.349 ± 0.020	2.0 ± 5.7
Dynamic #3	0.283	0.288 ± 0.025	1.7 ± 8.6
Dynamic #4	0.348	0.350 ± 0.013	0.5 ± 3.8
Dynamic #5	0.338	0.344 ± 0.013	1.8 ± 3.7
Dynamic #6	0.505	0.510 ± 0.019	0.9 ± 3.7
Dynamic #7	0.477	0.483 ± 0.018	1.3 ± 3.8
Dynamic #8	0.403	0.407 ± 0.016	1.1 ± 4.0
Dynamic #9	0.543	0.550 ± 0.021	1.3 ± 3.7
Dynamic #10	0.354	0.355 ± 0.013	0.3 ± 3.8
Dynamic #11	0.455	0.460 ± 0.017	1.1 ± 3.8
Dynamic #12	0.366	0.515 ± 0.015	1.5 ± 3.9

Table 5.5: Comparison of dose-to-air kernel summation to measurements in dynamic IMRT fields.

Table 5.5 shows the results of the measurements of the selected IMRT fields compared with the Monte-Carlo kernel summation. No uncertainty is shown for the experimental results because of their high reproducibility. The experimental uncertainties are always negligible compared to the kernel summation uncertainties. The column with the Monte-Carlo results shows uncertainties combining the statistical component from the variance reduction and the component due the positioning uncertainty. Although it is not shown in the table, the statistical component, about 3.7 %, was always higher than the positioning one.

The agreement between Monte-Carlo and experimental measurements appear to be very good, with a relative difference below 2 %. However, as we explained in the previous section, we are limited by an uncertainty of 3.7 % due to a lack of statistics in the kernels (see 72). The remedy would be either to acquire kernels with more statistics or to interpolate the kernels to a smaller number of points. The former solution would be time consuming as it would take four times as much CPU time (about two weeks at the CLUMEQ Supercomputer Centre) to acquire one chamber kernel, only to divide the uncertainty by two. The latter solution would be a slight gain of time because we should need to interpolate only half of the points[1] we actually acquired, with a computing time of about 2 min on a laptop.

---

[1] Equations A.9 and A.16 show that the standard deviation is proportional to the number of interpolated points.

Chapter 6

Conclusion

6.1 Summary

Ionisation chamber measurements of IMRT fields are complicated by the fact that these fields do not comply with the dosimetry reference protocols AAPM TG-51 and IAEA TRS-398. Therefore, there is a need for a reference dosimetry protocol for nonstandard beams. In this thesis, we investigated the accuracy of chamber modelling to nonstandard beam configurations. To this end, a realistic model of the Exradin® A12 Farmer chamber was created. The response of the modelled chamber to pencil beams was calculated and the response to an arbitrary reconstructed field was determined. As a benchmark, the calculation was tested in open field reference conditions by comparison to direct Monte-Carlo calculation. Pencil-beam dose-to-air response kernels were created for the chamber, as well as dose-to-water response kernels. The kernel summation method was tested against direct simulations. Finally the kernel summation was used to calculate chamber response with static open fields as well as dynamic MLC IMRT fields. The results were compared to experimental measurements.

Beam quality conversion factor calculations on relative absorbed dose to water calibration coefficients agreed with TG-51 values within 0.1 % and 0.4 % for 6 MV and 18 MV photon beams, respectively. The profiles calculated for the chamber revealed the importance of the details of its geometry. In particular, the effect of the central electrode was responsible for a dose-response relative increase of 43 % when a pencil beam was swept across the chamber. The comparison of the kernel summation and a direct Monte-Carlo simulation showed a relative agreement within 0.1 % for the calculation of the conversion factor of a 6 MV photon beam. Kernel summations with open fields compared well with the measurements, with an agreements within 0.2 % and 4.0 %, except for a field, for which the effect of positioning uncertainty was large, and which showed a relative difference of 7.3 %. Similarly, the comparison with measurements with IMRT fields showed relative agreements within 2.0 %, as the positioning was not as critical as in the case of open fields.

The variance on the kernel summation using an uncertainty combination technique was developed, and it revealed that the standard deviation is proportional to the number of interpolated points in the kernel. The kernels we acquired led to a statistical limit of 3.7 %. As a consequence, the statistical uncertainty is of the same order of magnitude as the uncertainty due to the positioning, and sometimes it is even larger. Nonetheless, the kernel summation method associated with the realistic chamber model showed very promising results. Moreover, we could show how the geometry of the chamber was influencing its response, and we showed that the positioning accuracy was sometimes critical.

6.2 Future work

The acquisition of additional data for the pencil-beam kernels, which should yield statistical uncertainties of the order of 0.1 %, is the immediate task that should be undertaken. The comparison with experimental measurements would be more conclusive.

From this point on, two paths can be followed. Other chambers can be modelled and compared with each other in order to study in detail the effect of the chamber design on its response to radiation, particularly nonstandard beams. The other path, which was originally Bouchard and Seuntjens's goal, is to perform dose-to-water measurements to calculate and compare IMRT correction factors. With a benchmarked chamber model, it will be possible to create a three-dimensional map of the IMRT conversion factor to help the decision on where to place the ionisation chamber when performing the patient-specific quality assurance.

Finally, we need to keep in mind that the ultimate goal of this subject is the production of a new protocol for the dosimetry of nonstandard beams—IMRT, tomotherapy—that do not comply with reference protocols.

Appendix A

Statistics in kernel summation

In this appendix, we develop an uncertainty combination technique to calculate the variance on the summation of kernels acquired by Monte-Carlo simulation and by interpolation of the simulated points. The technique is used to report standard deviations on the kernels summations throughout this thesis.

A.1 Rationale

The detailed kernels used in this analysis are obtained in two stages. The first stage is a data sampling of dose responses using EGSnrc/CAVITY. The dose responses are calculated on an irregular grid of points in a 10×10 cm^2 field. These points are carefully chosen to keep as many details as possible of the water voxel or the chamber geometry, but their number has to be limited (for example, by using the symmetry of the geometry) so that the simulation running time be kept reasonably short (*e.g.*, a couple of days). At this point, all dose responses calculated are statistically independent from each other, but the kernels cannot be used in this state because the grid size is irregular and too coarse.

In the second stage, the calculated data are interpolated to obtain detailed kernels on a regular and fine grid of points in the 10×10 cm^2 field. Typically, for the chamber geometry, the data are interpolated from a 46×37 irregular grid to a 1001×1001 regular one. The result is kernels with a very fine definition (0.01 mm^2 cells) that will be used for summations.

The problem is that, after the interpolation process, the dose responses in the detailed kernels are no longer statistically independent. A summation of these kernels will therefore introduce covariance terms when we calculate the summation variance. The difficulty *per se* appears when we consider that the summation of 1001^2 statistically dependent dose responses involves a $1001^2 \times 1001^2$ covariance matrix that requires about eight terabytes of memory to store[1]. We present in this appendix how we solved this problem.

A.2 A simple one-dimensional case

Let us consider a simple case with two points x_1 and x_2. At these points, the statistically independent dose responses $z(x_1)$ and $z(x_2)$ are calculated, with variances $\sigma^2_{z(x_1)}$ and $\sigma^2_{z(x_2)}$. We then divide the segment between x_1 and x_2 in $m-1$ equal segments defined between points y_1 and y_2 through y_{m-1} and y_m, with $y_1 = x_1$ and $y_m = x_2$. By linear interpolation, we get the dose responses $z(y_i)$:

$$\begin{aligned} z(y_i) &= \left(1 - \frac{i-1}{m-1}\right) z(x_1) + \frac{i-1}{m-1} z(x_2)\,, \qquad i \in [1,m] && \text{(A.1)} \\ &= z(x_1) + \frac{i-1}{m-1}(z(x_2) - z(x_1))\,. && \text{(A.2)} \end{aligned}$$

The variance $\sigma^2_{z(x_i)}$ of each dose response $z(y_i)$ is given by:

$$\sigma^2_{z(x_i)} = \left(1 - \frac{i-1}{m-1}\right)^2 \sigma^2_{z(x_1)} + \left(\frac{i-1}{m-1}\right)^2 \sigma^2_{z(x_2)}\,, \qquad i \in [1,m]. \tag{A.3}$$

Now, let us define the total sum S of our one-dimensional kernel. It is calculated as follows:

$$S = \sum_{i=1}^{m} z(y_i)\,, \tag{A.4}$$

and the variance of S is given by:

$$\sigma^2_S = \sum_{i=1}^{m} \sigma^2_{z(x_i)} + 2 \sum_{i=1}^{m} \sum_{j=i+1}^{m} \sigma_{z(x_i)z(x_j)}\,. \tag{A.5}$$

The second term in the equation of the variance is the sum of covariances. We can already see with a simple example that the expression of the variance of S can become

---

[1] Calculations are performed with doubles in C language, and the size of a double is eight bytes.

cumbersome, with a lot of terms to calculate and to sum up. However, there is a simpler way to calculate σ_S^2 if, from Equations A.2 and A.4, we rewrite S as follows:

$$\begin{aligned} S &= \sum_{i=1}^{m} \left(z(x_1) + \frac{i-1}{m-1} \left(z(x_2) - z(x_1) \right) \right) && \text{(A.6)} \\ &= m \cdot z(x_1) + \frac{1}{m-1} \frac{m(m-1)}{2} \left(z(x_2) - z(x_1) \right) && \text{(A.7)} \\ &= \frac{m}{2} \left(z(x_1) + z(x_2) \right) . && \text{(A.8)} \end{aligned}$$

The advantage of this last expression of S is that all the terms involved are statistically independent because they are the terms calculated during the Monte-Carlo simulation. As a consequence, the expression of the variance of S does not have any covariance term, as can be seen here:

$$\sigma_S^2 = \left(\frac{m}{2} \right)^2 \left(\sigma_{z(x_1)}^2 + \sigma_{z(x_2)}^2 \right) . \tag{A.9}$$

A.3 A simple two-dimensional case

Now, let us define a rectangle whose coordinates are (x_1, y_1), (x_m, y_1), (x_m, y_n) and (x_1, y_n), where m and n are two integers. Dose responses are calculated by Monte-Carlo at these coordinates. They are statistically independent.

A regular grid is defined on this rectangle, with $(m-1) \times (n-1)$ cells with dimensions $\Delta x \times \Delta y$, where $\Delta x = \frac{x_m - x_1}{m-1}$ and $\Delta y = \frac{y_n - y_1}{m-1}$.

At each point (x_i, y_j), a dose response is calculated by linear interpolation from the four dose responses calculated by Monte-Carlo at the corners of the rectangle. Let us define t_i and u_j:

$$\begin{aligned} t_i = \frac{x_i - x_1}{x_m - x_1} &= \frac{i-1}{m-1} , \qquad i \in [1, m] && \text{(A.10)} \\ u_j = \frac{y_j - y_1}{y_n - y_1} &= \frac{j-1}{n-1} , \qquad j \in [1, n] . && \text{(A.11)} \end{aligned}$$

Each interpolated dose response $z(x_i, y_j)$ is then calculated as follows:

$$z(x_i, y_j) = (1-t_i)(1-u_j) z(x_1, y_1) + t_i(1-u_j) z(x_m, y_1) + (1-t_i) u_j z(x_1, y_n) + t_i u_j z(x_m, y_n) . \tag{A.12}$$

We have now a detailed $(m-1)\times(n-1)$ dose kernel calculated from four statistically independent dose responses.

The sum S of the dose kernel is given by:

$$S = \sum_{i=1}^{m}\sum_{j=1}^{n} z(x_i, y_j)\ . \tag{A.13}$$

Again, it would be very difficult to calculate the variance of S directly from Equation A.13 because of the covariance terms that would appear. We need to replace the expression of the dose response in the equation, in order to express S solely with the dose responses that were calculated by Monte-Carlo and that are statistically independent.

After a calculation similar to that in Equations A.6 to A.8, we get:

$$\begin{aligned} S &= \frac{mn}{4}\left[z(x_1,y_1)+z(x_m,y_n)+z(x_1,y_n)+z(x_m,y_1)\right] && \text{(A.14)}\\ &= \frac{1}{4}\left(\frac{x_m+\Delta x-x_1}{\Delta x}\right)\left(\frac{y_n+\Delta y-y_1}{\Delta y}\right) \\ &\quad\times\left[z(x_1,y_1)+z(x_m,y_n)+z(x_1,y_n)+z(x_m,y_1)\right]\ , && \text{(A.15)}\end{aligned}$$

and the variance σ_S^2 is easily given by:

$$\begin{aligned} \sigma_S^2 &= \frac{1}{16}\left(\frac{x_m+\Delta x-x_1}{\Delta x}\right)^2\left(\frac{y_n+\Delta y-y_1}{\Delta y}\right)^2 \\ &\quad\times\left[\sigma^2_{z(x_1,y_1)}+\sigma^2_{z(x_m,y_n)}+\sigma^2_{z(x_1,y_n)}+\sigma^2_{z(x_m,y_1)}\right]\ . && \text{(A.16)}\end{aligned}$$

A.4 General case: chamber kernel summation

In the general case of a chamber kernel, we do not have four dose responses on the corners of one rectangle, but 46 × 37 dose responses on an irregular grid covering only half of the chamber for symmetry reasons (see Figure A.1). In our analysis, the cells in the regular grid are square ($\Delta x = \Delta y = \epsilon$), and their dimension ϵ is chosen so that the number of cells in any rectangle of the irregular grid is an integer.

We are going to use the results of the previous section to sum the dose-to-air kernel. We shall have to be careful not to count twice the dose contributions at the borders of the rectangles, even though the effect should be negligible. For that, we are going to use the result in Equation A.15 for every rectangle of the irregular grid. Then, we shall subtract every dose contribution that was counted twice.

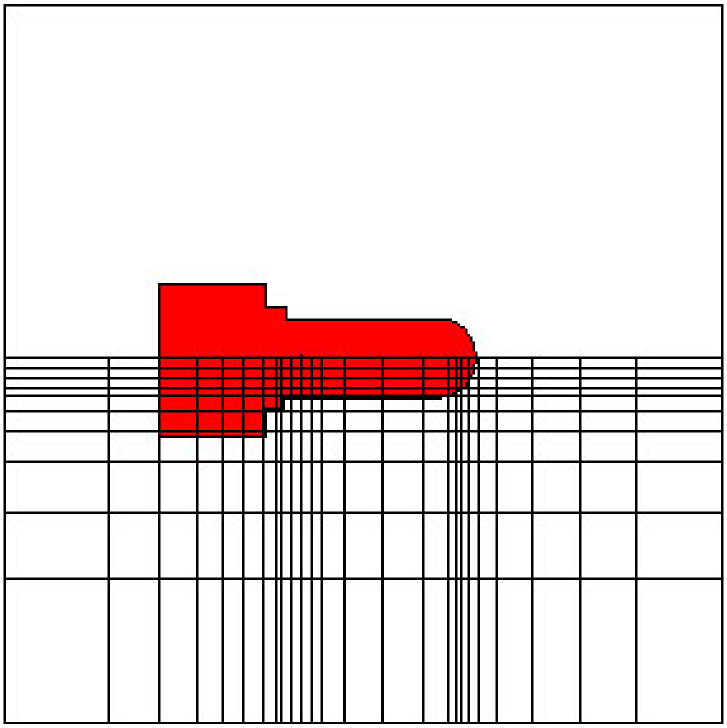

Figure A.1: Illustration of the coarse irregular grid from which dose responses are calculated with the Monte-Carlo code. Dose responses are then interpolated on a fine regular grid to obtain a detailed dose-to-air kernel.

Let us note S_{kl} the sum of interpolated dose responses in the rectangle defined by (x_k, y_l), (x_{k+1}, y_l), (x_{k+1}, y_{l+1}) and (x_k, y_{l_1}) (with $k \in [1, 45]$ and $l \in [1, 36]$). S_{kl} is given by:

$$\begin{aligned} S_{kl} &= \frac{1}{4}\left(\frac{x_{k+1}+\epsilon-x_k}{\epsilon}\right)\left(\frac{y_{l+1}+\epsilon-y_l}{\epsilon}\right) \\ &\quad \times \left[z(x_k, y_l) + z(x_{k+1}, y_{l+1}) + z(x_k, y_{l+1}) + z(x_{k+1}, y_l)\right] . \end{aligned} \tag{A.17}$$

The total sum S_{tot} of the kernel is the sum of all S_{kl}, multiplied by 2 for the symmetry of the chamber, minus the contributions that are counted more than once. Let us call S_{over} the sum of these over-contributions. S_{tot} can be written as:

$$S_{\text{tot}} = 2\sum_{k=1}^{45}\sum_{l=1}^{36} S_{kl} - S_{\text{over}} . \tag{A.18}$$

Let us calculate the double summation first:

$$\begin{aligned} S_{\text{tot}} + S_{\text{over}} &= \frac{1}{2}\sum_{k=1}^{45}\sum_{l=1}^{36}\frac{x_{k+1}+\epsilon-x_k}{\epsilon}\frac{y_{l+1}+\epsilon-y_l}{\epsilon} \\ &\quad \times\left[z(x_k,y_l)+z(x_{k+1},y_{l+1})+z(x_k,y_{l+1})+z(x_{k+1},y_l)\right] \qquad \text{(A.19)} \end{aligned}$$

We now are going to rewrite the double sum in a way so that each dose response $z(x_k, y_l)$ appears only once:

$$\begin{aligned} S_{\text{tot}} + S_{\text{over}} &= \frac{1}{2}\sum_{k=2}^{45}\frac{x_{k+1}+2\epsilon-x_{k-1}}{\epsilon}\left[\sum_{l=2}^{36}\frac{y_{l+1}+2\epsilon-y_{l-1}}{\epsilon}z(x_k,y_l)\right. \\ &\qquad \left.+\frac{y_2+\epsilon-y_1}{\epsilon}z(x_k,y_1)+\frac{y_{37}+\epsilon-y_{36}}{\epsilon}z(x_k,y_{37})\right] \\ &+ \frac{1}{2}\frac{x_2+\epsilon-x_1}{\epsilon}\left[\sum_{l=2}^{36}\frac{y_{l+1}+2\epsilon-y_{l-1}}{\epsilon}z(x_1,y_l)\right. \\ &\qquad \left.+\frac{y_2+\epsilon-y_1}{\epsilon}z(x_1,y_1)+\frac{y_{37}+\epsilon-y_{36}}{\epsilon}z(x_1,y_{37})\right] \\ &+ \frac{1}{2}\frac{x_{46}+\epsilon-x_{45}}{\epsilon}\left[\sum_{l=2}^{36}\frac{y_{l+1}+2\epsilon-y_{l-1}}{\epsilon}z(x_{46},y_l)\right. \\ &\qquad \left.+\frac{y_2+\epsilon-y_1}{\epsilon}z(x_{46},y_1)+\frac{y_{37}+\epsilon-y_{36}}{\epsilon}z(x_{46},y_{37})\right]. \qquad \text{(A.20)} \end{aligned}$$

We now need to express S_{over}. The over-contributions come from the fact that the dose responses at the borders of more than one rectangle are counted twice. They are even counted four times because of the kernel symmetry. Moreover, the dose responses at corners common to four rectangles are counted eight times, symmetry included. Finally, the contribution on the chamber axis (at y_1) is counted once too many when the sum is multiplied by two to account for the symmetry. S_{over} is given by:

$$\begin{aligned} S_{\text{over}} &= 2\left[\frac{1}{2}\sum_{l=2}^{36}\sum_{k=1}^{45}\frac{x_{k+1}+\epsilon-x_k}{\epsilon}\left(z(x_k,y_l)+z(x_{k+1},y_l)\right)\right. \\ &\qquad \left.+\frac{1}{2}\sum_{k=2}^{45}\sum_{l=1}^{36}\frac{y_{l+1}+\epsilon-y_l}{\epsilon}\left(z(x_k,y_l)+z(x_k,y_{l+1})\right)-\sum_{k=2}^{45}\sum_{l=2}^{36}z(x_k,y_l)\right] \\ &+ \left[\frac{1}{2}\sum_{k=1}^{45}\frac{x_{k+1}+\epsilon-x_k}{\epsilon}\left(z(x_k,y_1)+z(x_{k+1},y_1)\right)-\sum_{k=2}^{45}z(x_k,y_1)\right], \qquad \text{(A.21)} \end{aligned}$$

which we can rewrite conveniently as follows:

$$\begin{aligned}
S_{\text{over}} &= \sum_{l=2}^{36}\left(\sum_{k=2}^{45}\frac{x_{k+1}+2\epsilon-x_{k-1}}{\epsilon}z(x_k,y_l)+\frac{x_2+\epsilon-x_1}{\epsilon}z(x_1,y_l)+\frac{x_{46}+\epsilon-x_{45}}{\epsilon}z(x_{46},y_l)\right)\\
&+ \sum_{k=2}^{45}\left(\sum_{l=2}^{36}\frac{y_{l+1}+2\epsilon-y_{l-1}}{\epsilon}z(x_k,y_l)+\frac{y_2+\epsilon-y_1}{\epsilon}z(x_k,y_1)+\frac{y_{37}+\epsilon-y_{36}}{\epsilon}\right)\\
&+ \frac{1}{2}\left(\sum_{k=2}^{45}\frac{x_{k+1}+2\epsilon-x_{k-1}}{z}(x_k,y_1)+\frac{x_2+\epsilon-x_1}{\epsilon}z(x_1,y_1)+\frac{x_{46}+\epsilon-x_{45}}{\epsilon}z(x_{46},y_1)\right)\\
&- 2\sum_{k=2}^{45}\sum_{l=2}^{36}z(x_k,y_l)-\sum_{k=2}^{45}z(x_k,y_1)\,. \qquad \text{(A.22)}
\end{aligned}$$

S_{tot} is obtained by subtracting Equation A.22 from Equation A.20. The result, in our analysis, is the kernel summation for the chamber in a 10 × 10 cm^2 field. After rearrangements of the terms in the equation, so that each $z(x_k, y_l)$ appears only once, we get:

$$\begin{aligned}
2S_{\text{tot}} &= \sum_{k=2}^{45}\frac{x_{k+1}-x_{k-1}}{\epsilon}\left(\sum_{l=2}^{36}\frac{y_{l+1}-y_{l-1}}{\epsilon}z(x_k,y_l)+\frac{y_2-y_1}{\epsilon}z(x_k,y_1)+\frac{y_{37}+\epsilon-y_{36}}{\epsilon}z(x_k,y_{37})\right)\\
&+ \frac{x_2+\epsilon-x_1}{\epsilon}\left(\sum_{l=2}^{36}\frac{y_{l+1}-y_{l-1}}{\epsilon}z(x_1,y_l)+\frac{y_2-y_1}{\epsilon}z(x_1,y_1)+\frac{y_{37}+\epsilon-y_{36}}{\epsilon}z(x_1,y_{37})\right)\\
&+ \frac{x_{46}+\epsilon-x_{45}}{\epsilon}\left(\frac{y_2-y_1}{\epsilon}z(x_{46},y_1)+\frac{y_{37}+\epsilon-y_{36}}{\epsilon}z(x_{46},y_{37})-\sum_{l=2}^{36}z(x_{46},y_l)\right)\,. \qquad \text{(A.23)}
\end{aligned}$$

It is now very easy to calculate the variance of S_{tot}, and its formula can be derived in a similar way to that what was done in Equations A.15 and A.16.

For the summation of the dose-to-water kernel, a similar formula to Equation A.23 is used. The difference resides in the fact that for the dose-to-water kernel summation, two extra symmetries need to be accounted for, as illustrated in Figure A.2.

Finally, we need to make a remark about kernel summations in IMRT conditions. The kernel summation is similar to Equation A.13, but each kernel component is weighted by the product of the transmission function and the radial fluence (see Equation 4.4 p. 47). Simplifications leading to the result in Equation A.23 are no longer possible. To solve this difficulty, we have replaced the weight by its mean value. In the case of the dose-to-air kernel, the mean value of the weight is simply the relative cavity dose (RCD), whereas it

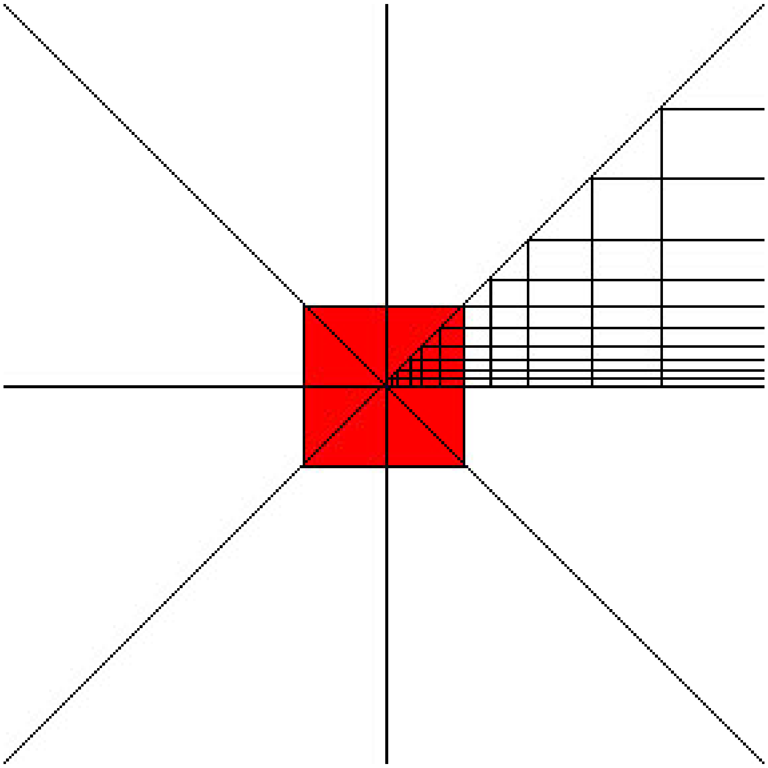

Figure A.2: Illustration of the coarse irregular grid from which dose responses in water are calculated with the Monte-Carlo code. Dose responses are then interpolated on a fine regular grid to obtain a detailed dose-to-water kernel.

is the relative dose factor (RDF) in the case of the dose-to-water kernel. In other words, the variance of the kernel summation in IMRT conditions is the variance of S_{tot} for air or water multiplied by RCD^2 or by RDF^2.

Bibliography

Agazaryan, N., T. D. Solberg, and J. J. DeMarco (2003). Patient specific quality assurance for the delivery of intensity modulated radiotherapy. *J. Appl. Clin. Med. Phys.* **4**(1), 40–50.

Ahnesjö, A. and M. M. Aspradakis (1999). Dose calculations for external photon beams in radiotherapy. *Phys. Med. Biol.* **44**, R99–R155.

Ahnesjö, A., B. Hårdemark, U. Isacsson, and A. Montelius (2006). The IMRT information process—mastering the degrees of freedom in external beam therapy. *Phys. Med. Biol.* **51**, R381–R402.

Almond, P. R., P. J. Biggs, B. M. Coursey, W. F. Hanson, M. S. Huq, R. Nath, and D. W. O. Rogers (1999). AAPM's TG-51 protocol for clinical reference dosimetry of high-energy photon and electron beams. *Med. Phys.* **26**(9), 1847–1870.

Andreo, P., D. T. Burns, K. Hohlfeld, M. S. Huq, F. Kanai, T. Laitano, V. Smyth, and S. Vynckier (2004). Absorbed dose determination in external beam radiotherapy: an international code of practice for dosimetry based on standards of absorbed dose to water. TRS-398, International Atomic Energy Agency, Vienna, Austria.

Andreo, P., J. R. Cunningham, K. Hohlfeld, and H. Svensson (1987). Absorbed dose determination in photon and electron beams: An international code of practice. TRS-277, International Atomic Energy Agency, Vienna, Austria.

Arnfield, M. R., J. V. Siebers, J. O. Kim, Q. Wu, P. J. Keall, and R. Mohan (2000).

A method for determining multileaf collimator transmission and scatter for dynamic intensity modulated radiotherapy. *Med. Phys.* **27**(10), 2231–2241.

Arnfield, M. R., Q. Wu, S. Tong, and R. Mohan (2001). Dosimetric validation for multileaf collimator-based intensity-modulated radiotherapy: a review. *Med. Dosim.* **26**(2), 179–188.

Auger, P. (1926). L'effet photoélectrique composé. *Ann. Phys. (Paris)* **10**(6), 183.

Bayouth, J. E. and M. Morrill (2003). MLC dosimetric characteristics for small field and IMRT applications. *Med. Phys.* **30**(9), 2545–2552.

Berger, M. J. (1963). Monte Carlo calculation of the penetration and diffusion of fast charged particles. In S. F. B. Alder and M. Rotenberg (Eds.), *Methods in Comput. Phys.*, Volume 1, pp. 135–215. New York: Academic.

Bhabha, H. J. (1936). The Scattering of Positrons by Electrons with Exchange on Dirac's Theory of the Positron. *Proceedings of the Royal Society of London. Series A, Mathematical and Physical Sciences* **154**(881), 195–206.

Bielajew, A. F., H. Hirayama, W. R. Nelson, and D. W. O. Rogers (1994). History, overview and recent improvements of EGS4. PIRS-0436, National Research Council of Canada, Ottawa, Canada.

Boehmer, D., J. Bohsung, I. Eichwurzel, A. Moys, and V. Budach (2004). Clinical and physical quality assurance for intensity-modulated radiotherapy of prostate cancer. *Radiother. Oncol.* **71**, 319–325.

Bogner, L., J. Scherer, M. Treutwein, M. Hartmann, F. Gum, and A. Amediek (2004). Verification of IMRT: techniques and problems. *Strahlenter. Onkol.* **34**(6), 340–350.

Bortfeld, T. (2006). IMRT: a review and preview. *Phys. Med. Biol.* **51**, R363–R379.

Bortfeld, T., W. Schlegel, and B. Rhein (1993). Decomposition of pencil beam kernels for fast dose calculations in three-dimensional treatment planning. *Med. Phys.* **20**(2), 311–318.

Bortfeld, T. R., A. L. Boyer, W. Schlegel, D. L. Kahler, and T. J. Waldron (1994b). Realisation and verification of three-dimensional conformal radiotherapy with modulated fields. *Int. J. Radiat. Oncol. Biol. Phys.* **30**, 899–908.

Bortfeld, T. R., D. Kahler, T. J. Waldron, and A. L. Boyer (1994a). X-ray field compensation with multileaf collimators. *Int. J. Radiat. Oncol. Biol. Phys.* **28**, 723–730.

Both, S., I. M. Alecu, A. R. Stan, M. Alecu, A. Ciura, J. M. Hansen, and R. Alecu (2007). A study to establish reasonable action limits for patient-specific quality assurance in intensity-modulated radiation therapy. *J. Appl. Clin. Med. Phys.* **8**(2), 1–8.

Bouchard, H. (2003). Accurate dosimetry of Intensity Modulated Radiation Therapy beams using thimble ionization chambers. Master's thesis, Medical Physics Unit, McGill University, Montreal, QC.

Bouchard, H. and J. Seuntjens (2004). Ionization chamber-based reference dosimetry of intensity modulated radiation beams. *Med. Phys.* **31**(9), 2454–2465.

Boyer, A. L., P. Biggs, J. Galvin, E. Klein, T. LoSasso, D. Low, K. Mah, and C. Yu (2001b). Basic applications of multileaf collimators. Report 72 of TG-50 Radiation Therapy Committee, American Association of Physicists in Medicine.

Boyer, A. L., B. Butler, T. A. DiPetrillo, M. J. Engler, B. Fraass, W. Grant, III, C. Clifton Ling, D. A. Low, T. R. Mackie, R. Mohan, J. A. Purdy, M. Roach, J. G. Rosenman, L. J. Verhey, J. W. Wong, R. L. Cumberlin, H. Stone, and J. R. Palta (2001a). Intensity-modulated radiotherapy: current status and issues of interest. *Int. J. Radiat. Oncol. Biol. Phys.* **51**(4), 880–914.

Bragg, W. H. (1912). *Studies in radioactivity.* London, UK: Macmillan and Co.

Brahme, A., J.-E. Roos, and I. Lax (1982). Solution of an integral equation encountered in rotation therapy. *Phys. Med. Biol.* **27**(10), 1221–1229.

Brown, L. M. and R. P. Feynman (1952). Radiative Corrections to Compton Scattering. *Phys. Rev.* **85**(2), 231–244.

Buckley, L. A., I. Kawrakow, and D. W. O. Rogers (2003). An EGSnrc investigation of cavity theory for ion chambers measuring air kerma. *Med. Phys.* **30**(6), 1211–1218.

Burman, C., C.-S. Chui, G. Kutcher, S. Leibel, M. Zelefsky, T. LoSasso, S. Spirou, Q. Wu, J. Yang, J. Stein, R. Mohan, Z. Fuks, and C. C. Ling (1997). Planning, delivery, and quality assurance of intensity-modulated modulated radiotherapy using dynamic multileaf collimator: a strategy for large-scale implementation for the treatment of carcinoma of the prostate. *Int. J. Rad. Oncol. Biol. Phys.* **39**(4), 863–873.

Canadian Cancer Society (2007). Canadian Cancer Statistics 2007. Technical report, Canadian Cancer Society/National Cancer Institute of Canada, Toronto, Canada.

Capote, R., F. Sánchez-Doblado, A. Leal, J. I. Lagares, R. Arráns, and G. H. Hartmann (2004). An EGSnrc Monte Carlo study of the microionization chamber for reference dosimetry of narrow irregular IMRT beamlets. *Med. Phys.* **31**(9), 2416–2422.

Chow, C. L., G. N. Grigorov, and R. Jiang (2006). Intensity modulated radiation therapy with irregular multileaf collimated field: a dosimetric study on the penumbra region with different leaf stepping patterns. *Med. Phys.* **33**(12), 4606–4613.

Compton, A. H. (1923). A quantum theory of the scattering of x-rays by light elements. *Phys. Rev.* **21**(5), 483–502.

Convery, D. J. and M. E. Rosenbloom (1992). The generation of intensity-modulated fields for conformal radiotherapy by dynamic collimation. *Phys. Med. Biol.* **37**, 1359–1374.

Convery, D. J. and S. Webb (1998). Generation of discrete beam-intensity modulation by dynamic multileaf collimation under minimum leaf separation constraints. *Phys. Med. Biol.* **43**, 2521–2538.

Deng, J., T. Pawlicki, Y. Chen, J. Li, S. B. Jiang, and C.-M. Ma (2001). The MLC tongue-and-groove effect on IMRT dose distributions. *Phys. Med. Biol.* **46**, 1039–1060.

Desgraupes, B. (2000). *LaTeX - Apprentissage, guide et référence.* Paris, France: Vuibert.

Devic, S., J. Seuntjens, E. Sham, E. Podgoršak, C. Ross Schmidtlein, A. S. Kirov, and C. G. Soares (2005). Precise radiochromic film dosimetry using a flat-bed document scanner. *Med. Phys.* **32**(7), 2245–2253.

Einstein, A. (1905). On a heuristic point of view concerning the production and transformation of light [in German]. *Ann. Phys. (Leipzig)* **322**, 132–148.

Escudé, L., D. Linero, M. Mollà, and R. Miralbell (2006). Quality assurance for radiotherapy in prostate cancer: point dose measurements in intensity modulated fields with large dose gradients. *Int. J. Radiat. Oncol. Biol. Phys.* **66**(4 Suppl.), S136–S140.

Ezzell, G. A., J. M. Galvin, D. Low, J. R. Palta, I. Rosen, M. B. Sharpe, P. Xia, Y. Xiao, L. Xing, and C. X. Yu (2003). Guidance document on delivery, treatment planning, and clinical implementation of IMRT: Report of the IMRT subcommittee of the AAPM radiation therapy committee. *Med. Phys.* **30**(8), 2089–2115.

Fano, U. (1954). Note on the Bragg-Gray cavity principle for measuring energy dissipation. *Radiat. Res.* **1**(3), 237–240.

Followill, D. S. and F. Nüsslin (2007). Point/Counterpoint: IMRT should not be administered at photon energies greater than 10 MV. *Med. Phys.* **34**(6), 1877–1879.

Fraass, B. A. (1995). The development of conformal radiation therapy. *Med. Phys.* **22**(11), 1911–1921.

Fraser, D., J. Seuntjens, and W. Parker (2005). A comparison of three ionization chambers for IMRT patient specific quality assurance. *Med. Phys.* **32**(6), 2166.

Galvin, J. M., G. Ezzell, A. Eisbrauch, C. Yu, B. Butler, Y. Xiao, I. Rosen, J. Rosenman, M. Sharpe, L. Xing, P. Xia, T. Lomax, D. A. Low, and J. Palta (2004). Implementing IMRT in clinical practice: a joint document of the American Society for Therapeutic Radiology and Oncology and the American Association of Physicists in Medicine. *Int. J. Rad. Oncol. Biol. Phys.* **58**(5), 1616–1634.

Gray, L. H. (1929). The absorption of penetrating radiation. *Proc. R. Soc.* **122**(790), 647–668.

Guerrero Urbano, M. T. and C. M. Nutting (2004a). Clinical use of intensity-modulated radiotherapy: part I. *Br. J. Radiol.* **77**, 88–96.

Guerrero Urbano, M. T. and C. M. Nutting (2004b). Clinical use of intensity-modulated radiotherapy: part II. *Br. J. Radiol.* **77**, 177–182.

Gustafsson, A., B. K. Lind, and A. Brahme (1994). A generalized pencil beam algorithm for optimization of radiation therapy. *Med. Phys.* **21**(3), 343–356.

Hubbell, J. H. (2006). Review and history of photon cross section calculations. *Phys. Med. Biol.* **51**, R245–R262.

Huq, M. S. and P. Andreo (2004). Advances in the determination of absorbed dose to water in clinical high-energy photon and electron beams using ionization chambers. *Phys. Med. Biol.* **49**, R49–R104.

Huq, M. S., Y. Yu, Z.-P. Chen, and N. Suntharalingam (1995). Dosimetric characteristics of a commercial multileaf collimator. *Med. Phys.* **22**(2), 241–247.

Källman, P., B. Lind, Eklöf, and A. Brahme (1988). Shaping of arbitrary dose distributions by dynamic multileaf collimation. *Phys. Med. Biol.* **33**(11), 1291–1300.

Kawrakow, I. (2000a). Accurate condensed history Monte Carlo simulation of electron transport. I. EGSnrc, the new EGS4 version. *Med. Phys.* **27**(3), 485–498.

Kawrakow, I. (2000b). Accurate condensed history Monte Carlo simulation of electron transport. II. Application to ion chamber response simulations. *Med. Phys.* **27**(3), 499–513.

Kawrakow, I. (2005). egspp: the EGSnrc C++ class library. PIRS-899, National Research Council of Canada, Ottawa, Canada.

Kawrakow, I. and M. Fippel (2000). Investigation of variance reduction techniques for Monte Carlo photon dose calculation using XVMC. *Phys. Med. Biol.* **45**, 2163–2183.

Kawrakow, I. and D. W. O. Rogers (2006). The EGSnrc code system: Monte Carlo simulation of electron and photon transport. PIRS-701, National Research Council of Canada, Ottawa, Canada.

Khan, F. M. (1994). *The Physics of Radiation Therapy* (Second ed.). Baltimore, MD: Williams & Wilkins.

Kim, J. O., J. V. Siebers, P. J. Keall, M. R. Arnfield, and R. Mohan (2001). A Monte Carlo study of radiation transport through multileaf collimators. *Med. Phys.* **28**(12), 2497–2506.

Klein, O. and Y. Nishina (1929). Scattering of radiation by free electrons on the new relativistic quantum dynamics of Dirac. [in German]. *Z. Phys.* **52**, 853–868.

Kutcher, G. J., L. Coia, M. Gillin, W. F. Hanson, S. Leibel, R. J. Morton, J. R. Palta, J. A. Purdy, L. E. Reinstein, G. K. Svensson, M. Weller, and L. Wingfield (1994). Comprehensive QA for radiation oncology. Report 46 of TG-40 Radiation Therapy Committee, American Association of Physicists in Medicine.

Létourneau, D., M. Gulam, D. Yan, M. Oldham, and J. W. Wong (2004). Evaluation of a 2D diode array for IMRT quality assurance. *Radiather. Oncol.* **70**, 199–206.

Leybovich, L. B., A. Sethi, and N. Dogan (2003). Comparison of ionization chambers of various volumes for IMRT absolute dose verification. *Med. Phys.* **30**(2), 119–123.

LoSasso, T., C.-S. Chui, and C. C. Ling (1998). Physical and dosimetric aspects of a multileaf collimation system used in the dynamic mode for implementing intensity modulated radiotherapy. *Med. Phys.* **25**(10), 1919–1927.

LoSasso, T., C.-S. Chui, and C. C. Ling (2001). Comprehensive quality assurance for the delivery of intensity modulated radiotherapy with a multileaf collimator used in the dynamic mode. *Med. Phys.* **28**(11), 2209–2219.

Low, D. A. (2002). Quality assurance of intensity-modulated radiotherapy. *Semin. Radiat. Oncol.* **12**(3), 219–228.

Low, D. A., R. L. Gerber, S. Mutic, and J. A. Purdy (1998). Phantom for IMRT distribution measurement and treatment verification. *Int. J. Rad. Oncol. Biol. Phys.* **40**(5), 1231–1235.

Ma, C.-M., S. B. Jiang, T. Pawlicki, Y. Chen, J. S. Li, J. Deng, and A. L. Boyer (2003). A quality assurance phantom for IMRT dose verification. *Phys. Med. Biol.* **48**, 561–572.

Mackie, T. R. (2006). History of tomotherapy. *Phys. Med. Biol.* **51**, R427–R453.

Martens, C., C. De Wagter, and W. De Neve (2000). The value of the PinPoint ion chamber for characterization of small field segments used in intensity-modulated radiotherapy. *Phys. Med. Biol.* **45**, 2519–2530.

McNiven, A., T. Kron, and J. Van Dyk (2004). A multileaf collimator phantom for the quality assurance of radiation therapy planning systems and CT simulators. *Int. J. Rad. Oncol. Biol. Phys.* **60**(3), 994–1001.

Miller, C. W. (1953). Travelling-wave linear accelerator for X-ray therapy. *Nature* **171**, 297–298.

Mittelbach, F., M. Goossens, J. Braams, D. Carlisle, and C. Rowley (2004). *The LaTeX Companion* (Second ed.). Addison-Wesley.

Møller, C. (1931). The collision of two particles under the consideration of retarded potentials [in German]. *Z. Phys.* **70**, 786–795.

Nath, R., P. J. Biggs, F. J. Bova, C. C. Ling, J. A. Purdy, J. van de Geijn, and M. S. Weinhous (1993). AAPM code of practice for radiotherapy accelerators. Report 47 of TG-45 Radiation Therapy Committee, American Association of Physicists in Medicine.

Paliwal, B., W. Tome, S. Richardson, and T. R. Mackie (2000). A spiral phantom for IMRT and tomotherapy treatment delivery verification. *Med. Phys.* **27**(11), 2503–2507.

Palm, Å. and O. Mattsson (1999). Experimental study on the influence of the central electrode in Farmer-type ionization chambers. *Phys. Med. Biol.* **44**, 1299–1308.

Pasquino, M., V. Casanova Borca, P. Catuzzo, F. Ozzello, and S. Tofani (2006). Transmission, penumbra and leaf positional accuracy in commissioning and quality assurance program of a multileaf collimator for step-and-shoot IMRT treatments. *Tumori* **92**, 511–516.

Pawlicki, T. and C.-M. Ma (2001). Monte Carlo simulation for MLC-based intensity-modulated radiotherapy. *Med. Dosim.* **26**(2), 157–168.

Podgoršak, E. B. (Ed.) (2005a). *Radiation Oncology Physics: A Handbook for Teachers and Students.* Vienna, Austria: International Atomic Energy Agency.

Podgoršak, E. B. (2005b). *Radiation Physics for Medical Physicists.* Berlin, Germany: Springer-Verlag.

Poppe, B., A. Djouguela, K. Bleshschmidt, A. Willborn, A. Rühmann, and D. Harder (2007). Spatial resolution of 2D ionization chamber arrays for IMRT dose verification: single-detector size and sampling step width. *Phys. Med. Biol.* **52**, 2921–2935.

Rayleigh (1899). On the Transmission of Light through an Atmosphere containing Small Particles in Suspension, and on the Origin of the Blue of the Sky. *Philosophical Magazine* **47**, 375–384.

Richardson, S. L., W. A. Tome, N. P. Orton, and B. R. McNutt, T. R. Paliwal (2003). IMRT delivery verification using a spiral phantom. *Med. Phys.* **30**(9), 2553–2558.

Roesch, W. C. (1958). Dose for nonelectronic equilibrium conditions. *Radiat. Res.* **9**(4), 399–410.

Rogers, D. W. O., I. Kawrakow, J. P. Seuntjens, B. R. B. Walters, and E. Mainegra-Hing (2004). NRC user codes for EGSnrc. PIRS-702, National Research Council of Canada, Ottawa, Canada.

Sánchez-Doblado, F., P. Andreo, R. Capote, A. Leal, M. Perucha, R. Arráns, L. Núñez, E. Mainegra, J. I. Lagares, and E. Carrasco (2003). Ionization chamber dosimetry of small photon fields: a Monte Carlo study on stopping-power ratios for radiosurgery and IMRT beams. *Phys. Med. Biol.* **48**, 2081–2099.

Sánchez-Doblado, F., R. Capote, A. Leal, J. V. Roselló, J. I. Lagares, R. Arráns, and G. H. Hartmann (2005a). Micro ionization chamber dosimetry in IMRT verification: clinical implications of dosimetric errors in the PTV. *Radiother. Oncol.* **75**, 342–348.

Sánchez-Doblado, F., R. Capote, A. Leal, J. V. Roselló, J. I. Lagares, R. Arráns, and G. H. Hartmann (2005b). Microionization chamber for reference dosimetry in IMRT verification: clinical implications on OAR dosimetric errors. *Phys. Med. Biol.* **50**, 959–970.

Sánchez-Doblado, F., G. H. Hartmann, J. Pena, R. Capote, M. Paiusco, B. Rhein, A. Leal, and J. I. Lagares (2007). Uncertainty estimation in intensity-modulated radiotherapy absolute dosimetry verification. *Int. J. Radiation Oncology Biol. Phys.* **68**, 301–310.

Schultz, R. J., P. R. Almond, J. R. Cunningham, J. G. Holt, R. Loevinger, N. Suntharalingam, K. A. Wright, R. Nath, and G. D. Lempert (1983). A protocol for the determination of absorbed dose from high-energy photon and electron beams. *Med. Phys.* **10**(6), 741–771.

Siebers, J. V., P. J. Keall, J. O. Kim, and R. Mohan (2002). A method for photon beam Monte Carlo multileaf collimator particle transport. *Phys. Med. Biol.* **47**, 3225–3249.

Siebers, J. V. and R. Mohan (2003). Monte Carlo and IMRT. In J. R. Palta and T. R. Mackie (Eds.), *Intensity-Modulated Radiation Therapy: The State of the Art*, pp. 531–560. Madison, WI: Medical Physics Publishing.

Smith, A. R. (2006). Proton Therapy. *Phys. Med. Biol.* **51**, R491–R504.

Spencer, L. V. and F. H. Attix (1955). A theory of cavity ionization. *Radiat. Res.* **3**(3), 239–254.

Spezi, E., A. L. Angelini, F. Romani, and A. Ferri (2005). Characterization of a 2D ion chamber array for the verification of radiotherapy treatments. *Phys. Med. Biol.* **50**, 3361–3373.

Spirou, S. V. and C. S. Chui (1994). Generation of arbitrary intensity profiles by dynamic jaws or multileaf collimators. *Med. Phys.* **21**(7), 1031–1041.

Stasi, M., B. Baiotto, G. Barboni, and G. Scielzo (2004). The behavior of several microionization chambers in small intensity modulated radiotherapy fileds. *Med. Phys.* **31**(10), 2792–2795.

Steciw, S., B. Warkentin, S. Rathee, and B. G. Fallone (2005). Three-dimensional IMRT verification with a flat-panel EPID. *Med. Phys.* **32**(2), 600–612.

Svensson, R., P. Källman, and A. Brahme (1994). An analytical solution for the dynamic control of multileaf collimators. *Phys. Med. Biol.* **39**, 37–61.

Thwaites, D. I. and J. B. Tuohy (2006). Back to the future: the history and development of the clinical linear accelerator. *Phys. Med. Biol.* **51**, R343–R362.

Ting, J. Y. and L. W. Davis (2001). Dose verification for patients undergoing IMRT. *Med. Dosim.* **26**(2), 205–213.

Tyagi, N., J. M. Moran, D. W. Litzenberg, A. F. Bielajew, B. A. Frass, and I. J. Chetty (2007). Experimental verification of a Monte Carlo-based MLC simulation model for IMRT dose calculation. *Med. Phys.* **34**(2), 651–663.

van Santvoort, J. P. C. and B. J. M. Heijimen (1996). Dynamic multileaf collimation without 'tongue-and-groove' underdosage effects. *Phys. Med. Biol.* **41**, 2091–2105.

Verhaegen, F. and J. Seuntjens (2003). Monte Carlo modelling of external radiotherapy photon beams. *Phys. Med. Biol.* **48**, R107–R164.

Wang, X., S. Spirou, T. LaSasso, J. Stein, C.-S. Chui, and R. Mohan (1996). Dosimetric verification of intensity-modulated fields. *Med. Phys.* **23**(3), 317–327.

Warkentin, B., S. Steciw, S. Rathee, and B. G. Fallone (2003). Dosimetric IMRT verification with a flat-panel EPID. *Med. Phys.* **30**(12), 3143–3155.

Webb, S. (1993). *The Physics of Three-Dimensional Radiation Therapy.* Bristol, UK: IOP Publishing Ltd.

Webb, S. (2000). A new concept of multileaf collimator (the shuttling MLC)–an interpreter for high-efficiency IMRT. *Phys. Med. Biol.* **45**, 3343–3358.

Webb, S. (2003). The physical basis of IMRT and inverse planning. *Br. J. Radiol.* **76**, 678–689.

Webb, S., T. Bortfeld, J. Stein, and D. Convery (1997). The effect of stair-step leaf transmission on the 'tongue-and-groove problem' in dynamic radiotherapy with a multileaf collimator. *Phys. Med. Biol.* **42**, 595–602.

Wiezorek, T., N. Banz, M. Schwedas, H. Schelthauer, M. Salz, D. Georg, and T. G. Wendt (2005). Dosimetric quality assurance for intensity-modulated radiotherapy. *Strahlenter. Onkol.* **181**(7), 468–474.

Williams, P. C. (2003). IMRT: delivery techniques and quality assurance. *Br. J. Radiol.* **76**, 766–776.

Winkler, P., A. Hefner, and D. Georg (2005). Dose-response characteristics of an amorphous silicon EPID. *Med. Phys.* **32**(10), 3095–3105.

Woo, M. K. and A. Nico (2005). Impact of multileaf collimator leaf positioning accuracy on intensity modulation radiation therapy quality assurance ion chamber measurements. *Med. Phys.* **32**(5), 1440–1445.

Xia, P. and C. Chuang (2003). Patient-specific quality assurance in IMRT. In J. R. Palta and T. R. Mackie (Eds.), *Intensity-Modulated Radiation Therapy: The State of the Art*, pp. 495–514. Madison, WI: Medical Physics Publishing.

Xia, P. and J. Y. Ting (2007). Point/Counterpoint: segmental MLC is superior to dynamic MLC for IMRT delivery. *Med. Phys.* **34**(7), 2673–2675.

Xia, P. and L. J. Verhey (1998). Multileaf collimator leaf sequencing algorithm for intensity modulated beams with multiple static segments. *Med. Phys.* **25**(8), 1424–1434.

Index